Real-time Trajectory Design for Unmanned Aerial Vehicles using Receding Horizon Control

by

Yoshiaki Kuwata

Bachelor of Engineering
The University of Tokyo, 2001

Submitted to the Department of Aeronautics and Astronautics
in partial fulfillment of the requirements for the degree of

Master of Science in Aeronautics and Astronautics

at the

MASSACHUSETTS INSTITUTE OF TECHNOLOGY

June 2003

Author .....
Department of Aeronautics and Astronautics
May 23, 2003

Certified by .....
Jonathan P. How
Associate Professor
Thesis Supervisor

Accepted by .....
Edward M. Greitzer
H.N. Slater Professor of Aeronautics and Astronautics
Chair, Committee on Graduate Students

Real-time Trajectory Design for Unmanned Aerial Vehicles using Receding Horizon Control

by

Yoshiaki Kuwata

Submitted to the Department of Aeronautics and Astronautics
on May 23, 2003, in partial fulfillment of the
requirements for the degree of
Master of Science in Aeronautics and Astronautics

Abstract

This thesis investigates the coordination and control of fleets of *unmanned aerial vehicles* (UAVs). Future UAVs will operate autonomously, and their control systems must compensate for significant dynamic uncertainty. A hierarchical approach has been proposed to account for various types of uncertainty at different levels of the control system. The resulting controller includes task assignment, graph-based coarse path planning, detailed trajectory optimization using *receding horizon control* (RHC), and a low-level waypoint follower. *Mixed-integer linear programming* (MILP) is applied to both the task allocation and trajectory design problems to encode logical constraints and discrete decisions together with the continuous vehicle dynamics.

The MILP RHC uses a simple vehicle dynamics model in the near term and an approximate path model in the long term. This combination gives a good estimate of the cost-to-go and greatly reduces the computational effort required to design the complete trajectory, but discrepancies in the assumptions made in the two models can lead to infeasible solutions. The primary contribution of this thesis is to extend the previous stable RHC formulation to ensure that the on-line optimizations will always be feasible. Novel pruning and graph-search algorithms are also integrated with the MILP RHC, and the resulting controller is analytically shown to guarantee finite-time arrival at the goal. This pruning algorithm also significantly reduces the computational load of the MILP RHC.

The control algorithms acting on four different levels of the hierarchy were integrated and tested on two hardware testbeds (three small ground vehicles and a hardware-in-the-loop simulation of three aircraft autopilots) to verify real-time operation in the presence of real-world disturbances and uncertainties. Experimental results show the successful control loop closures in various scenarios, including operation with restricted environment knowledge based on a realistic sensor and a coordinated mission by different types of UAVs.

Thesis Supervisor: Jonathan P. How
Title: Associate Professor

Acknowledgments

I would like to thank several people who made this research possible. First, my advisor Professor Jonathan How guided me through this work with a lot of insight. This research is an extension of John Bellingham's work. Many inputs from Arthur Richards are appreciated. The hardware experiments could not be performed without the help of Chung Tin, Ian Garcia, and Ellis King. I would also like to thank Louis Breger, Mehdi Alighanbari, Luca Bertuccelli, and Megan Mitchell for their support through the ordeal. Last but not least, administrative assistant Margaret Yoon helped notably to put the final touches on this thesis.

This research was funded under DARPA contract # N6601-01-C-8075. The testbeds described in Chapter 5 of the thesis were funded under the DURIP grant (AFOSR Grant # F49620-02-1-0216).

Contents

List of Figures

List of Tables

Chapter 1

Introduction

1.1 Background

The capabilities and roles of *unmanned aerial vehicles* (UAVs) are evolving, and new concepts are required for their control [1]. For example, today's UAVs typically require several operators per aircraft, but future UAVs will be designed to make tactical decisions autonomously and will be integrated into coordinated teams to achieve high-level goals, thereby allowing one operator to control a group of vehicles. Thus, new methods in planning and execution are required to coordinate the operation of a fleet of UAVs. An overall control system architecture must also be developed that can perform optimal coordination of the vehicles, evaluate the overall system performance in real time, and quickly reconfigure to account for changes in the environment or the fleet. This thesis presents results on the guidance and control of fleets of cooperating UAVs, including goal assignment, trajectory optimization, and hardware experiments.

For many vehicles, obstacles, and targets, fleet coordination is a very complicated optimization problem [1, 2, 3] where computation time increases very rapidly with the problem size. Ref. [4] proposed an approach to decompose this large problem into assignment and trajectory problems, while capturing key features of the coupling between them. This allows the control architecture to solve an allocation problem first to determine a sequence of waypoints

for each vehicle to visit, and then concentrate on designing paths to visit these pre-assigned waypoints. Since the assignment is based on a reasonable estimate of the trajectories, this separation causes a minimal degradation in the overall performance.

1.1.1 Trajectory Design

Optimizing a kinematically and dynamically constrained path is a significant problem in controlling autonomous vehicles, and has received attention in the fields of robotics, undersea vehicles, and aerial vehicles [5, 6]. Planning trajectories that are both optimal and dynamically feasible is complicated by the fact that the space of possible control actions is extremely large and non-convex, and that simplifications reducing the dimensionality of the problem without losing feasibility and optimality are very difficult to achieve.

Previous work demonstrated the use of *mixed-integer linear programming* (MILP) in off-line trajectory design for vehicles under various dynamic and kinematic constraints [7, 8, 9]. MILP allows the inclusion of non-convex constraints and discrete decisions in the trajectory optimization. Binary decision variables allow the choice of whether to pass "left" or "right" of an obstacle, for example, or the discrete assignment of vehicles to targets to be included in the planning problem. Optimal solutions can be obtained for these trajectory generation problems using commercially available software such as CPLEX [10, 11]. Using MILP, however, to design a whole trajectory with a planning horizon fixed at the goal is very difficult to perform in real time because the computational effort required grows rapidly with the length of the route and the number of obstacles to be avoided.

This limitation can be avoided by using a receding *planning horizon* in which MILP is used to form a shorter plan that extends towards the goal, but does not necessarily reach it. This overall approach is known as either *model predictive control* (MPC) or *receding horizon control* (RHC) [12]. The performance of a RHC strongly depends on the proper evaluation of the terminal penalty on the shorter plan. This evaluation is difficult when the feasibility of the path beyond the plan must be ensured. Previous work presented a heuristic to approximate the trajectory beyond the shorter plan that used straight line paths

to estimate the cost-to-go from the plan's end point to the goal [3, 13, 14]. This RHC makes full use of the future states predicted through a model in order to obtain the current control inputs. In a trajectory design problem, the future states can be predicted by the straight line paths. This is because the shortest path from any location to the goal is a connection of straight lines, if no vehicle dynamics are involved and no disturbances act on the vehicle. As such, generating a coarse cost map based on straight line approximations (and then using Dijkstra's algorithm) provides a good prediction of the future route beyond the planning horizon. The receding horizon controller designs a detailed trajectory over the planning horizon by evaluating the terminal state with this cost map.

While this planner provides good results in practice, the trajectory design problem can become infeasible when the positioning of nearby obstacles leaves no dynamically feasible trajectory from the state that is to be reached by the vehicle. This is because the Dijkstra's algorithm neglects the vehicle dynamics when constructing the cost map. In such a case, the vehicle cannot follow the heading discontinuities where the line segments intersect since the path associated with the cost-to-go estimate is not dynamically feasible.

This thesis presents one way to overcome the issues with the previous RHC approach by evaluating the cost-to-go estimate along straight line paths that are known to be "near" *kinodynamically feasible* paths to the goal (see Chapter 3 for details). This new trajectory designer is shown to: (a) be capable of designing trajectories in highly constrained environments, where the formulation presented in Ref. [13] is incapable of reaching the goal; and (b) travel more aggressively since the turn around an obstacle corner is designed at the MILP optimization phase, unlike a trajectory designer that allows only predetermined turns at each corner [15].

Although RHC has been successfully applied to chemical process control [16], applications to systems with faster dynamics, such as those found in the field of aerospace, have been impractical until recently. The on-going improvements in computation speed has stimulated recent hardware work in this field, including the on-line use of *nonlinear trajectory generator* (NTG) optimization for control of an aerodynamic system [17, 18]. The use of MILP together

with RHC enables the application of the real-time trajectory optimization to scenarios with multiple ground and aerial vehicles that operate in dynamic environments with obstacles.

1.1.2 Task Allocation

A further key aspect of the UAV problem is the allocation of different tasks to UAVs with different capabilities [19]. This is essentially a *multiple-choice multi-dimension knapsack problem* (MMKP) [20], where the number of possible allocations grows rapidly as the problem size increases. The situation is further complicated if the tasks:

- Are strongly coupled – *e.g.*, a waypoint must be visited three times, first by a type 1 UAV, followed by a type 2, and then a type 3. These three events must occur within t_l seconds of each other.
- Have tight relative timing constraints – *e.g.*, three UAVs must be assigned to strike a target from three different directions within 2 seconds of each other.

With limited resources within the team, the coupling and timing constraints can result in very tight linkages between the activities of the various vehicles. Especially towards the end of missions, these tend to cause significant problems (*e.g.*, "churning" and/or infeasible solutions) for the approximate assignment algorithms based on "myopic algorithms" (*e.g.* iterative "greedy" or network flow solutions) that have recently been developed [2, 19]. MILP, again, provides a natural language for codifying these various mission objectives and constraints using a combination of binary (*e.g.*, as switches for the discrete/logical decisions) and continuous (*e.g.*, for start and arrival time) variables [3, 12, 4]. MILP allows us to account for the coupling and relative timing constraints and to handle large fleets with many targets and/or pop-up threats.

1.2 Thesis Overview

This thesis discusses a hierarchical approach to the coordination and control of a fleet of UAVs, as shown in Figure 1-1. The box with dashed lines is called the *planner* and produces

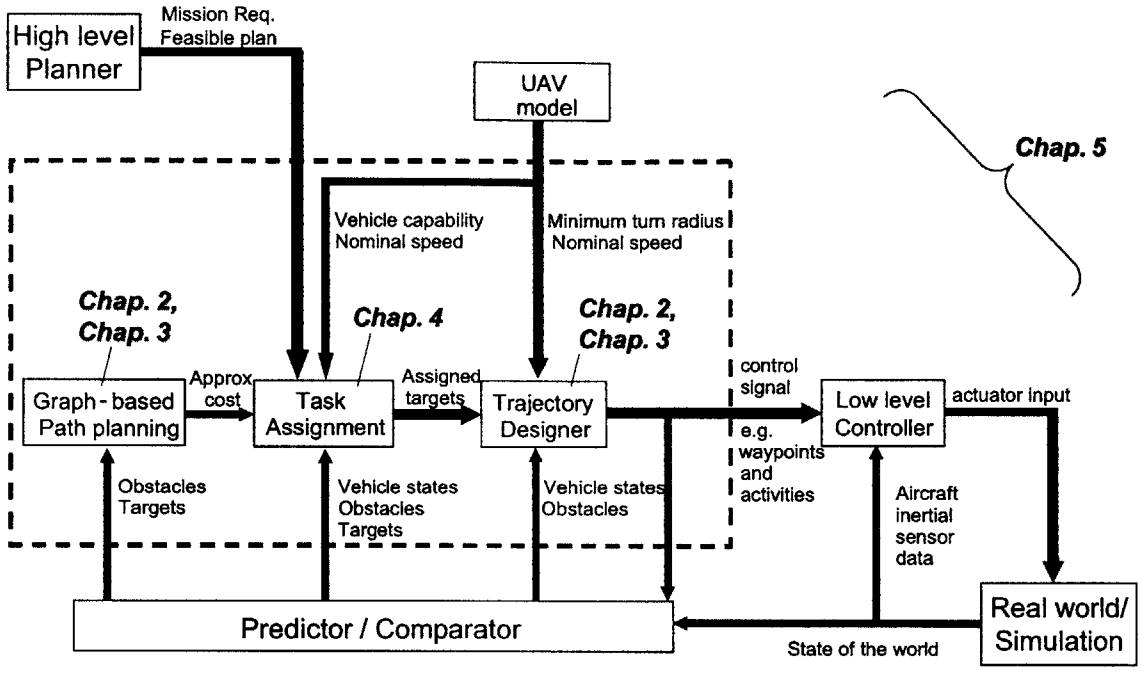

Figure 1-1: Block diagram of the hierarchical approach developed in this thesis.

a control signal to vehicles. The three boxes in the planner (graph-based path planning, task assignment, trajectory designer) are the key technologies in this approach, and are discussed in Chapters 2 through 4. Chapter 2 formulates a MILP trajectory generation algorithm for minimum time of arrival problems. In this chapter, a receding horizon controller using MILP [13, 14] has been extended to include multiple waypoints for multiple vehicles with the entire algorithm comprehensively expressed in mixed-integer linear form. Chapter 3 presents a modification of the trajectory planner to guarantee that the vehicle always reaches the goal in bounded time, even when operating in an environment with obstacles.

Chapter 4 demonstrates, in a complex example with 6 UAVs and 12 waypoints, that adding timing constraints to the allocation problem can have a significant impact on the computational time. An approximate decomposition algorithm [3, 4] is extended to include these relative timing constraints and adds extra degrees of freedom to the formulation, allowing the UAVs to loiter during the mission. The overall block diagram in Figure 1-1 is implemented in software and hardware in Chapter 5. The control loops around the planner

are closed one at a time, and several experimental results demonstrate the real-time loop closures using two new testbeds.

Chapter 2

Receding Horizon Control using Mixed-Integer Linear Programming

This chapter presents several extensions to a previous formulation of a receding horizon controller for minimum time trajectory generation problems [14]. Section 2.1 addresses the concept of *receding horizon control* (RHC) and how it is applied to trajectory optimization problems. Then, the trajectory optimization problem is formulated using *mixed-integer linear programming* (MILP), which is well suited to trajectory planning because it can directly incorporate logical constraints such as obstacle avoidance and waypoint selection and because it provides an optimization framework that can account for basic dynamic constraints such as turn limitations.

2.1 Overview of the Receding Horizon Controller

Improvements in UAV capabilities make it possible for UAVs to perform longer and more complicated missions and scenarios. In these missions and scenarios, optimal path navigation through complicated environments is crucial to mission success. As more vehicles and more targets are involved in the mission, the complexity of the trajectory design problem grows rapidly, increasing the computation time to obtain the optimal solution [9]. One alternative

to overcome this computational burden is to use receding horizon control (RHC) [21]. The RHC uses a plant model and an optimization technique to design an input trajectory that optimizes the plant's output over a period of time called *the planning horizon.* A portion of the input trajectory is then implemented over the shorter *execution horizon*, and the optimization is performed again starting from the state that is to be reached. If the control problem is not completed at the end of the planning horizon, the cost incurred past the planning horizon must be accounted for in the cost function. The selection of the terminal penalty in RHC design is a crucial factor in obtaining reasonable performance, especially in the presence of obstacles and no-fly zones.

In general, the cost function of a receding horizon controller's optimization problem estimates the cost-to-go from a selected terminal state to the goal. For vehicle trajectory planning problems in a field with no-fly zones, Ref. [13] presented a receding horizon controller that uses the length of a *path to the goal* made up of straight line segments as its cost-to-go. This is a good approximation for minimum time of arrival problems since the true minimum distance path to the goal will typically touch the corners of obstacles that block the vehicle's path. In order to connect the detailed trajectory designed over the planning horizon and the coarse cost map beyond it, the RHC selects an obstacle corner that is visible from the terminal point and is associated with the best path. This approach has another advantage in terms of real-time applications. The cost map not only gives a good prediction of vehicle behavior beyond the planning horizon, but because it is very coarse, it also can be rapidly updated when the environment and/or situational awareness changes.

The following sections focus on solving the vehicle trajectory design problem after a set of ordered goals are assigned to each vehicle. The MILP formulation presented here extends an existing algorithm [13, 14] to incorporate more sophisticated scenarios (*e.g.,* multiple vehicles, multiple goals) and detailed dynamics (*e.g.,* constant speed operation).

2.2 Model of Aircraft Dynamics

It has been shown that the point mass dynamics subject to two-norm constraints form an approximate model for limited turn-rate vehicles, provided that the optimization favors the minimum time, or minimum distance, path [9]. By explicitly including minimum speed constraints, this formulation can be applied to problems with various objectives, such as expected score and risk, with a minimal increase in computation time.

2.2.1 Discrete Time System

Aircraft dynamics is expressed as a simple point mass with position and velocity $[x, y, v_x, v_y]^T$ as state variables and acceleration $[a_x, a_y]^T$ as control inputs.

$$\frac{\mathrm{d}}{\mathrm{d}t}\begin{bmatrix} x \\ y \\ v_x \\ v_y \end{bmatrix} = \begin{bmatrix} 0 & 0 & 1 & 0 \\ 0 & 0 & 0 & 1 \\ 0 & 0 & 0 & 0 \\ 0 & 0 & 0 & 0 \end{bmatrix}\begin{bmatrix} x \\ y \\ v_x \\ v_y \end{bmatrix} + \begin{bmatrix} 0 & 0 \\ 0 & 0 \\ 1 & 0 \\ 0 & 1 \end{bmatrix}\begin{bmatrix} a_x \\ a_y \end{bmatrix} \tag{2.1}$$

The zero-order hold equivalent discrete time system is

$$\begin{bmatrix} x \\ y \\ v_x \\ v_y \end{bmatrix}_{k+1} = \begin{bmatrix} 1 & 0 & \Delta t & 0 \\ 0 & 1 & 0 & \Delta t \\ 0 & 0 & 1 & 0 \\ 0 & 0 & 0 & 1 \end{bmatrix}\begin{bmatrix} x \\ y \\ v_x \\ v_y \end{bmatrix}_k + \begin{bmatrix} (\Delta t)^2/2 & 0 \\ 0 & (\Delta t)^2/2 \\ \Delta t & 0 \\ 0 & \Delta t \end{bmatrix}\begin{bmatrix} a_x \\ a_y \end{bmatrix}_k \tag{2.2}$$

where k expresses a time step and Δt is the time interval. Note that the control input $[a_x, a_y]_k^T$ stays constant over each time interval Δt under the zero-order hold assumption.

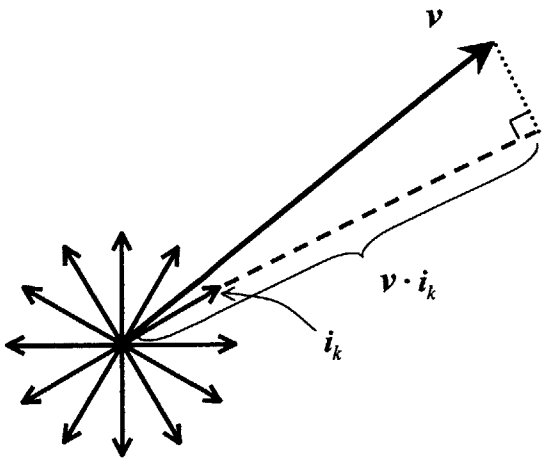

Figure 2-1: Projection of velocity vector

2.2.2 Speed Constraints

The constraint on the maximum speed $v_{\max}$ is written as a combination of linear constraints on the velocity vector $\boldsymbol{v}$ using uniformly distributed unit vectors

$$\boldsymbol{v} \cdot \boldsymbol{i}_k \leq v_{\max}, \qquad k = 1, \ldots, n_{v_{\max}} \tag{2.3}$$

$$\boldsymbol{i}_k = \begin{bmatrix} \cos\left(\dfrac{2\pi k}{n_{v_{\max}}}\right) \\ \sin\left(\dfrac{2\pi k}{n_{v_{\max}}}\right) \end{bmatrix} \tag{2.4}$$

where $n_{v_{\max}}$ is the number of unit vectors $\boldsymbol{i}_k$ onto which the velocity vector is projected. The speed constraint is effectively a constraint on the length of the projection of the velocity vector onto a unit vector, as shown in Figure 2-1. Eqs. 2.3 and 2.4 require that the velocity vector be inside a regular polygon with $n_{v_{\max}}$ sides circumscribed about a circle of radius $v_{\max}$.

A constraint on the minimum speed $v_{\min}$ can be expressed in the similar way: the dot product of the velocity vector and a unit vector must be larger than $v_{\min}$. However, it is different from the maximum speed constraint in that *at least one* of the constraints must be

active, instead of all of them,

$$\boldsymbol{v} \cdot \boldsymbol{i}_k \geq v_{\min}, \qquad \exists k, \qquad (k = 1, \ldots, n_{v_{\min}}) \tag{2.5}$$

$$\boldsymbol{i}_k = \begin{bmatrix} \cos\left(\dfrac{2\pi k}{n_{v_{\min}}}\right) \\ \sin\left(\dfrac{2\pi k}{n_{v_{\min}}}\right) \end{bmatrix} \tag{2.6}$$

Here, $n_{v_{\min}}$ is the number of unit vectors onto which the velocity vector is projected. Eq. 2.5 is a non-convex constraint and is written as a combination of mixed-integer linear constraints

$$\boldsymbol{v} \cdot \boldsymbol{i}_k \geq v_{\min} - M_v(1 - b_{\text{speed},k}), \qquad k = 1, \ldots, n_{v_{\min}} \tag{2.7}$$

$$\sum_{k=1}^{n_{v_{\min}}} b_{\text{speed},k} \geq 1 \tag{2.8}$$

where M_v is a number larger than $2v_{\min}$, and the $b_{\text{speed},k}$ are binary variables that express the non-convex constraints in the MILP form. Note that if $b_{\text{speed},k} = 1$, the inequality in Eq. 2.7 is active, indicating that the minimum speed constraint is satisfied. On the other hand, if $b_{\text{speed},k} = 0$, the k^{th} constraint in Eq. 2.7 is not active, and the constraint on minimum speed is relaxed. Eq. 2.8 requires that at least one constraint in Eq. 2.7 be active. Eqs. 2.6 to 2.8 ensure that the tip of the velocity vector lies outside of a regular polygon with $n_{v_{\min}}$ sides circumscribed on the outside of a circle with radius $v_{\min}$.

Figure 2-2 shows two polygons that constrain the length of the velocity vector. The dashed line represents a polygon associated with minimum speed constraints and the solid line is for the maximum speed. The maximum and minimum speed constraints force the tip of the velocity vector to stay in the region between these two polygons. The values used in this example are:

$$v_{\max} = 1, \qquad v_{\min} = 0.95, \qquad n_{v_{\max}} = 20, \qquad n_{v_{\min}} = 10, \tag{2.9}$$

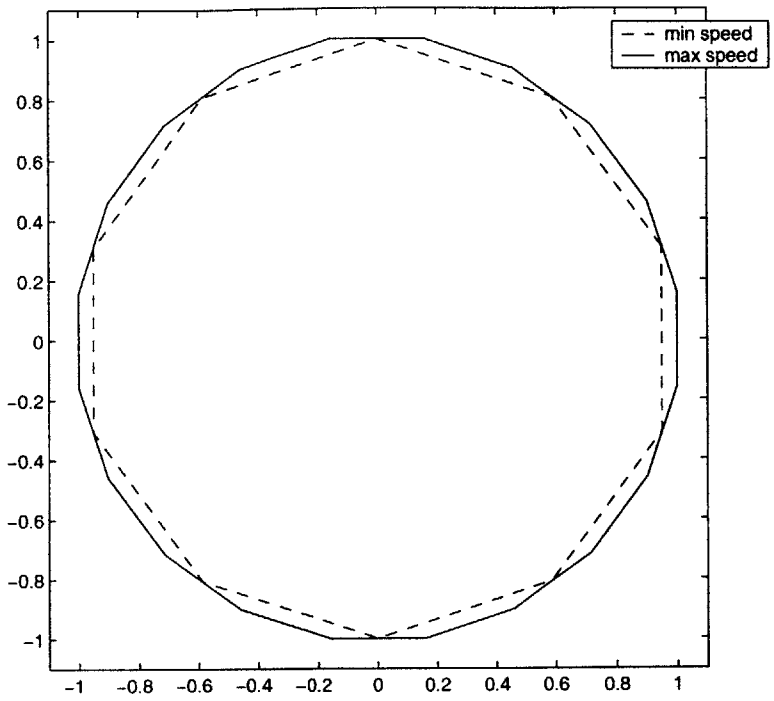

Figure 2-2: Convex and non-convex constraints on a normalized velocity vector

Since the minimum speed constraints require binary variables, which typically slows down the MILP optimization process, $n_{v_{\min}}$ is typically much smaller than $n_{v_{\max}}$. Note that the speed constraints can become infeasible if $v_{\max}$ and $v_{\min}$ are set equal unless $n_{v_{\max}} = n_{v_{\min}}$. In Figure 2-2, for example, if the radius of the dashed polygon is increased, then no feasible velocity vector exists in the direction $[0, 1]^T$ (straight up), because the minimum constraint will be larger than the maximum constraint.

2.2.3 Minimum Turning Radius

UAVs usually fly at roughly a constant speed v and have a minimum turning radius $r_{\min}$. The constraint on the turning radius r is

$$r_{\min} \leq r = \frac{v^2}{a} \tag{2.10}$$

and this constraint can be written as a constraint on lateral acceleration,

$$a \leq \frac{v^2}{r_{\min}} \equiv a_{\max} \tag{2.11}$$

where a is the magnitude of the acceleration vector and $a_{\max}$ is the maximum acceleration magnitude. Similar to the maximum speed constraint, the constraint on the maximum acceleration is written as a combination of linear constraints on the acceleration vector $\boldsymbol{a}$

$$\boldsymbol{a} \cdot \boldsymbol{i}_k \leq a_{\max}, \qquad k = 1, \ldots, n_a \tag{2.12}$$

$$\boldsymbol{i}_k = \begin{bmatrix} \cos\left(\frac{2\pi k}{n_a}\right) \\ \sin\left(\frac{2\pi k}{n_a}\right) \end{bmatrix} \tag{2.13}$$

where n_a is the number of unit vectors onto which the acceleration vector is projected. The constraints on velocity in Eqs. 2.3 to 2.8 keep the speed roughly constant, so the allowable acceleration vector direction is perpendicular to the velocity vector. The state equation (Eq. 2.2) for the vehicle uses a zero-order hold on the inputs, so the acceleration vector stays the same over the time-step Δt. Figure 2-3 shows a turn with the maximum lateral acceleration. The actual minimum turning radius $r_{\min_{\text{actual}}}$ is a radius of the polygon in the figure. It is geometrically calculated, using the relation between $a_{\max}$ and $r_{\min}$ in Eq. 2.11, as

$$r_{\min_{\text{actual}}} = r_{\min}\sqrt{1 - \left(\frac{v\,\Delta t}{2r_{\min}}\right)^2} \tag{2.14}$$

and is slightly smaller than $r_{\min}$. Table 2.1 shows the values obtained from this equation.

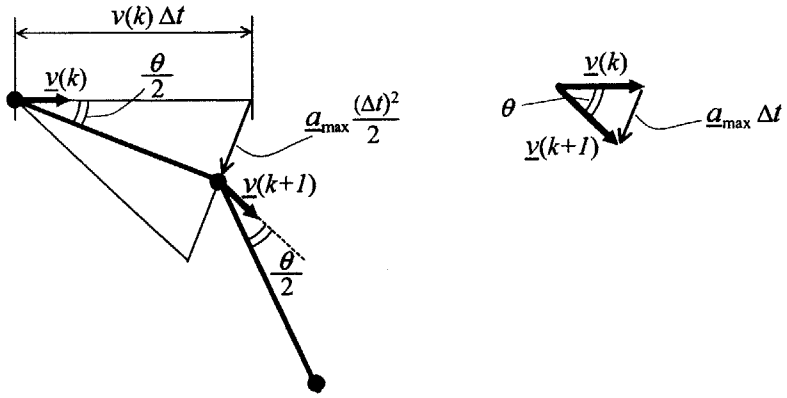

Figure 2-3: Turn with the maximum acceleration. The points marked with • show the discrete trajectory points and are the corners of a regular polygon. The thick lines show a regular polygon inscribed in a circle of minimum turning radius. Note that two triangles in the figure are similar.

Table 2.1: Minimum turn radii realized in a discretized model

$(v\,\Delta t)/r_{\min}$	$r_{\min_{\text{actual}}}/r_{\min}$
0.2	0.99
0.4	0.98
0.6	0.95
0.8	0.92
1.0	0.87

2.3 Collision Avoidance Constraints

2.3.1 Obstacle Avoidance

During the overall mission, UAVs must stay outside of no-fly-zones, which are modelled as obstacles in our formulation [17, 22, 23]. Obstacle avoidance is a non-convex constraint and requires binary variables and a large number M in MILP. At each time step k, the vehicle must stay outside of a rectangular obstacle defined by four parameters $[x_l, y_l, x_u, y_u]$. The four edges of each obstacle are given by

$$x = x_l; \quad x = x_u; \quad y = y_l; \quad \text{or} \quad y = y_u \tag{2.15}$$

The constraints on vehicle position are formulated as

$$x_k \leq x_l + M\, b_{\text{obst},1jk} \tag{2.16}$$

$$y_k \leq y_l + M\, b_{\text{obst},2jk} \tag{2.17}$$

$$x_k \geq x_u - M\, b_{\text{obst},3jk} \tag{2.18}$$

$$y_k \geq y_u - M\, b_{\text{obst},4jk} \tag{2.19}$$

$$\sum_{i=1}^{4} b_{\text{obst},ijk} \leq 3 \tag{2.20}$$

$$j = 1, \ldots, n_o, \qquad k = 1, \ldots, n_p$$

where $[x_k, y_k]^T$ gives the position of a vehicle at time k, M is a number larger than the size of the world map, n_o is the number of obstacles, n_p is the number of steps in the planning horizon, and $b_{\text{obst},ijk}$ is an $i-j-k^{\text{th}}$ element of a binary matrix of size 4 by n_o by n_p. At time-step k, if $b_{\text{obst},ijk} = 0$ in Eqs. 2.16 to 2.19, then the constraint is active and the vehicle is outside of the j^{th} obstacle. If not, the large number M relaxes the obstacle avoidance constraint. The logical constraint in Eq. 2.20 requires that at least one of the four constraints be active for each obstacle at each time-step. The obstacle shape is assumed to be rectangular, but this formulation is extendable to obstacles with polygonal shapes. Also, non-convex obstacles can be easily formed by overlapping several rectangular obstacles.

Figure 2-4 shows that we must expand the obstacle size at the planning level to account for the discrete steps taken by the vehicle. This increase is done at both the estimation and trajectory design phases. Since the avoidance constraints are only applied at discrete time steps shown as $\otimes$ marks, it is possible for the planned trajectory to "cut the corner" of the obstacle between time points. Each waypoint is separated by $v\Delta t$ and an obstacle $[x_l, y_l, x_u, y_u]$ must be expanded in each direction by $v\Delta t/(2\sqrt{2})$, which is the maximum incursion distance, so that

$$[x_l, y_l, x_u, y_u]\Big|_{\text{expanded}} = \left[x_l - \frac{v\Delta t}{2\sqrt{2}},\, y_l - \frac{v\Delta t}{2\sqrt{2}},\, x_u + \frac{v\Delta t}{2\sqrt{2}},\, y_u + \frac{v\Delta t}{2\sqrt{2}}\right] \tag{2.21}$$

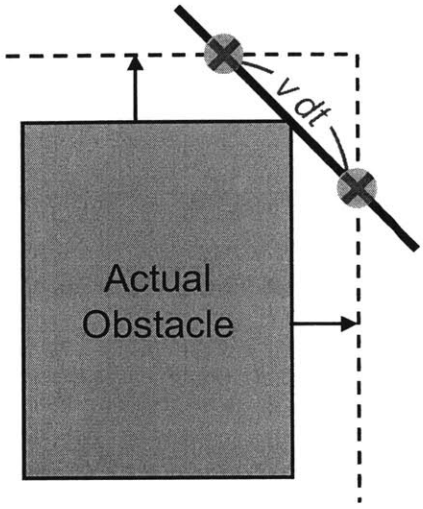

Figure 2-4: Corner cut and obstacle expansion

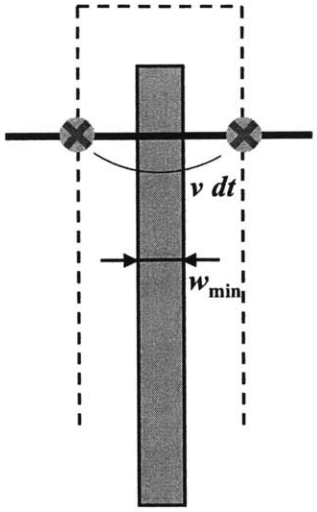

Figure 2-5: Step over of thin obstacle

With the obstacles expanded, Figure 2-5 illustrates the minimum width $w_{\min}$ of the obstacles that is required to ensure that no "step-over" can occur.

$$w_{\min} = v\,\Delta t\left(1 - \frac{1}{\sqrt{2}}\right) \tag{2.22}$$

2.3.2 Vehicle Avoidance

Collision avoidance between vehicles is written in the same way as obstacle avoidance [24, 25, 26]. Assume the i^{th} vehicle has a certain physical size and safety distance surrounding it that forms together a rectangle of $2d_i$ by $2d_i$ around its center. At each time k, the position of the i^{th} vehicle and that of the j^{th} vehicle must satisfy the following relations:

$$x_{ik} \leq x_{jk} + (d_i + d_j) + M\, b_{\text{veh},1ijk} \tag{2.23}$$

$$y_{ik} \leq y_{jk} + (d_i + d_j) + M\, b_{\text{veh},2ijk} \tag{2.24}$$

$$x_{ik} \geq x_{jk} - (d_i + d_j) - M\, b_{\text{veh},3ijk} \tag{2.25}$$

$$y_{ik} \geq y_{jk} - (d_i + d_j) - M\, b_{\text{veh},4ijk} \tag{2.26}$$

$$\sum_{l=1}^{4} b_{\text{veh},lijk} \leq 3 \tag{2.27}$$

$$i = 1, \ldots, n_v, \qquad j = i+1, \ldots, n_v \qquad k = 1, \ldots, n_p$$

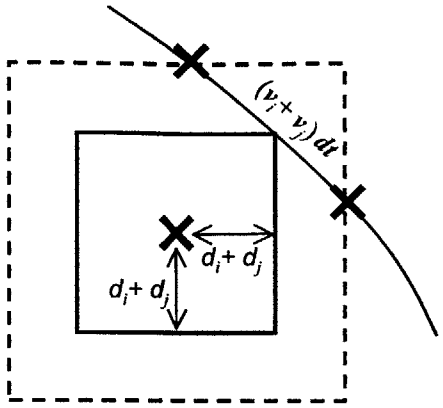

Figure 2-6: Safety distance for vehicle collision avoidance in relative frame

where $[x_{ik}, y_{ik}]^T$ gives the position of a vehicle i at time k, n_v is the number of vehicles, and $b_{\text{veh},lijk}$ is the $l-i-j-k^{\text{th}}$ element of a binary matrix of size 4 by n_v by n_v by n_p. If $b_{\text{veh},lijk} = 0$ in Eqs. 2.23 to 2.26, the constraint is active, and the safety boxes of the two vehicles, i and j, do not intersect each other.

Again, in order to account for the discretized time, a margin is added to the vehicle rectangle of $2d_i$ by $2d_i$. If two vehicles i and j are moving towards each other with a speed of v_i and v_j respectively, the distance between each waypoint in a relative coordinate frame, as shown in Figure 2-6, can be as large as $(v_i + v_j)\,\Delta t$. Thus, the size of the i^{th} vehicle in this MILP optimization model must be expanded to a size of $2d_i|_{\text{expanded}}$ by $2d_i|_{\text{expanded}}$ where

$$d_i|_{\text{expanded}} = d_i + \frac{v_i\,\Delta t}{\sqrt{2}}, \qquad i = 1, \ldots, n_v \tag{2.28}$$

2.4 Plan beyond the Planning Horizon

The Receding Horizon Controller in Ref. [14] uses a coarse cost map based on straight lines to predict the trajectory beyond the planning horizon. There are two aspects involved in connecting the detailed trajectory over the planning horizon to this coarse cost map. First, MILP selects a cost point that leads the vehicle to the goal along the shortest path. Second, it ensures that the selected cost point is visible from a point on the planning horizon (*i.e.*, the straight line segment connecting the selected cost point and the horizon point must be obstacle/collision free).

Given the location of the obstacles and a goal, the cost points are defined as the obstacle corners and the goal itself. The shortest distance from a cost point to the goal along kinematically feasible straight-line segments forms a cost associated with the cost point and goal. If a cost point is inside of another obstacle, it has an infinite cost.

Let $[x_{\mathrm{cp},i}, y_{\mathrm{cp},i}]^T$ denote the i^{th} cost point, c_i the cost associated with the i^{th} cost point, and $c_{\mathrm{vis},k}$ the cost-to-go at the cost point selected by vehicle k. The binary variables associated with cost point selection $\boldsymbol{b}_{\mathrm{cp}}$ will have three dimensions for cost point, goal, and vehicle, where n_c is a number of cost points, and n_g is a number of goals:

$$c_{\mathrm{vis},k} = \sum_{i=1}^{n_c}\sum_{j=1}^{n_g} c_i\, b_{\mathrm{cp},ijk} \tag{2.29}$$

$$\sum_{i=1}^{n_c}\sum_{j=1}^{n_g} b_{\mathrm{cp},ijk} = 1, \qquad k = 1,\ldots,n_v \tag{2.30}$$

Eq. 2.30 enforces the constraint that each vehicle must choose a combination of goal and cost point, and Eq. 2.29 extracts the cost-to-go at the selected point from the cost map c_i.

In order to ensure that the selected cost point $[x_{\mathrm{vis},k}, y_{\mathrm{vis},k}]^T$ is visible from the terminal point $[(x_{n_p})_k, (y_{n_p})_k]^T$ of vehicle k, obstacle avoidance is checked at n_t test points that are placed on a line segment connecting the two points. This requires binary variables $\boldsymbol{b}_{\mathrm{vis}}$ that have four dimensions: the obstacle corner, vehicle, test point, and obstacle. The test conditions can be written as:

$$\begin{bmatrix} x_{\mathrm{vis},k} \\ y_{\mathrm{vis},k} \end{bmatrix} = \sum_{i=1}^{n_c}\sum_{j=1}^{n_g} \begin{bmatrix} x_{\mathrm{cp},k} \\ y_{\mathrm{cp},k} \end{bmatrix} b_{\mathrm{cp},ijk} \tag{2.31}$$

$$\begin{bmatrix} x_{\mathrm{LOS},k} \\ y_{\mathrm{LOS},k} \end{bmatrix} = \begin{bmatrix} x_{\mathrm{vis},k} \\ y_{\mathrm{vis},k} \end{bmatrix} - \begin{bmatrix} (x_{n_p})_k \\ (y_{n_p})_k \end{bmatrix} \tag{2.32}$$

$$\begin{bmatrix} x_{\mathrm{test},km} \\ y_{\mathrm{test},km} \end{bmatrix} = \begin{bmatrix} (x_{n_p})_k \\ (y_{n_p})_k \end{bmatrix} + \frac{m}{n_t} \begin{bmatrix} x_{\mathrm{LOS},k} \\ y_{\mathrm{LOS},k} \end{bmatrix} \tag{2.33}$$

$$x_{\mathrm{test},km} \le (x_l)_n + M\, b_{\mathrm{vis},1kmn} \tag{2.34}$$

$$y_{\mathrm{test},km} \le (y_l)_n + M\, b_{\mathrm{vis},2kmn} \tag{2.35}$$

$$x_{\text{test},km} \geq (x_u)_n - M\, b_{\text{vis},3kmn} \tag{2.36}$$

$$y_{\text{test},km} \geq (y_u)_n - M\, b_{\text{vis},4kmn} \tag{2.37}$$

$$\sum_{i=1}^{4} b_{\text{vis},ikmn} \leq 3 \tag{2.38}$$

$$k = 1, \ldots, n_v, \qquad m = 1, \ldots, n_t, \qquad n = 1, \ldots, n_o$$

where $[x_{\text{LOS},k}, y_{\text{LOS},k}]^T$ in Eq. 2.32 is a line-of-sight vector from the terminal point to the selected cost point for vehicle k, and the binary variable $\boldsymbol{b}_{\text{vis}}$ has four dimensions (obstacle boundary, vehicle, test point, and obstacle).

2.5 Target Visit

The highest goal of the mission is to search, attack, and assess specific targets. These tasks can be generalized as visiting goals and performing the appropriate action. The heading direction at the target can be included if assessment from a different angle is required. In this section, these goals are assumed to be allocated among several vehicles so that each vehicle has an ordered list of goals to visit. The goals are assumed to be set further apart than the planning horizon, so each vehicle can visit at most one goal point in each plan. The constraint on the target visit is active at only one time-step if a plan reaches the goal, and is relaxed at all of the waypoints if it does not. If a vehicle visits a goal, the rest of the steps in the plan are directed to the next goal. Therefore, only the first two unvisited goals are considered in MILP (*i.e.,* the number of goals n_g is set to be 2). The selection of the cost point and the decision of the time of arrival are coupled as

$$\sum_{i=1}^{n_c} b_{\text{cp},i1j} = \sum_{i=n_t}^{n_t+1} b_{\text{arrival},ij} \tag{2.39}$$

$$\sum_{i=1}^{n_c} b_{\text{cp},i2j} = \sum_{i=1}^{n_t-1} b_{\text{arrival},ij}; \qquad j = 1, \ldots, n_v \tag{2.40}$$

where $b_{\text{arrival},ij} = 1$ if the j^{th} vehicle visits the first target at the i^{th} time step, and equals 0 if not. Also, $i = n_t + 1$ indicates the first target was not reached within the planning horizon.

If a vehicle cannot reach the goal or reaches the goal at the final step, Eq. 2.39 must use the cost map built for the first goal. If a vehicle can visit the first goal in the planning horizon, Eq. 2.40 requires it to use the cost map built about the second goal.

A goal has a $v_i \Delta t$ by $v_i \Delta t$ square region of tolerance around it because the system is operated in discrete time. This tolerance is encoded using the intermediate variable $\boldsymbol{d}_{\text{err}}$

$$x_{ij} - x_{\text{goal},j} \geq -d_{\text{err},j} - M(1 - b_{\text{arrival},ij}) \tag{2.41}$$

$$y_{ij} - y_{\text{goal},j} \geq -d_{\text{err},j} - M(1 - b_{\text{arrival},ij}) \tag{2.42}$$

$$x_{ij} - x_{\text{goal},j} \leq +d_{\text{err},j} + M(1 - b_{\text{arrival},ij}) \tag{2.43}$$

$$y_{ij} - y_{\text{goal},j} \leq +d_{\text{err},j} + M(1 - b_{\text{arrival},ij}) \tag{2.44}$$

$$0 \leq d_{\text{err},j} \leq \frac{v_i \, \Delta t}{2} \tag{2.45}$$

$$i = 1, \ldots, n_t, \qquad j = 1, \ldots, n_v$$

If a vehicle j reaches its goal at time-step i, then $b_{\text{arrival},ij} = 1$ and the constraints in Eqs. 2.41 to 2.44 are active; if not, all the constraints are relaxed. Including $\boldsymbol{d}_{\text{err}}$ in the objective function causes the point of visit x_{ij} (where $b_{\text{arrival},ij} = 1$) to move closer to the goal. The heading constraints can be written in the same way

$$\dot{x}_{ij} \geq \dot{x}_{\text{goal},j} - v_{\text{err},j} - M_v(1 - b_{\text{arrival},ij}) \tag{2.46}$$

$$\dot{y}_{ij} \geq \dot{y}_{\text{goal},j} - v_{\text{err},j} - M_v(1 - b_{\text{arrival},ij}) \tag{2.47}$$

$$\dot{x}_{ij} \leq \dot{x}_{\text{goal},j} + v_{\text{err},j} + M_v(1 - b_{\text{arrival},ij}) \tag{2.48}$$

$$\dot{y}_{ij} \leq \dot{y}_{\text{goal},j} + v_{\text{err},j} + M_v(1 - b_{\text{arrival},ij}) \tag{2.49}$$

$$0 \leq v_{\text{err},j} \leq v_{\text{err,max}} \tag{2.50}$$

$$i = 1, \ldots, n_t, \qquad j = 1, \ldots, n_v$$

Again, constraints on the velocity at the target location are only active for the waypoint in the target region.

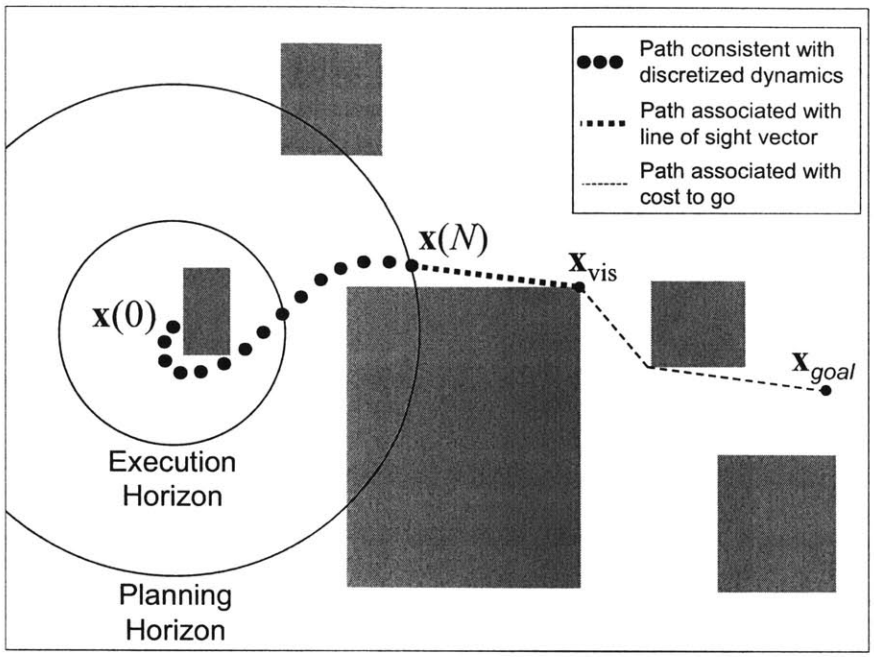

Figure 2-7: Line-of-sight vector and cost-to-go [14]

2.6 Cost Function

This formulation minimizes the time of arrival as a primary objective. Under the assumption that each vehicle flies at a constant speed, the minimization of distance is equivalent to the minimization of time. The distance to the goal is made up of three segments: ① initial position to the terminal point of the plan, ② terminal point to the cost point, and ③ the precalculated cost-to-go at the selected cost point. Since the distance from the initial position to the terminal point is constant, the MILP optimizer minimizes the sum of the length of the line-of-sight vector ② and the cost-to-go at the selected cost point ③ by choosing the best combination of terminal and cost-to-go points.

The length of the line-of-sight vector is a two norm of the line-of-sight vector defined in

Eq. 2.32. This is calculated in the MILP by minimizing an upper bound:

$$l_j \geq \begin{bmatrix} x_{\text{LOS},j} \\ y_{\text{LOS},j} \end{bmatrix} \cdot \boldsymbol{i}_k \tag{2.51}$$

$$\boldsymbol{i}_k = \begin{bmatrix} \cos\left(\dfrac{2\pi k}{n_l}\right) \\ \sin\left(\dfrac{2\pi k}{n_l}\right) \end{bmatrix} \tag{2.52}$$

$$j = 1, \ldots, n_v, \qquad k = 1, \ldots, n_l$$

where n_l is the number of unit vectors onto which the line-of-sight vector is projected and l_j gives an upper bound of the line-of-sight vector length for vehicle j. In this case, the objective function J_0 to be minimized is

$$J_0 = \sum_{j=1}^{n_v} (l_j + c_{\text{vis},j}) \tag{2.53}$$

where $c_{\text{vis},j}$ is a cost-to-go at the cost point selected by the j^{th} vehicle as defined in Eq. 2.29. The time-step of arrival (TOA) for the j^{th} vehicle is expressed as

$$TOA_j = \sum_{k=1}^{n_t+1} k\, b_{\text{arrival},kj}, \qquad j = 1, \ldots, n_v \tag{2.54}$$

Note that in Eq. 2.54, if $k = n_t + 1$ when $b_{\text{arrival},kj} = 1$, then the j^{th} vehicle will not reach the target in the planning horizon, thereby resulting in a higher cost. Combined with Eq. 2.53, the term TOA forms the objective function for the minimum time of arrival problem:

$$J_1 = \sum_{j=1}^{n_v} \left\{ \alpha \left(v_j \Delta t\right) TOA_j + l_j + c_{\text{vis},j} \right\} \tag{2.55}$$

where $v_j \Delta t$ converts the discrete time-step (TOA_j is an integer) into distance and α is a large weighting factor that makes the first term dominant. With a small α, the vehicle tends to minimize the cost-to-go, so that it arrives at the first goal at the terminal step in the

planning horizon. This is in contrast to the more desirable case of arriving at the first goal before the terminal step, and then minimizing the cost-to-go to the next goal. Thus the weight α must be larger than the number of steps required to go from the first goal to the next goal.

Finally, the term J_a, containing two auxiliary terms, is added to the primary cost in Eq. 2.55 to decrease the position and heading error at the target. The new cost to be minimized is defined as

$$J = J_1 + J_a \tag{2.56}$$

$$\text{where } J_a = \sum_{j=1}^{n_v} (\beta d_{\text{err},j} + \gamma v_{\text{err},j}) \tag{2.57}$$

Note that an overly large value of β results in "wobbling" near the target. The wobbling occurs as the vehicle attempts to maneuver, such that on the same time-step when it enters the target region, it arrives at the center of the target.

Also note that the equations involving the dynamics, constraints, and costs are not dependent of the number of vehicles except for vehicle collision avoidance, and thus these can be solved separately if vehicle collision avoidance is not an issue.

2.7 Example

A simple example is presented here to show the validity of this model. The model is described in the modelling language AMPL, which calls CPLEX 7.1 as a MILP solver. The computation is done on a Windows-based PC with CPU speed 2.2GHz (Pentium 4) and 512 MB RAM.

Figure 2-8 shows a trajectory where a single vehicle starts in the left of the figure and goes to a destination on the right, designated by a circle. Three obstacles require almost the tightest turn for the vehicle. Solid lines show actual obstacle boundaries and dotted lines are the expanded obstacles. The list of parameters are:

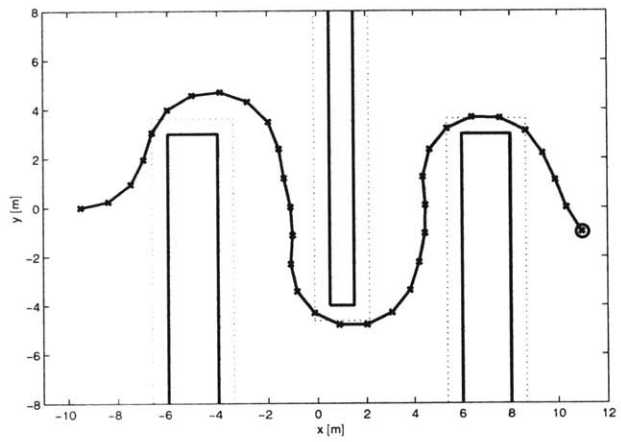

Figure 2-8: Trajectory with minimum speed constraints

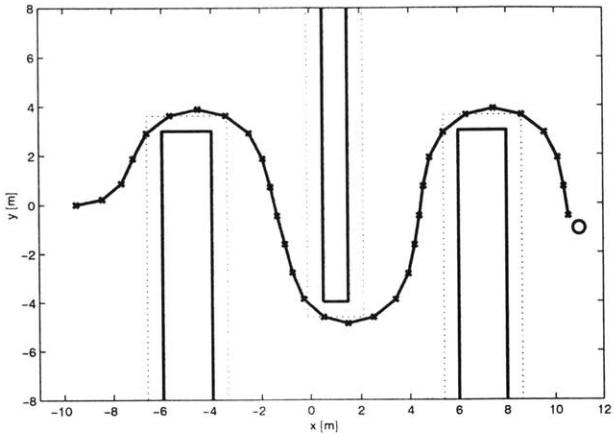

Figure 2-9: Trajectory without minimum speed constraints

- $v = 1$
- $\Delta t = 1.2$
- $r_{\min} = 2.8$
- $n_a = 20$
- $n_p = 5$
- $n_e = 1$
- $n_{v_{\max}} = 20$
- $n_{v_{\min}} = 10$
- $n_l = 36$
- $M = 100$
- $M_v = 2v_{\min}$

Note that the optimal trajectory has waypoints on the obstacle boundaries. Figure 2-9 shows a trajectory without minimum speed constraints. Since it is still a minimum time problem, there is not much difference in the trajectory. However, without minimum speed constraints, the vehicle can slow down to make a tighter turn, making the effective minimum turn radius smaller than that in Figure 2-8. Thus, the time-step of arrival in Figure 2-9 is two steps less than that in Figure 2-8.

Figure 2-10 shows a speed profile and Figure 2-11 shows a computation time for each plan generation. Points marked with small dots show the case without minimum speed constraints, and points marked with $\times$ are the cases with minimum speed constraints. When a tight turn is required, the effect of minimum turn constraints on computation time is readily apparent. However, the computation time is still short enough to apply this receding horizon controller to real-time trajectory generation. Points with $\circ$ have an unnecessarily large M where $M_v = 200v_{\min}$. This tends to slow down the computation where minimum

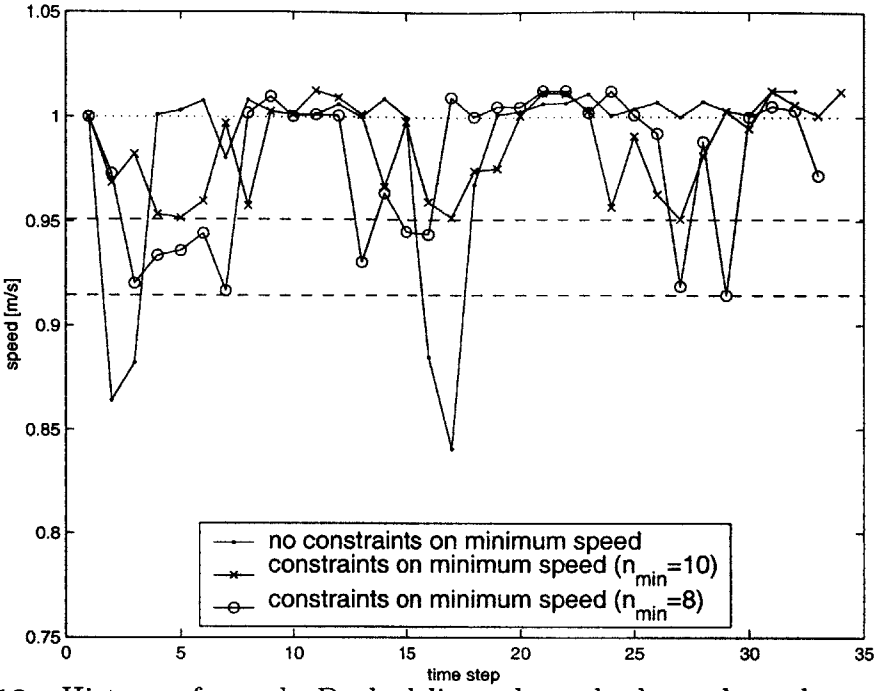

Figure 2-10: History of speed. Dashed lines show the lower bounds on the speed. The case with $n_{v_{\min}} = 10$ keeps the speed higher than the case with $n_{v_{\min}} = 10$.

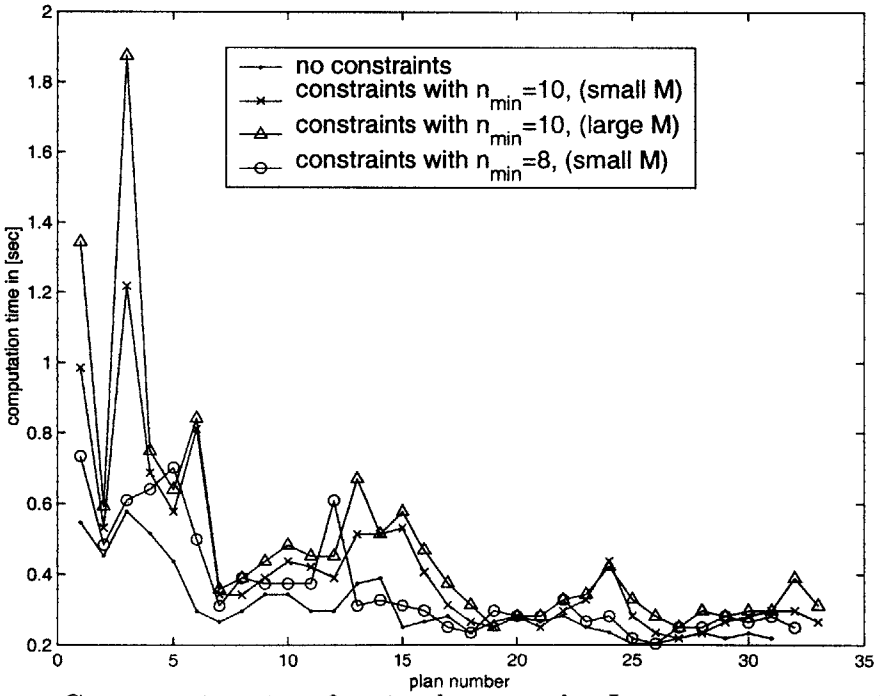

Figure 2-11: Computation time for simple example. Looser constraints ($n_{v_{\min}} = 8$) results in less computation time. The spike observed at the third plan with $n_{v_{\min}} = 10$ is avoided by $n_{v_{\min}} = 8$. Overly large M slows down the computation.

turn constraints are active, which suggests the "big M" should be set as small as possible.

To compare with $n_{v_{\min}} = 10$, the resolution of the minimum speed constraints is reduced to 8. Reducing $n_{v_{\min}}$ results in much shorter computation time, as shown in Figure 2-11. It allows the vehicle to slow down to 91% of the maximum speed[1], whereas $n_{v_{\min}} = 10$ maintains the speed to within 95% of the maximum speed. Thus in this example, a 40% reduction in the computation time was obtained with only a 4% change in the minimum speed.

2.8 Conclusions

This chapter extended the previous work and posed the multi-vehicle multi-waypoint minimum time-of-arrival trajectory generation problem in MILP form. The selection of the goal is expressed in MILP form using binary variables that include other logical constraints such as collision avoidance. The point mass model captures the essential features of the aircraft dynamics such as speed and minimum turning radius constraints. The detailed analysis also clarified the effect of the time discretization. The non-convex minimum speed constraints have also been added to the problem to better capture the vehicle behavior in highly constrained environments. The effect on the computation time was also examined.

[1]The lower bound for the speed is obtained by finding the largest regular polygon that fits inside the regular polygon for the maximum speed constraints.

Chapter 3

Stable Receding Horizon Trajectory Designer

This chapter presents a stable formulation of the receding horizon trajectory designer. The "stability" of the trajectory designer is defined as a guaranteed arrival at the goal. In the formulation presented in the previous chapter, a straight line approximation gives a good cost estimate, but it can require too tight a turn because it does not account for the vehicle dynamics. Replanning is usually able to find a dynamically feasible path around the line segment path. However, in an extreme case described in Section 3.1, the large heading discontinuities when the line segments join leads to an infeasible problem in the detailed trajectory design phase. This situation is avoided by introducing three turning circles per corner when building the cost map and extending the planning horizon sufficiently far enough out beyond the execution horizon. Section 3.2 discusses the visibility graph that constructs collision free paths in the world map. The modified Dijkstra's algorithm presented in Section 3.3 ensures there exists a feasible turn from one corner to another, and Section 3.4 discusses how to extract the necessary part of the cost map for the MILP optimization. Finally, Section 3.5 reveals sufficient conditions required (based on the existence of a feasible path) in the detailed trajectory design phase to prove the stability of the receding horizon controller.

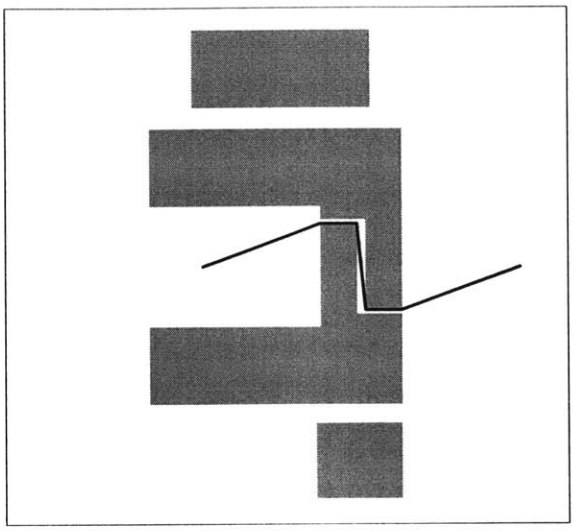

Fig. 3-1: Straight line approximation goes through the narrow passage

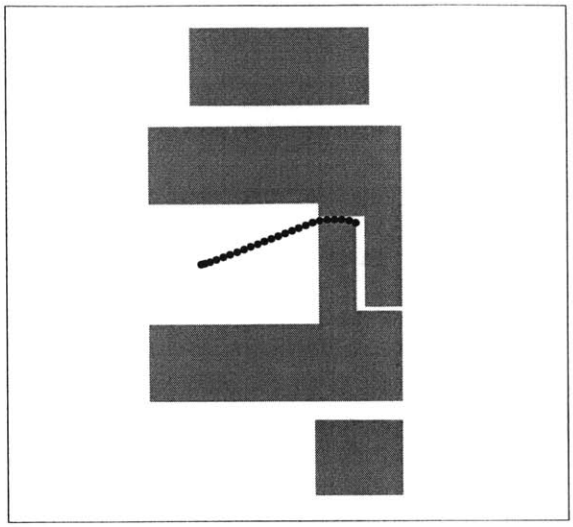

Fig. 3-2: Infeasible problem in the detailed trajectory design phase

3.1 Overview

The basic receding horizon controller [14] uses an aircraft dynamics model described in Eqs. 2.2 to 2.13 over the planning horizon in the detailed trajectory generation phase, and a simple kinematic model (*i.e.,* collision free straight line segments) beyond it. The trajectory optimization problem can become infeasible if there is a large difference between the straight line approximation and the *kinodynamically feasible* trajectory that has a minimum turning radius. Figures 3-1 and 3-2 illustrate the case where kinodynamically infeasible straight line segments lead to an infeasible trajectory design problem [14].

One way to avoid this situation is to prune, before constructing a cost map, all of the corners that require a large turn or have other obstacles around them. This ensures that any incoming direction at every corner can result in a feasible turn. However, this could lead to an overly conservative path selection (*e.g.,* "go around all the obstacles").

Another approach is to place a turning circle at each corner when constructing a cost map, and enforce the rule that the vehicle moves towards the arc of the circle, not the corner. Ref. [15] introduced binary variables to encode the *join* and *leave* events on the turning circles, but these binaries complicate the MILP problem and make it harder to solve

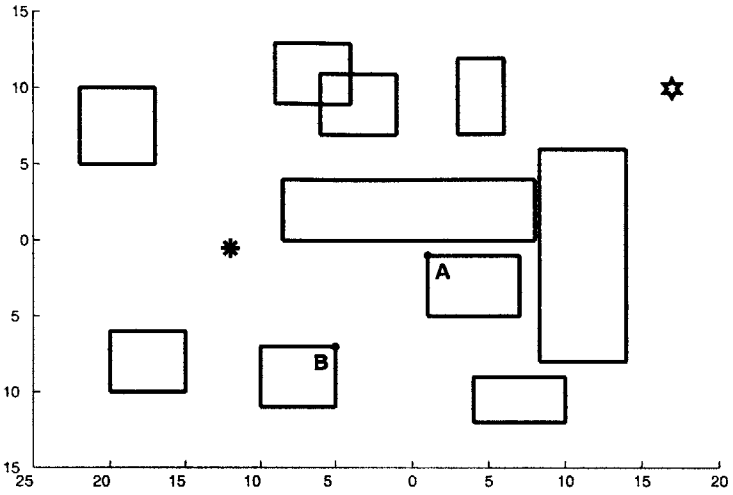

Figure 3-3: Typical scenario populated with obstacles

while restricting the freedom of the trajectory designer to choose a path.

A new approach presented in this chapter ensures the existence of a kinodynamically feasible turn at each corner by applying a modified Dijkstra's algorithm when constructing the cost map. When searching for the shortest path, this algorithm rejects a sequence of nodes if the turning circles cannot be suitably placed (*i.e.*, a kinodynamically infeasible sequence). The generated tree of nodes gives the shortest distance from each node to the goal along the straight lines in the regions where a feasible path is guaranteed to exist. When optimizing the trajectory using RHC, the planning horizon is then extended beyond the execution horizon such that while executing the plan, the vehicle will always stay in the regions from which a feasible path to the goal exists.

3.2 Visibility Graph

This section extends the graph search algorithm from Ref. [13] which is used to generate a coarse cost map for path planning in an obstacle field. Nodes for the graph are the obstacle corners and the goal point. This is a good approximation, because with very fast turning dynamics, the shortest path from one node to another would consist of the straight line

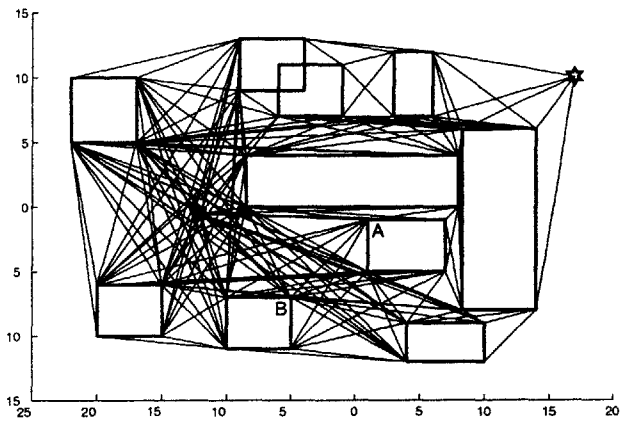

Fig. 3-4: Visibility graph

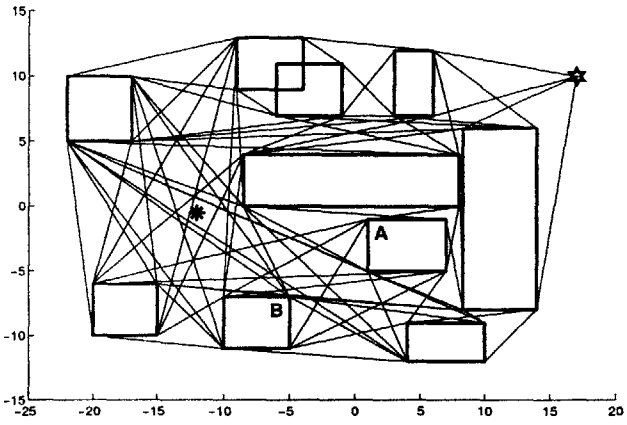

Fig. 3-5: Visibility graph after pruning

segments provided by the visibility graph. Figure 3-3 shows a typical scenario where many obstacles reside between the vehicle location (marked as the $*$ middle left) and the goal (marked as a star in the upper right). Figure 3-4 shows all the collision free connections between nodes. Two connected nodes in this figure are "visible" from each other.

Before running the Dijkstra's algorithm to solve for the shortest path toward the single source node, pruning some connections that will never be selected reduces the computation time. In Figure 3-4, some connections are unnecessary since the vehicle will never follow these paths. For example, the connection between node A and B can be pruned because a vehicle going from A to B will collide with the obstacle to which node B is attached. More generally, if a connected line segment is extended by ϵ at both ends, and either extended end point is inside an obstacle, that connection can be removed. Figure 3-5 shows a visibility graph after pruning – the number of connections has decreased from 367 to 232.

3.3 Modified Dijkstra's Algorithm

This section extends the previous way of constructing the cost map, described in Section 3.2, to ensure the existence of kinodynamically feasible paths around the straight line segments. Proper placement of turning circles is critical in the less conservative estimate of the existence of a feasible turn. An analytical way of placing collision free circles is introduced in Subsec-

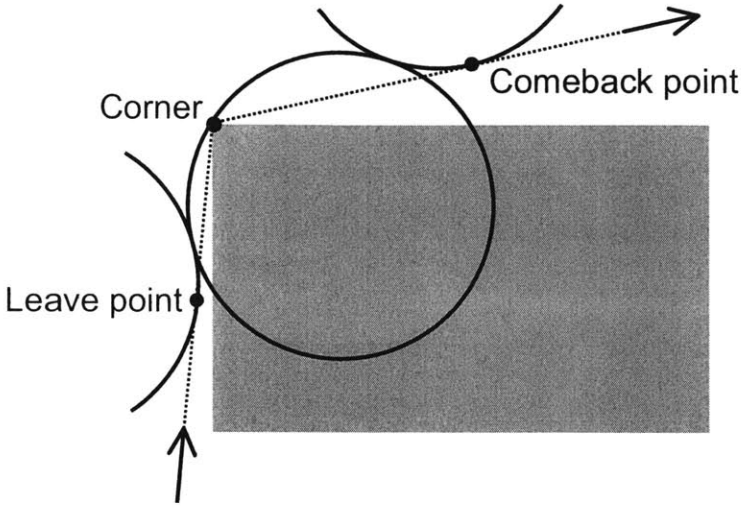

Figure 3-6: Three turning circles at obstacle corner

tion 3.3.1. This circle placement algorithm is embedded in the modified Dijkstra's algorithm, as discussed in Subsection 3.3.2. Combined with the visibility graph obtained in Section 3.2, the modified Dijkstra's algorithm that incorporates both kinematics and dynamics yields a reliable cost map. It also produces upper and lower bounds for the shortest-distance problem.

3.3.1 Turning Circles Around a Corner

Three Circles

The optimal trajectory of an aircraft flying at a constant speed with limited lateral acceleration is depicted as a series of straight line segments and arcs of the minimum turning circle [25]. Figure 3-6 shows three turning circles, the arcs of which compose a path flyable by the vehicle when it changes from one straight line to another. The vehicle leaves the original straight line path at a "leave point", make a turn with the maximum side force allowed, passes around the obstacle corner, and then aligns its heading to the next straight line at a "comeback point". The straight line segments in Figure 3-6 are the connections in the visibility graph, guaranteed to be collision free as stated in Section 3.2. Two more things must be verified in order to construct a tree of kinodynamically feasible paths. First, the turning circles must be collision free (*i.e.*, not intersect any obstacles). Second, when

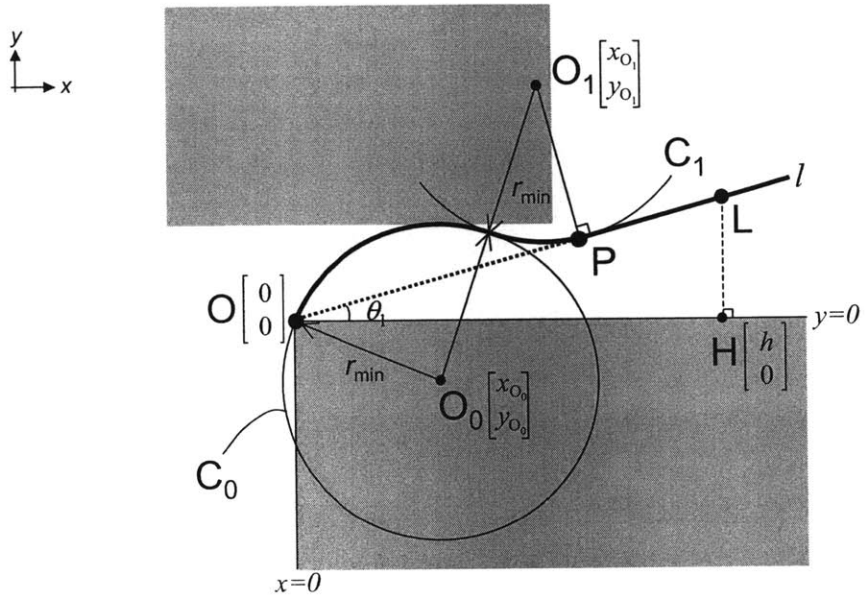

Figure 3-7: Circle placement problem

constructing a tree backwards from a goal[1], a comeback point around a corner must not go over the leave point of its previous corner. This second condition requires that the vehicle must come back to the straight line and align its heading with it, before deviating from the straight line to make the next turn.

Circle Placement Problem

Without loss of generality, an upper left corner of an obstacle is examined. Figure 3-7 illustrates the notation for the circle placement problem. An upper left corner O of an obstacle can be assumed to be at the origin, and a straight line l connects O and its previous corner. A leave point L of the previous corner is placed on l. "Corner circle" C_0 with radius $r_{\min}$ passes through the obstacle corner O. "Comeback circle" C_1 with radius $r_{\min}$ is tangent to both circle C_0 and the straight line l. Then, the circle placement problem given a visibility graph is stated as follows:

Given L, determine the center O_0 of C_0, and the center O_1 of C_1, such that the

[1]Therefore the "previous" corner means a corner which is one node closer to the goal.

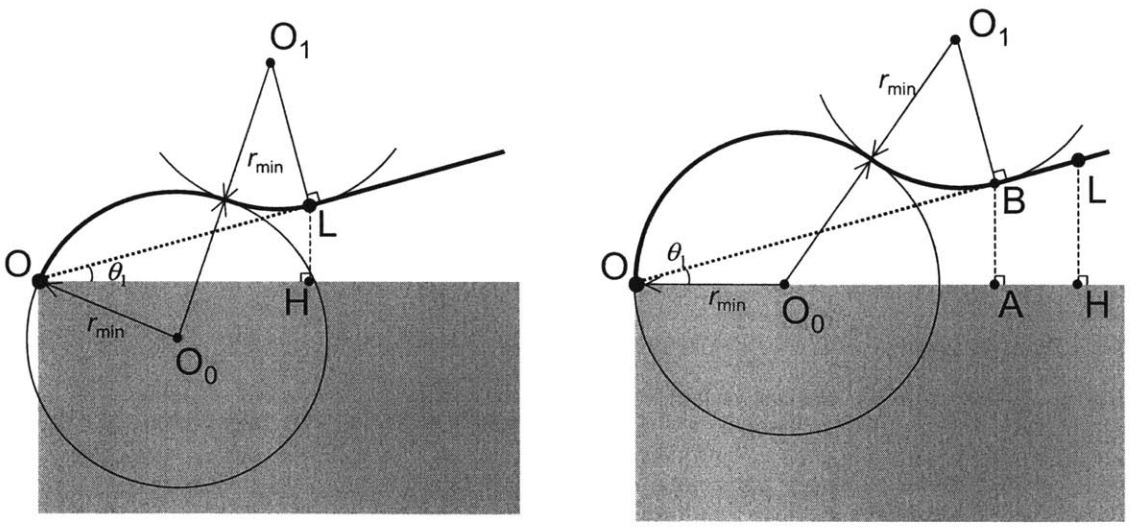

(a) Leave point is close to the corner

(b) Leave point is far from the corner

Figure 3-8: Two cases for determining horizontal distance

path from O to L along the arcs of C_0 and C_1 and the straight line l is collision free, while keeping the comeback point P as far from the corner O as possible.

Let $[x_{O_0}, y_{O_0}]^T$ and $[x_{O_1}, y_{O_1}]^T$ denote the center of the circle C_0 and C_1 respectively, and let θ_1 denote the angle between the straight line l and the obstacle boundary $y = 0$.

The solution to this problem is presented in the following six steps. Note that there are two distances that play important roles in placing these circles. First, the separation distance $y_{\min}$ is defined as the minimum distance between an obstacle boundary $y = 0$ and the other obstacles above it (*i.e.*, $y \geq 0$). Second, the horizontal distance $x_{\max}$ is a width in the x direction over which the locations of other obstacles are examined to find the minimum separation distance $y_{\min}$.

Step 1. The first step is to determine the width in the x direction over which the location of the other obstacles are examined when solving for the separation distance. Figure 3-8 shows two different cases in obtaining the horizontal distance $x_{\max}$, given a leave point L of the previous corner. Let h denote the distance between corner O and a point H, where H completes the right triangle OLH, as shown in Figure 3-7. If the leave point L of the previous

corner is "close" to the corner, as in Figure 3-8(a), only the region OH needs to be examined to find the minimum separation distance. If it is "far", as in Figure 3-8(b), the center of the corner circle is set temporarily at $[0, r_{\min}]^T$ so that the comeback point P associated with corner O gets as close as possible to the leave point L of the previous corner. Note that in Figure 3-8(b), if the thick line turns out to be collision free, any incoming direction to the corner O (from $y \leq 0$) is able to produce a kinodynamically feasible turn that joins the straight line before reaching the leave point L. The "close" case and the "far" case are held together to define the horizontal distance $x_{\max}$ as follows.

$$\begin{aligned} x_{\max} &= \min(\overline{\mathrm{OH}}, \overline{\mathrm{OA}}) \\ &= \min\left(h, \frac{r_{\min}(1 + \sqrt{3 + 2\tan^2\theta_1 - 2\tan\theta_1\sqrt{1+\tan^2\theta_1}})}{1+\tan^2\theta_1}\right) \end{aligned} \tag{3.1}$$

where the second term is the length of $\overline{\mathrm{OA}}$ in Figure 3-8(b) and is analytically obtained[2]. The comeback point P has not yet been determined.

Step 2. The minimum separation distance $y_{\min}$ is obtained by examining obstacle corners and lines in the region $\left\{(x,y)\middle|\, 0 \leq x \leq x_{\max},\ x\tan\theta_1 \leq y\right\}$, so that there are no obstacles in the region $\left\{(x,y)\middle|\, 0 \leq x \leq x_{\max},\ x\tan\theta_1 \leq y \leq y_{\min}\right\}$. It guarantees that if two arcs of C_0 and C_1 stay in the region $\left\{(x,y)\middle|\, 0 \leq x \leq x_{\max},\ x\tan\theta_1 \leq y \leq y_{\min}\right\}$, then there exists a kinodynamically feasible path from O to L, which is a connection of the two arcs of C_0 and C_1 and the straight line l.

Step 3. When determining the comeback point P, two cases must be considered, as shown in Figure 3-9, depending on the separation distance $y_{\min}$. If the separation distance is large enough as in Figure 3-9(a), the leave point L in Figure 3-8(a) or point B in Figure 3-8(b) becomes the comeback point P associated with the corner O. If the separation distance is too small, as in Figure 3-9(b), the intersection I of two lines $y = y_{\min}$ and straight line l becomes the comeback point P since the region $\left\{(x,y)\middle|\, y > y_{\min},\ y > x\tan\theta_1\right\}$ is not guaranteed to be collision free. Therefore, the distance L between corner O and comeback

[2]This result was analytically obtained using Mathematica.

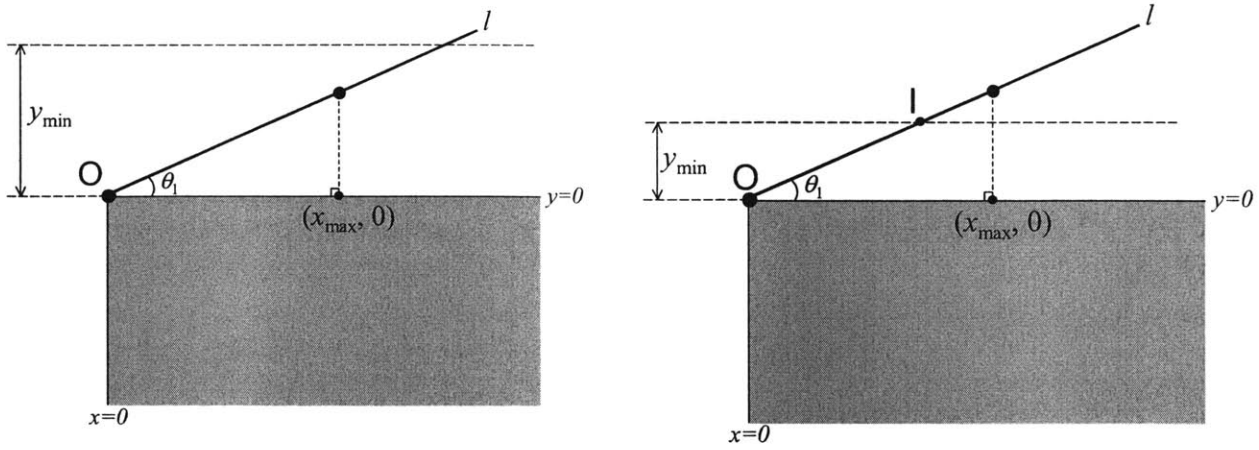

(a) (b)

Figure 3-9: Two cases for determining comeback point depending on separation distance

point P (along l) is given by

$$L = \min\left\{\frac{x_{\max}}{\cos\theta_1}, \frac{y_{\min}}{\sin\theta_1}\right\} \tag{3.2}$$

Step 4. Given L defined in Eq. 3.2, two circles are placed such that one of them passes through the corner O, the other is tangential to the straight line l at comeback point P, and the two arcs are smoothly connected to each other. The distance d between obstacle boundary $y = 0$ and the top of the circle C_0 is analytically obtained as:

$$d = r_{\min} - \frac{(2{r_{\min}}^2 - L^2)(r_{\min} + L\tan\theta_1) - L(r_{\min}\tan\theta_1 - L)\sqrt{8{r_{\min}}^2 - L^2}}{2({r_{\min}}^2 + L^2)\sqrt{1+\tan\theta_1}} \tag{3.3}$$

Step 5. At this point in the development, the comeback point is known to be connectable from the corner O by two arcs, and there are no obstacles in region $\left\{(x,y)\middle| 0 \le x \le x_{\max},\, x\tan\theta_1 \le y \le y_{\max}\right\}$. However, these arcs could intersect obstacles since the top of the circle can be beyond the comeback point in the y direction, as shown in Figure 3-10(b). Therefore, the top of the circle C_0 is restricted in the y direction by

$$d_{\max} = \min(d,\, y_{\min}) \tag{3.4}$$

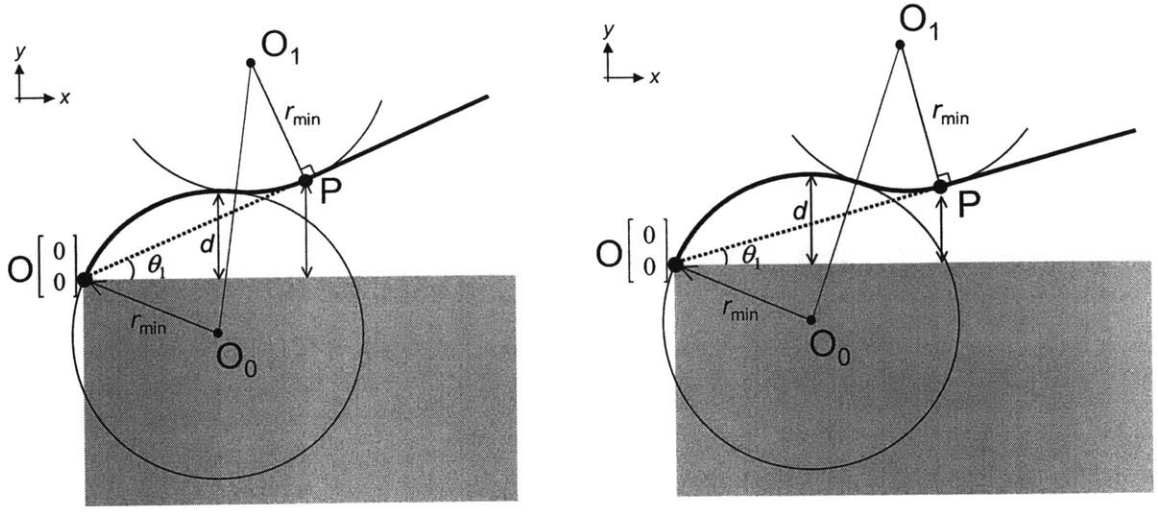

(a) Top of the circle is lower than P

(b) Top of the circle is higher than P

Figure 3-10: Two cases for determining the center O_0 of circle C_0

This restriction pushes the point P closer to the corner O and puts the leave point L farther from O, which will require an earlier deviation from the straight line when making a turn around the corner O.

Step 6. Finally, the position of the circles C_0 and C_1 is fixed as

$$\begin{bmatrix} x_{O_0} \\ y_{O_0} \end{bmatrix} = \begin{bmatrix} \sqrt{r_{\min}^2 - (r_{\min} - d_{\max})^2} \\ d_{\max} - r_{\min} \end{bmatrix} \tag{3.5}$$

$$\begin{bmatrix} x_{O_1} \\ y_{O_1} \end{bmatrix} = \begin{bmatrix} x_{O_0} \\ y_{O_0} \end{bmatrix} + 2r_{\min} \begin{bmatrix} \cos\phi_1 \\ \sin\phi_1 \end{bmatrix} \tag{3.6}$$

$$\phi_1 = \frac{\pi}{2} + \theta_1 - \beta$$

$$\beta = \arccos\left\{\frac{1 + \sin(\theta_1 + \alpha)}{2}\right\}$$

$$\alpha = \left|\arctan\frac{y_{O_0}}{x_{O_0}}\right|$$

where the angles ϕ_1 and α are shown in Figure 3-11. The difference between the path length along the straight line $\overline{OP}$ and the one along the two arcs $\widehat{OQ} + \widehat{QP}$ is also analytically

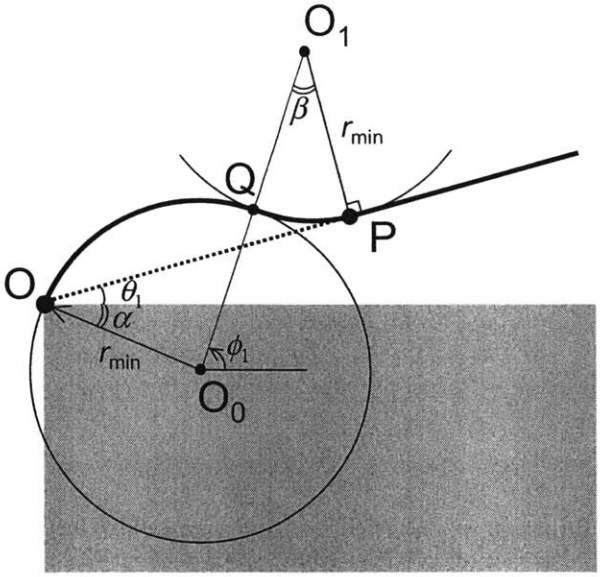

Figure 3-11: Angles used in the calculation of the centers of circles

obtained as

$$\Delta J = \left(2\beta + \frac{\pi}{2} - \theta_1 - \alpha\right) r_{\min} - \left[\left\{1 + \sin(\theta_1 + \alpha)\right\}\tan\beta + \cos(\theta_1 + \alpha)\right] r_{\min} \qquad (3.7)$$

Note that the path length along the two arcs gives an upper bound of the optimal path length. Typical values for the difference ΔJ are shown in Table 3.1 for a given $d_{\max}$ and θ_1.

This six step procedure analytically determines the position of the two circles C_0 and C_1 whose arcs constitute kinodynamically feasible paths from the corner O to the comeback point P.

Table 3.1: Difference ΔJ in the distance where $r_{\min} = 1$. θ_1 is expressed in degrees. $*$ represents that the circle and the straight line do not intersect.

		$d_{\max}$		
		0.1	0.5	1.0
θ_1	0	0.03	0.30	0.93
	30	$*$	0.04	0.30
	60	$*$	0.00	0.04

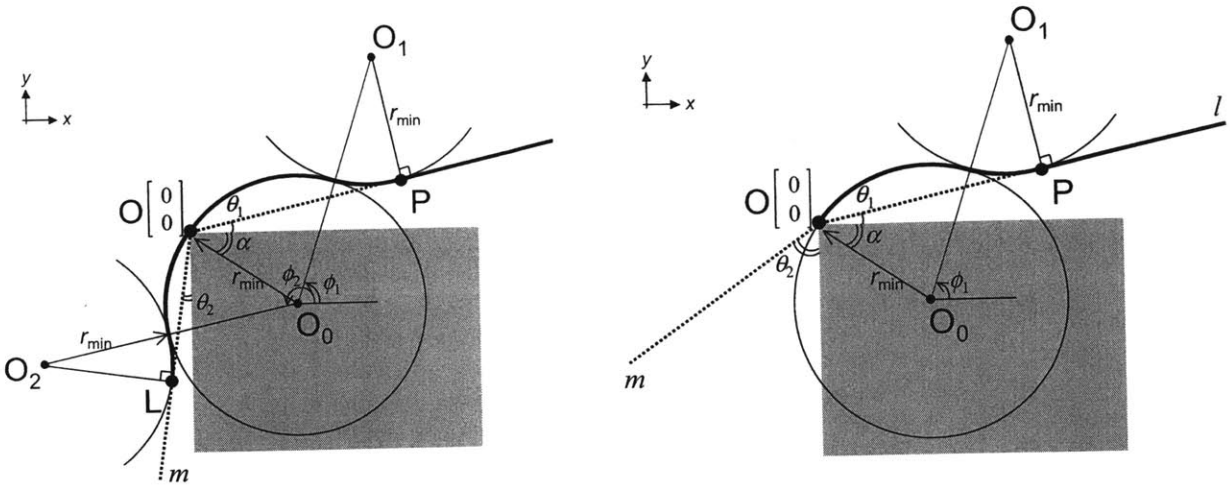

(a) Tight incoming direction

(b) No need to place leave circle

Figure 3-12: Two cases for determining the center O_2 of circle C_2

Leave Circle

The third "leave circle" C_2 is placed using another straight line m passing through the corner O to the next corner. Let θ_2 denote the angle that the line m forms with an obstacle boundary $x = 0$ as shown in Figure 3-12(a). C_2 must be tangential to both circle C_0 and the straight line m, and the contact point of the circle C_2 and the line m is the leave point for corner O. The center O_2 of circle C_2 is geometrically solved as

$$\begin{bmatrix} x_{O_2} \\ y_{O_2} \end{bmatrix} = \begin{bmatrix} x_{O_0} \\ y_{O_0} \end{bmatrix} + 2r_{\min} \begin{bmatrix} \cos\phi_2 \\ \sin\phi_2 \end{bmatrix} \tag{3.8}$$

$$\phi_2 = \pi - \theta_2 + \arccos\left\{\frac{1+\cos(\theta_2 - \alpha)}{2}\right\}$$

If the two arcs of C_0 and C_2 from the corner O to the leave point L intersect any obstacles, then the change from straight lines l to m around the corner O requires a tighter than dynamically allowable turn, and the connection is rejected. If the leave point L placed on m does not lie between the corner O and its next node, the vehicle is forced to leave the straight line m before reaching it, which is infeasible. In this case, the connection between l and m is also rejected. Note that if the angle between m and l is wide enough, as shown

in Figure 3-12(b), $\theta_2 \geq \alpha$, and the straight line m does not intersect with circle C_0 in the region $x < 0$. Any incoming direction $\theta\,(\geq \alpha)$ will result in a feasible turn, and there is no need to place a leave circle. In this case, the leave point L is placed at the corner O, which is used in Step 1 for the next corner.

3.3.2 Modified Dijkstra's Algorithm

The discussion in the previous section demonstrated that it is a pair of arcs[3], and not a node or one arc, that has to be pruned if vehicle dynamics are considered. A modified Dijkstra's algorithm is presented in this section that accommodates the rejection criteria for joining two arcs when searching for the shortest path.

The original Dijkstra's algorithm [27] finds the shortest path to all nodes from an origin node on a graph $G = (\mathcal{N}; \mathcal{A})$, where $\mathcal{N}$ is a finite set of nodes and $\mathcal{A}$ is a collection of arcs joining a pair of nodes that are members of $\mathcal{N}$. Weight $w_{ij}(\geq 0)$ is associated with an arc (i, j) in a set of arcs $\mathcal{A}$. This algorithm involves the labelling of a set of fixed nodes $\mathcal{P}$, of which the shortest node distances D_j from the origin node to each node $j \in \mathcal{N}$ has been found.

When making a cost map for the receding horizon trajectory design problem, $\mathcal{N}$ is a set of obstacle corners and goals and w_{ij} is the straight line distance between each pair of nodes. The weight w_{ij} is set to ∞ if node i is not visible from node j due to the obstacles. The goal is regarded as an origin node in the algorithm.

Dijkstra's algorithm chooses a node with a minimum distance label, but the modified Dijkstra's algorithm presented here chooses a node which has a minimum distance label, and from which a kinodynamically feasible connection to the current node is guaranteed to exist.

[3]In this subsection, the word "arc" is used as a term in the graph theory, which represents a connection between two nodes.

Algorithm Overview

The index of the goal node can be set to be 1. The modified Dijkstra's algorithm then consists of the following procedure:

1. Set current node $i = 1$, and initialize:

$$\mathcal{P} = \{1\}$$
$$D_j = \begin{cases} 0 & (j = 1) \\ w_{1j} & (j \neq 1) \end{cases} \tag{3.9}$$

2. Place the leave point for the goal on the goal.
3. Set node i as the successor of each node j. A successor node is the next node on the path toward the goal.
4. Find the next closest node from the set of unfixed nodes[4], and set it as a new current node i:

$$i := \arg\min_{j \notin \mathcal{P}} D_j \tag{3.10}$$

5. Place the two turning circles C_0 and C_1 around node i.
6. Fix node i, and update the set $\mathcal{P}$ of fixed nodes:

$$\mathcal{P} := \mathcal{P} \cup \{i\} \tag{3.11}$$

7. If all nodes in $\mathcal{N}$ are also in the set $\mathcal{P}$ of fixed nodes, terminate.
8. For all the nodes that are unfixed and visible from the current node i, *i.e.*, for each $\{j \mid j \notin \mathcal{P}, w_{ij} \neq \infty\}$:

   (a) Place a leave circle around i, and put a leave point for i on a straight line connecting i and j.

[4] "Unfixed" means that the shortest path to the goal has not been found.

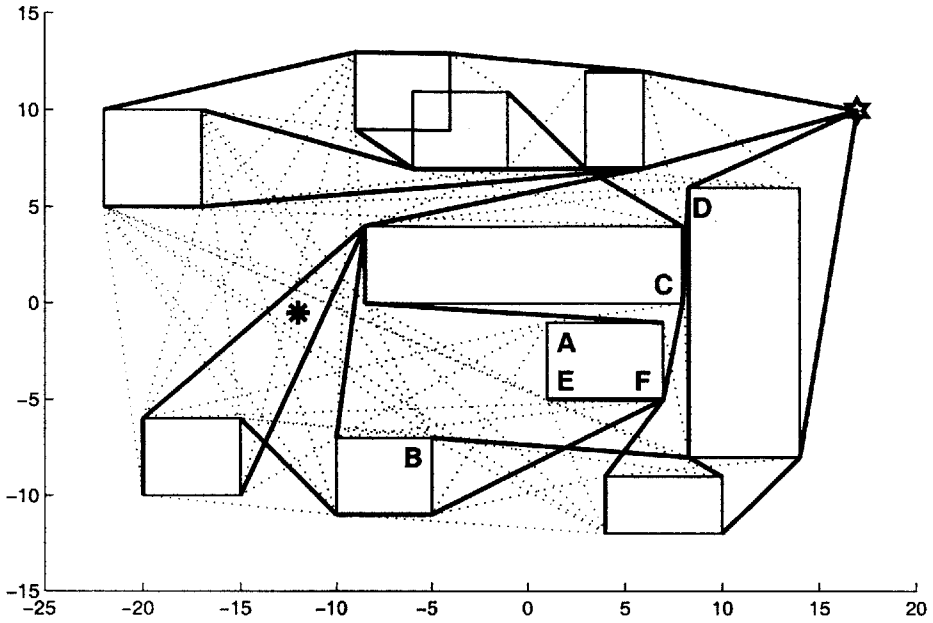

Figure 3-13: Tree of shortest paths

(b) Check the feasibility of the connection. If the leave point does not lie between i and j, then reject the connection, pick the next j, and go to 8a. If the path from i to j along the corner circle, leave circle, and the straight line i-j is not collision free, then reject the connection, pick the next j, and go to 8a.

(c) Update the temporary labels

$$D_j := \min(D_j, w_{ij} + D_i) \tag{3.12}$$

(d) If D_j is updated with $w_{ij} + D_i$, then set i as the successor of node j, and also update the separation distance for j in terms of connection i and j.

(e) Pick the next j and go to 8a.

9. Go to step 4 for next iteration

This procedure produces a tree of nodes with the goal node at its end. D_j gives the shortest distance from j to the goal along the straight line about which a kinodynamically feasible path is guaranteed to exist. Figure 3-13 shows a cost map made from Figure 3-5

after running the modified Dijkstra's algorithm. The dotted lines are the visibility graph in Figure 3-5. A minimum turning radius $r_{\min} = 2.5$ is used. Note that the corner A is not connected to the corner C since the path A-C-D requires tighter than dynamically allowable turns in order to avoid collisions, and hence this sequence would be kinodynamically infeasible. Corner A is also not connected to the tree E-F-C-D because the leave point of the connection E-A does not lie between the two nodes E and A due to the tight turns required for the tree E-F-C-D. If the minimum turning radius was reduced ($r_{\min} = 1$), the path A-C-D does not require a turning radius smaller than $r_{\min}$. In that case, node A has the tree C-D as its successor.

3.4 Cost Points

3.4.1 Corner Selection

Although the cost map obtained in the previous section provides a tree of nodes along which a kinodynamically feasible path is guaranteed to exist, not all the nodes can be passed to the MILP optimization process as cost points or candidate visible points since the formulation presented in Chapter 2 does not necessarily follow the precedence of nodes. Figure 3-14 illustrates that the violation of precedence can lead to an infeasible problem. Two or three circles with radius $r_{\min}$, discussed in Subsection 3.3.1, are also placed at each corner A, B, and C. In this example, the modified Dijkstra's algorithm guarantees that the tree A-B-C-D is a feasible sequence, but the vehicle should not aim directly for corner C following the dashed line because it cannot turn around the corner C with its minimum turning radius.

Taking into account the precedence of cost points when generating the cost map solves this issue. In order to form a list of "stable" cost points[5], the following algorithm is applied before calling the MILP optimization solver:

Step 1. Find all the points visible from the initial location of the vehicle and include them in the set of candidate cost points. This visibility is based solely on the straight lines,

[5]As long as the vehicle aims for these points, the stability of the trajectory is guaranteed.

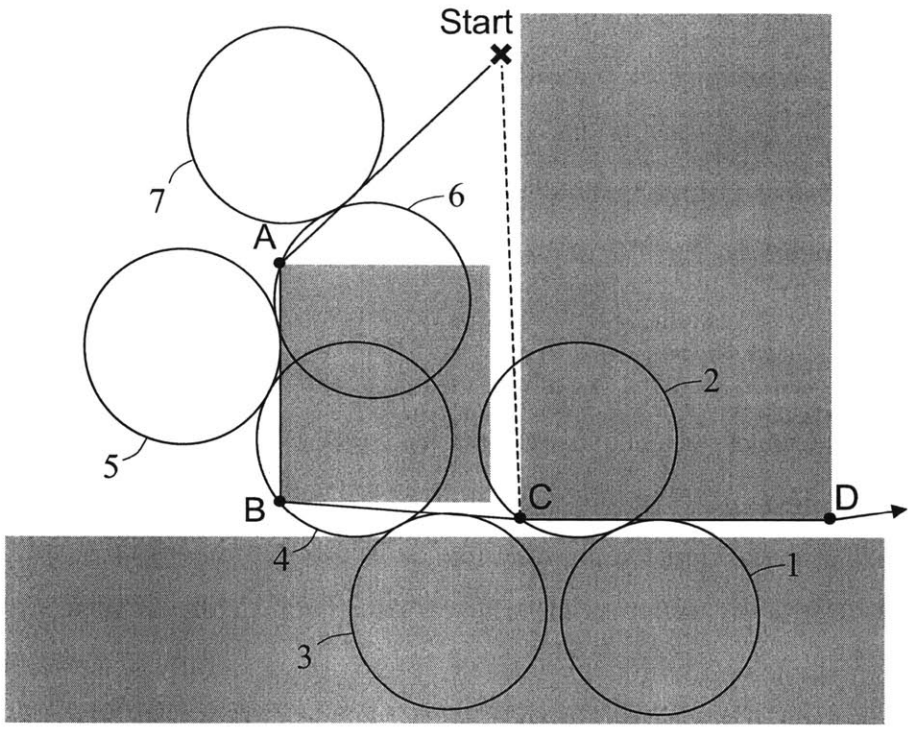

Figure 3-14: Precedence of cost points. The vehicle starts at the top (×), and goes to the right of the figure by going through the narrow passage C-D. The corner circle (2) at C intersects the obstacle to its left, and can not be directly connected to the start position. There is no leave circle placed around corner C since the straight line BC does not intersect circle 2. The leave circle (5) for corner B is the same as the comeback circle for corner A since an obstructive turn is required at corner B and the distance $\overline{AB}$ is short.

and the connection might require a dynamically infeasible turn at the candidate cost points.

Step 2. For each visible point, check if the connection is feasible by considering the circles placed around the corner, as discussed in Subsection 3.3.1. From the candidate cost points obtained in the previous step, eliminate points that are visible but are not connectable with a dynamically feasible path. The remaining points form a list of cost points.

Step 3. Calculate the distance between the initial location and each cost point. If it is shorter

than the length of the planning horizon, add successors of the cost point (one at a time) to the list of cost points until the tree starting from the cost point has one and only one node beyond the planning horizon. This keeps the number of nodes in the list of cost points as small as possible, and prevents the vehicle from skipping ordered nodes.

Figures 3-15 to 3-17 show a resulting list of cost points after executing each step of the algorithm above. Corners with • marks in Figure 3-15 represent nodes visible from the initial location $*$. Corners with square marks in Figure 3-16 represent points that are visible from the initial point and feasibly connectable to it. Note that the points with • in the left of the figure are not considered to be feasibly connectable to the initial point, since a vehicle going from the initial point $(*)$ to these nodes will require a sharp turn around the nodes in order to join the kinodynamically feasible tree. More generally, if an angle between the incoming direction to the corner and the outgoing direction from it is less than $\pi/2$, then the connection is regarded as infeasible. The visible and connectable points obtained after Step 2 form a list of cost points (marked with squares), but some points are added to this list, as discussed in Step 3, to form a complete list of cost points, which are shown in Figure 3-17. The planning horizon in this example has a length of 15 units. Point F has been added to the list in the operation of Step 3, but C was not included.

As described above, every time the receding horizon controller starts solving an optimization problem, only a limited number of points on each tree of cost nodes are extracted and used in the MILP. This ensures that the resultant trajectory is stable while retaining the freedom to choose the path along the way. Note that (for a static environment) the stored cost map remains unchanged and this process is not computationally intensive.

3.4.2 Effect on the Computation Time

The node pruning algorithm presented above not only ensures that the problem is feasible, but it also reduces the computation load. Figure 3-18 shows an environment densely populated with obstacles. The same optimal trajectory was obtained using the old and

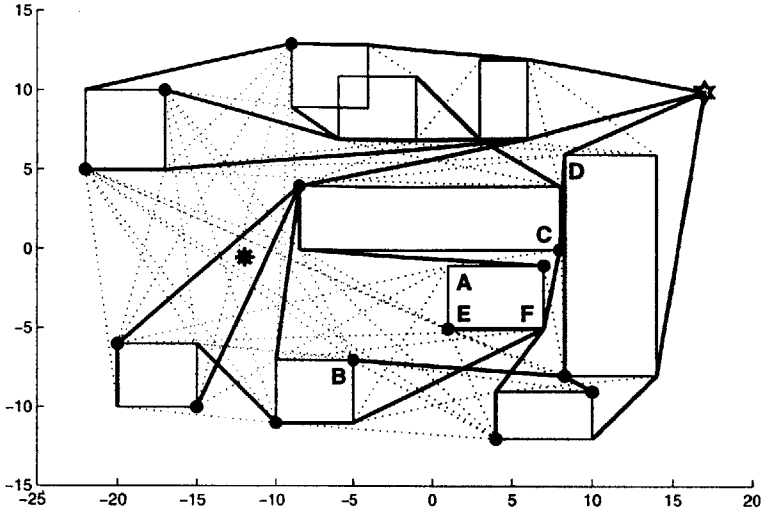

Figure 3-15: Points visible from the initial position

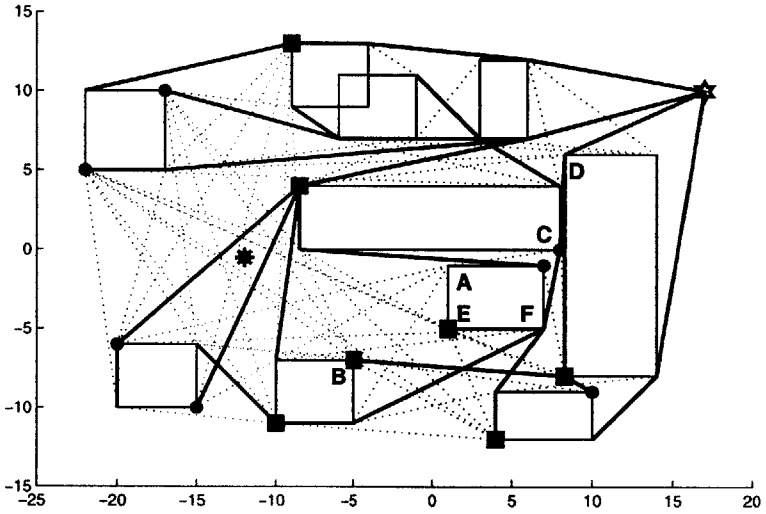

Figure 3-16: Points visible and connectable from the initial position

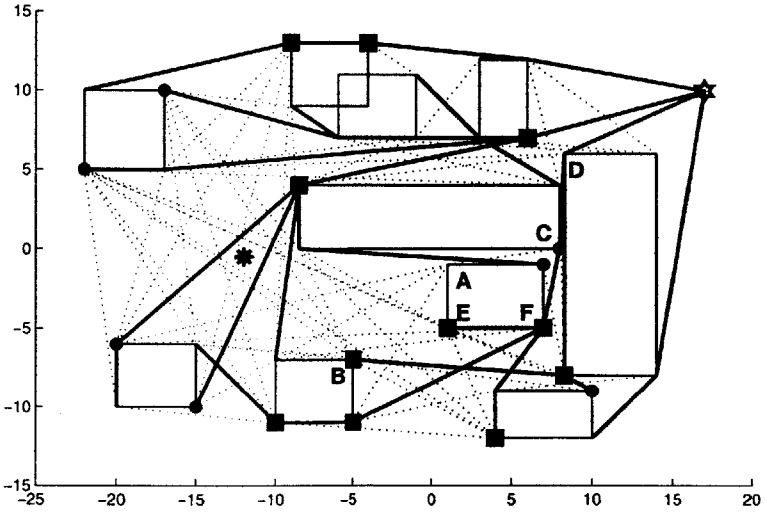

Figure 3-17: Cost points used in MILP

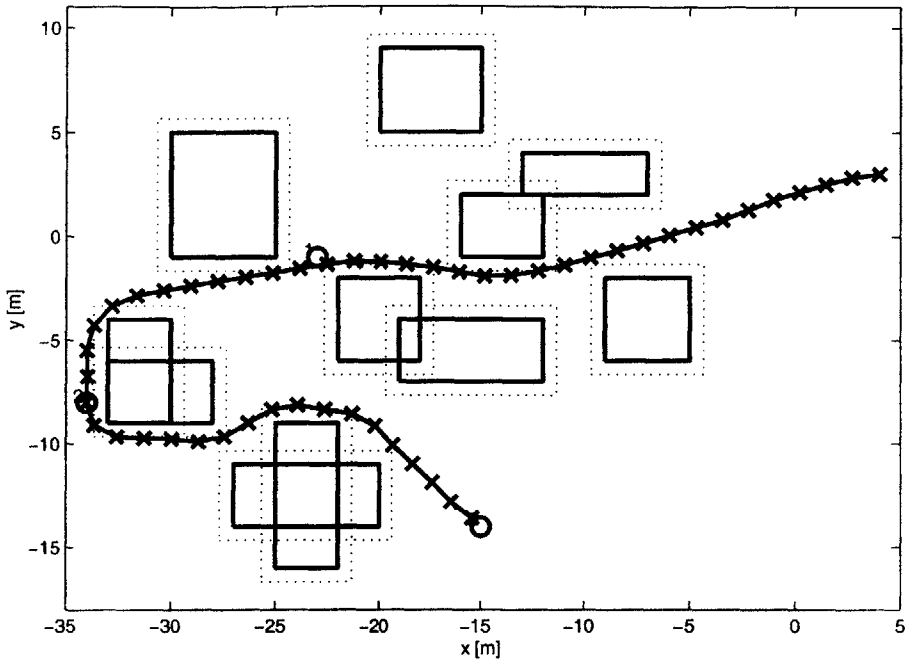

Figure 3-18: Trajectory in the highly constrained environment

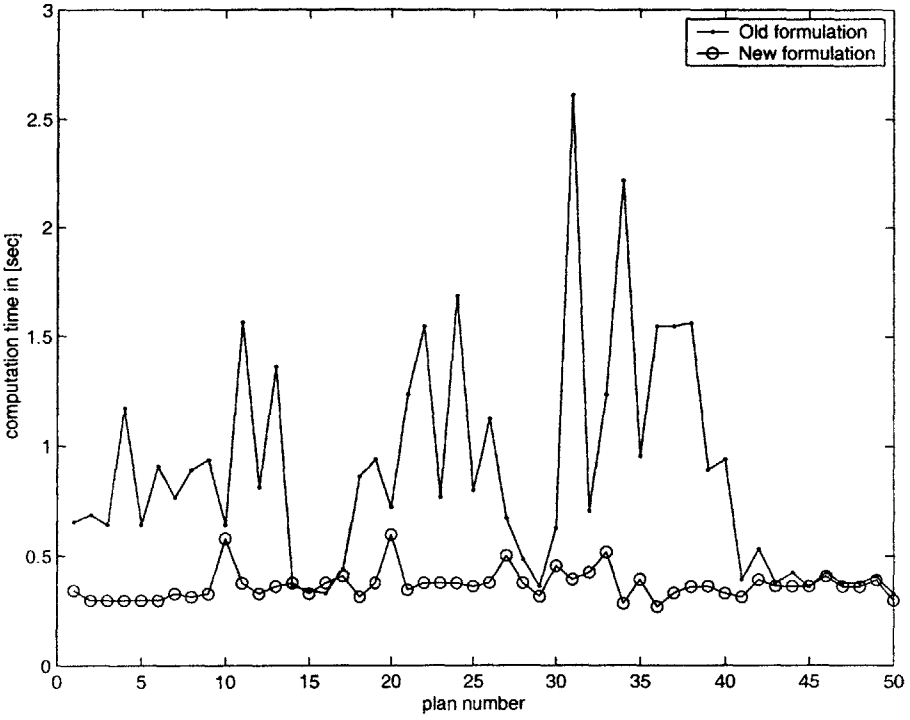

Figure 3-19: Comparison of the computation times.

new (stable) formulations, and Figure 3-19 compares the computation times of the two approaches. The plan reaches the final goal on the 50^{th} steps. The line with $\cdot$ and the one with $\circ$ show the computation time of the old and stable formulations, respectively. As shown, there is a significant improvement in the computation time. Without pruning, there are 47 candidate nodes. If a node lies behind an obstacle, the visibility test Eqs. 2.31 to 2.38 rejects the node. This process involves a number of binary variables, and becomes computationally demanding as the number of obstacles increases. The stable formulation prunes most of these nodes before performing the MILP optimization, which results in a drastic reduction in the computation time. Note that this formulation only prunes the nodes that **will never be selected**, and still retains the freedom to choose the best path from the trees of nodes that remain.

3.5 Stability Proof

The procedures discussed in the previous sections create a coarse cost map that guarantees the existence of a kinodynamically feasible path to the goal. This section addresses the optimization process using a receding horizon controller that designs detailed trajectories. In order to guarantee stability, several parameters of the receding horizon controller must satisfy the conditions, identified in Subsection 3.5.1.

3.5.1 Stability Criteria

The receding horizon controller has two horizons: the detailed trajectory, which is kinodynamically feasible, is designed over n_p steps of planning horizon; but only the portion in the execution horizon, which is the first n_e steps of the generated plan, is executed, and the receding horizon controller re-optimizes the trajectory beyond the execution horizon. However, since the straight lines used to approximate the cost beyond the planning horizon can be dynamically infeasible, this optimization process can fail. This situation is successfully avoided by having a planning horizon that is relatively long compared to the execution hori-

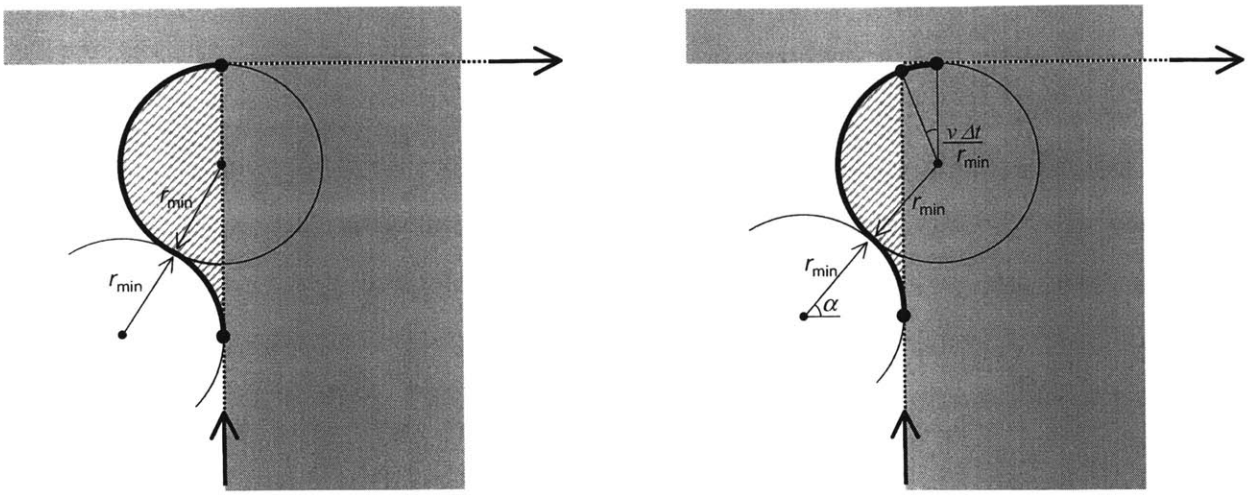

(a) Continuous time

(b) Discrete time step

Figure 3-20: Minimum margin to keep execution horizon in a feasible region

zon. The margin $(n_p - n_e)$ ensures the state on the execution horizon, which is the initial state of the next optimization problem, stays in the region from which a feasible path to the goal exists.

The length of the planning horizon n_p should be kept as small as possible since the complexity of MILP grows rapidly as the number of steps in the plan increases. The margin $(n_p - n_e)$ has a lower bound in order to guarantee stability, but it should be minimized in order to keep n_p small. The length of the execution horizon also has a lower bound, which is derived from the computation time: the next plan must be generated before the vehicle finishes executing the current plan.

The minimum margin must be able to account for the discrepancy between the straight line approximation and the dynamically feasible path. The largest discrepancy occurs when the intersection of two line segments forms a 90° angle at the obstacle corner. Figure 3-20(a) graphically shows the length of the minimum margin required to ensure that the state on the execution horizon never becomes infeasible if taken as an initial condition of the next plan. The vehicle enters from the bottom of the figure along the obstacle boundary and is aiming towards the right of the figure by going through the narrow passage. Once the vehicle passes

Table 3.2: Minimum number of steps required as a margin.

margin	$\frac{r_{\min}}{v\Delta t}$ (discrete)	degrees per step	$\frac{r_{\min}}{v\Delta t}$ (continuous)	degrees per step
3	1.2	49	0.8	70
4	1.4	40	1.1	53
5	1.7	34	1.4	42
6	2.0	29	1.6	35
7	2.3	26	1.9	30
8	2.5	23	2.2	26
10	3.1	19	2.7	21

through the thick line and enters the shaded portion, which is formed by two circles of radius $r_{\min}$, it cannot avoid a collision. The minimum margin $n_{m_{\min}}$ is geometrically calculated as the length of the thick line divided by the step size:

$$n_{m_{\min}} \geq \frac{7\pi r_{\min}}{6v\Delta t} \tag{3.13}$$

In a discrete time model, the vehicle can cut corners[6], and thus the constraint on the minimum margin is actually looser than Eq. 3.13. Figure 3-20(b) shows the worst case for the discrete time model. Again, the shaded area represents the infeasible region. In this case, the thick line has the length

$$\overline{L} = \frac{\pi r_{\min}}{2} + 2\alpha r_{\min} \tag{3.14}$$

where

$$\cos\alpha = \frac{r_{\min} + r_{\min}\sin\left(\frac{v\Delta t}{r_{\min}}\right)}{2r_{\min}} \tag{3.15}$$

and so

$$n_{m_{\min}} \geq \frac{r_{\min}}{v\Delta t}\left\{\frac{\pi}{2} + 2\arccos\left(\frac{1+\sin\left(\frac{v\Delta t}{r_{\min}}\right)}{2}\right)\right\} \tag{3.16}$$

The minimum margin obtained from Eq. 3.13 and 3.16, as a function of the ratio of minimum turning radius $r_{\min}$ and step size $v\Delta t$, is summarized in Table 3.2. The first column

[6]See Figure 2-4 on p.32

shows the minimum number of steps required as a margin given the ratio $r_{\min}/(v\Delta t)$. If the ratio is in between the two numbers, the larger value must be used to ensure stability when selecting the minimum margin from this table. With the same step size $v\Delta\, t$, a larger minimum turning radius requires a larger margin[7] since the vehicle is less agile. With the same minimum turning radius, a smaller $v\Delta t$ requires a larger margin since the waypoints on the trajectory are more detailed.

The third and fifth columns give the central angle per step for a given $r_{\min}/(v\Delta t)$ when turning along the circle with a minimum turning radius. As the angle per step decreases, *i.e.*, the vehicle follows the turning circle with more detailed waypoints, a larger number of steps is required as a margin. Note that a larger margin causes longer computation time; this represents a trade-off between the computation load and the resolution of the trajectory.

Simulation Result

The simulation result in Figure 3-21 demonstrates the stability of the receding horizon controller. Original obstacles are depicted by solid lines, while dashed lines show obstacle boundaries expanded to account for the discrete time model[8]. Solid lines with bullets show the detailed trajectory, and dotted lines with bullets show the waypoints of the previous plan. The vehicle starts at the bottom of the figure and goes to the upper right by passing through the narrow passage. From (a) to (f), the vehicle executes one step at a time. A circle introduced in Figure 3-20(b) is placed to show the infeasible region. The following parameters are used in this simulation.

- $n_p = 11$
- $n_e = 1$
- $r_{\min} = 3.1$
- $v\Delta t = 1$

[7] "Large" in the sense that the number of steps is large.
[8] See Figure 2-4 for obstacle enlargement.

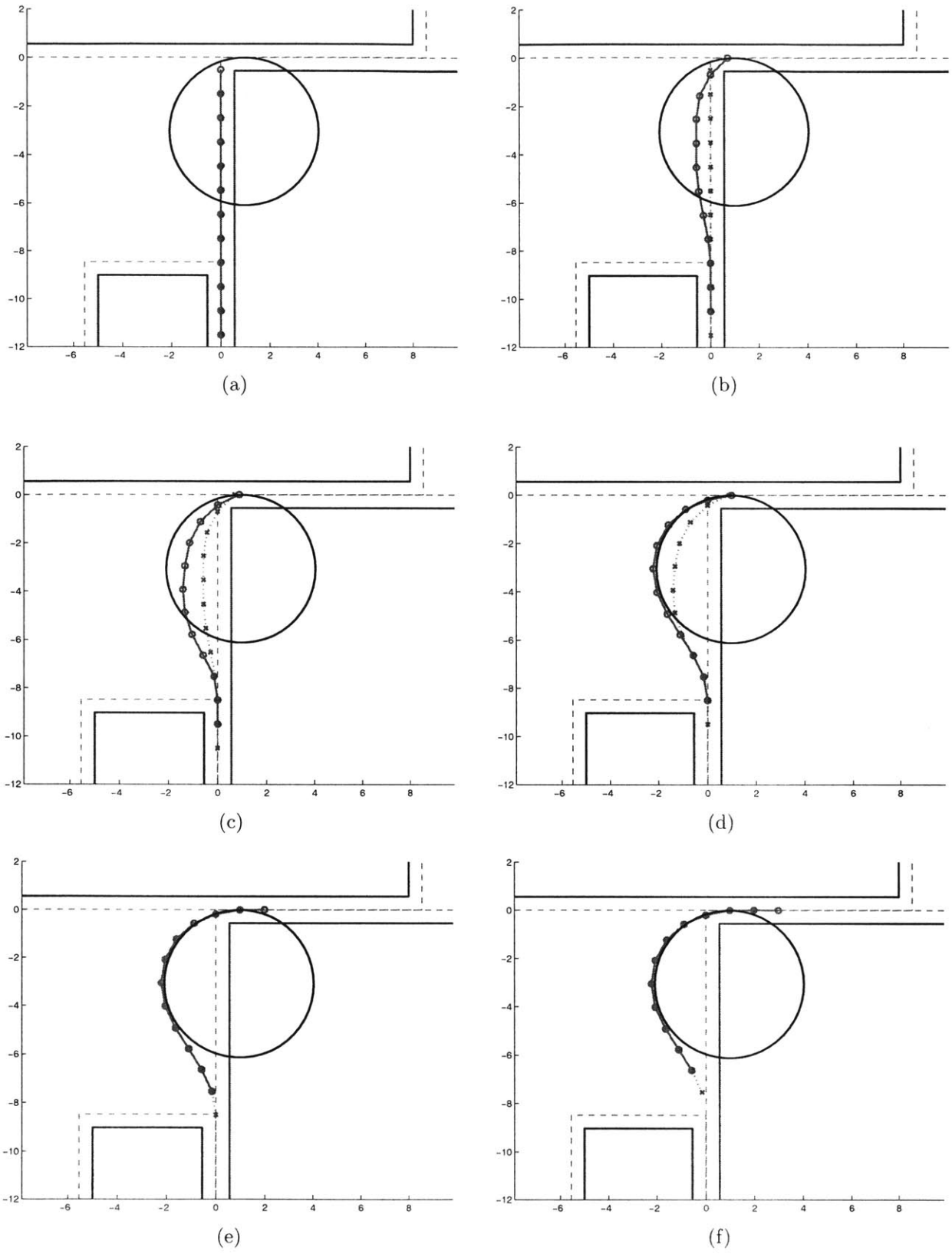

Figure 3-21: Worst case turn. The straight line approximation requires a 90 degree turn at the corner.

In Figure 3-21(a), the planning horizon approaches the corner. After executing one step, the planning horizon of the next plan enters the narrow passage, as shown in (b). However, it cannot proceed until the heading direction of the terminal step is aligned to the narrow passage as in (d). The resultant trajectory follows the circle of radius $r_{\min}$ as expected in Figure 3-20(b). This result shows that with the minimum margin obtained from Table 3.2 the vehicle always stays in a region from which a feasible path to the goal is guaranteed to exist. Note that this scenario goes infeasible with the old formulation, or with too short a margin. The estimate of the minimum margin is still conservative. Future work will be required to reduce the margin.

3.5.2 Finite Time Completion

Finite Time Completion

The modified Dijkstra's algorithm in Section 3.3 ensures the existence of a kinodynamically feasible path around the line segments from each cost point to the goal. As shown in the previous section, when turning a corner, the vehicle will deviate from the straight line path. In order to obtain a feasible path, however, the vehicle is required to satisfy a condition that the vehicle joins the next straight line before the comeback point. The minimum margin $n_{m_{\min}}$, as discussed in the previous subsection, enables the MILP RHC to find the optimal trajectory while satisfying this condition. This argument proves that the receding horizon optimization problems are always feasible until the vehicle reaches the goal.

Although the UAV moves at a constant speed v, the point on the planning horizon can move less than $v\Delta t$, as shown in Figures 3-21(b) to (d), when a planned trajectory does not follow the previous plan. This is caused by a discrepancy between the straight line approximation and the vehicle dynamics beyond the planning horizon. Once the heading discontinuities are resolved, however, the point on the planning horizon starts moving towards the goal again (Figures (d) to (e)).

The proof of a finite time completion is obtained from the following arguments. First, the sum of the straight line lengths from the start point to the goal is calculated as the total

path length. Then, all of the differences ΔJ between the arc lengths and the straight line lengths, as expressed in Eq. 3.7, are added to the total path length. This path length from the initial point to the goal along a feasible path gives an upper bound $J_{\max}$ of the length of the optimal trajectory. Since the vehicle moves at a constant speed v, it will enter a circle of radius $v\Delta t$ around the goal in at most $k_{\max}$ steps, where

$$k_{\max} = \text{floor}\left(\frac{J_{\max}}{v\Delta t}\right) \tag{3.17}$$

Simulation Result

Figure 3-22 shows an optimal trajectory for a scenario where two tight turns are required and Figure 3-23 shows the cost-to-go of each plan and the pre-calculated upper bound. Note that the difference between the two plots for the first plan is the sum of the difference ΔJ at each corner. The difference in the distance between the straight lines and the arcs is obtained from Eq. 3.7.

If the generated plan is the same as a straight line, then the cost-to-go decreases by $v\Delta t$ at each time step. When the planning horizon comes to the obstacle boundary $y = 0$, large discontinuities appear between the heading direction at the terminal point and the direction of the straight line approximation, and the horizon point cannot proceed until these two directions are aligned. Thus, the decrease in the cost-to-go during plan numbers 6–8 in Figure 3-23 is quite small. When the vehicle makes another turn in plans 16–18, the decrease in cost-to-go is also less than $v\Delta t$. However, the cost-to-go is bounded by the straight line $J(k) = J_{\max} - k(v\Delta t)$, which constantly decreases by $v\Delta t$ for each step and would eventually be less than zero. Having $J(k) < 0$ is a contradiction, so the cost-to-go must be less than $v\Delta t$ before the upper bound hits zero. This implies that the vehicle will enter inside a circle of radius $v\Delta t$ around the goal in finite time [15].

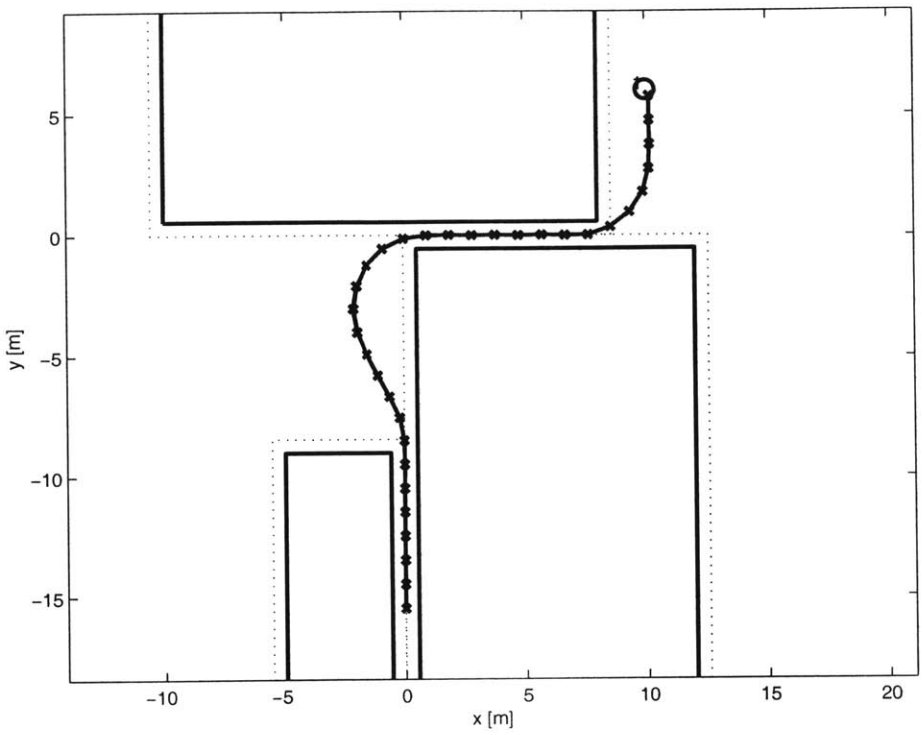

Figure 3-22: Trajectory

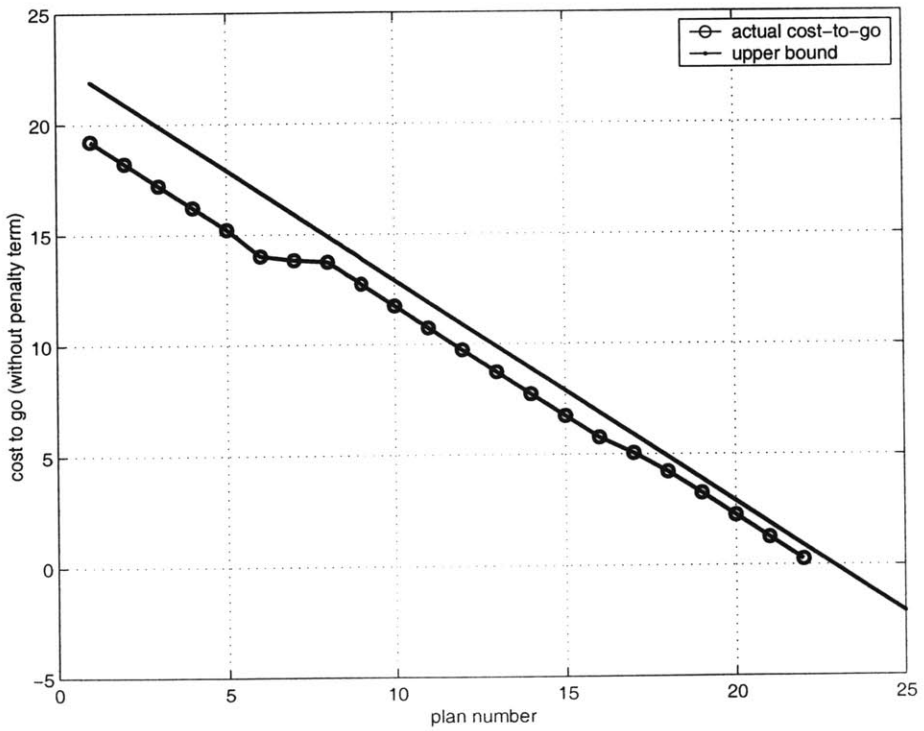

Figure 3-23: Decrease of cost-to-go

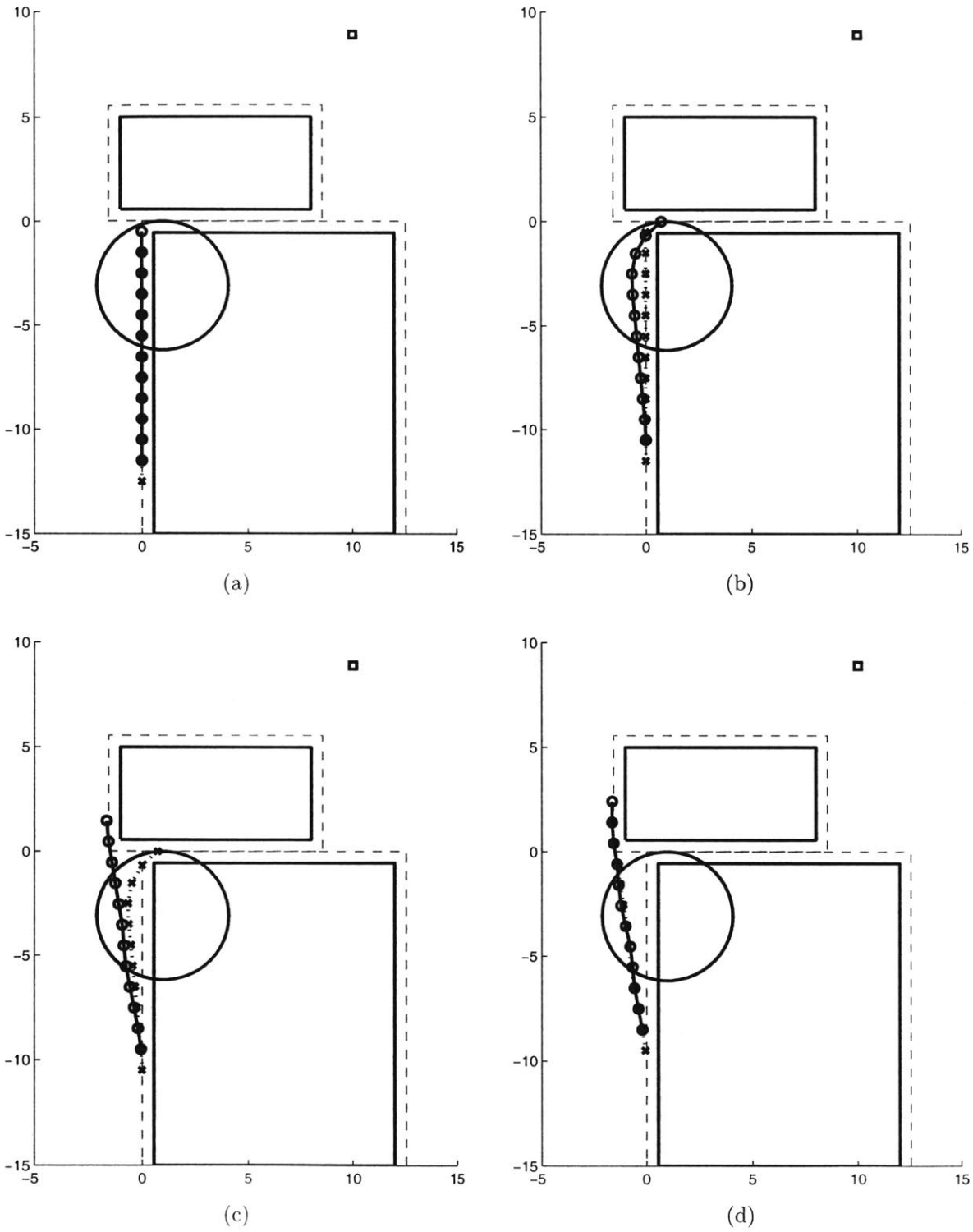

Figure 3-24: Selection of another path

Selection of Better Path

Once there is a large discrepancy between a straight line approximation and a dynamically feasible path, the decrease of cost-to-go gets smaller than the nominal $v\Delta t$ per step, although the cost-to-go along the actual trajectory is still bounded by a pre-calculable quantity as stated above. In such situations, the stable receding horizon controller can choose another path. Note that this formulation allows the controller to select only feasible paths, as shown in Figure 3-17.

Figure 3-24 shows an example where the vehicle changes its decision about the obstacle avoidance maneuver on its way to the goal. The vehicle is at the lower left, and the goal is marked with a small rectangle shown in the upper right of the figures. Originally, the vehicle chooses to pass through the narrow passage based on a cost estimate using straight lines (Fig. (a)). In Fig. (b), going around the corner prevents the planning horizon from proceeding and does not reduce the cost-to-go along the path. Then the controller makes a different decision, as shown in Fig. (c), on the selection of the visible point, and as a result the vehicle goes around the upper obstacle. Note that the controller selected another path simply because the cost-to-go along the new path is smaller than the first, and the cost-to-go of the actual vehicle trajectory is still bounded by the same straight line $J(k) = J_{\max} - k(v\Delta t)$.

3.6 Conclusions

This chapter presented a new algorithm that stably navigates the vehicle to the goal. The vehicle dynamics are taken into account as a minimum turning radius in the cost estimation phase. By placing turning circles around the obstacle corners, the modified Dijkstra's algorithm finds node sequences along which a feasible path to the goal exists. The pruning algorithm eliminates unnecessary nodes to form a stable cost map, without losing the freedom to choose better paths. This process was demonstrated to significantly reduce the computation time. It was also shown that the receding horizon controller must extend the planning horizon beyond the execution horizon in order to guarantee the stability of the tra-

jectory optimization. The lower bound of the margin required was analytically calculated. Combined with the stable cost map, this formulation proved that: 1) the RHC always has a feasible solution, and 2) the vehicle reaches the goal in finite time. The simulations verified these results.

Chapter 4

Task allocation for Multiple UAVs with Timing Constraints and Loitering

This chapter describes methods for optimizing the task allocation problem for a fleet of *unmanned aerial vehicles* (UAVs) with tightly coupled tasks and rigid relative timing constraints. The overall objective is to minimize the mission completion time for the fleet, and the task assignment must account for differing UAV capabilities and obstacles (no-fly zones). *Loitering times* are included as extra degrees of freedom in the problem to help meet the timing constraints. The overall problem is formulated using *mixed-integer linear programming*(MILP). Commercial software exists to obtain the globally optimal solution to these problems. However, an approximate decomposition solution method is used to overcome many computational issues for reasonable sized problems.

4.1 Problem Formulation

This section describes how the multiple vehicle routing problems with relative timing constraints and loitering can be written as a MILP. The algorithms assume that the team par-

titioning has already been performed, and that a set of tasks has been identified that must be performed by the team. The next step is to assign specific tasks to the team members and design a detailed trajectory for each member to achieve these tasks.

4.1.1 Problem Statement

Let there be a team of N_V UAVs with known starting states and maximum velocities, N_W waypoints[1], and N_Z no-fly zone. The starting state of the i^{th} UAV is given by the i^{th} row $[\ x_{0i} \quad y_{0i} \quad \dot{x}_{0i} \quad \dot{y}_{0i}\ ]$ of the $N_V \times 4$ matrix $\mathbf{S_0}$, and the maximum velocity of UAV i is given by $v_{\max,i}$. The locations of the N_W waypoints are assumed to be known, and the (x, y) position of waypoint i is given by the i^{th} row $[\ W_{i1} \quad W_{i2}\ ]$ of the matrix $\mathbf{W}$. The (x, y) location of the lower-left corner of the j^{th} obstacle is given by (Z_{j1}, Z_{j2}), and the upper-right corner by (Z_{j3}, Z_{j4}). Together, these two pairs make up the j^{th} row of the $N_Z \times 4$ matrix $\mathbf{Z}$.

The UAV capabilities are represented by the $N_V \times N_W$ binary capability matrix $\mathbf{K}$. The entry K_{ij} is 1 if UAV i is capable of performing the tasks associated with waypoint j, and 0 if not. Finally, N_C timing constraints are in matrix $\mathbf{C}$ and vector $\mathbf{d}$, in which each row represents a dependency between two waypoints. A row k in $\mathbf{C}$ with $[\ i \quad j\ ]$ and corresponding element d_k implies a timing constraint that waypoint j must be visited at least d_k time units after waypoint i.

The algorithm produces a trajectory for each UAV, represented for the i^{th} UAV by a series of states $\mathbf{s}_{ti} = [\ x_{ti} \quad y_{ti} \quad \dot{x}_{ti} \quad \dot{y}_{ti}\ ]$, $t \in [1, t_{F_i}]$, where t_{F_i} is the time at which UAV i reaches its final waypoint. The finishing times of all UAVs make up the vector $\mathbf{t_F}$.

4.1.2 Algorithm Overview

There are three main phases in our algorithm [3, 4]: (I) cost calculation, (II) planning and pruning, and (III) task assignment.

[1]In this chapter, "waypoint" refers to target or site to be visited whereas in the other chapters it refers to trajectory points generated by RHC.

I-1. Find the visibility graph between the UAV starting positions, waypoints, and obstacle vertices.

I-2. Using the Dijkstra's algorithm, calculate the shortest length of the all feasible paths between waypoints, and form the cost table. The straight line length divided by maximum velocity is used as an approximate cost.

II-1. Obtain feasible `combinations` of waypoints, accounting for the capability matrix $\mathbf{K}$ and the maximum number of waypoints per UAV.

II-2. Enumerate all feasible `permutations` from these combinations, subject to the timing constraints.

II-3. Calculate cost for each permutation using the cost table obtained in phase I.

II-4. Select the n_p best permutations for each combination. Typically, setting $n_p = 1$ will yield the optimal solution to the assignment problem.

III-1. Solve the task allocation problem using an optimization solver.

III-2. Solve for the each UAV's trajectory (*e.g.* using straight line segments).

At the end of the phase II, four matrices are produced whose j^{th} columns, taken together, fully describe one permutation of waypoints. These are the row vector $\mathbf{u}$, whose u_j entry identifies which UAV is involved in the j^{th} permutation; $N_W \times N_M$ matrix $\mathbf{V}$, whose V_{ij} entry is 1 if waypoint i is visited by permutation j, and 0 if not; $N_W \times N_M$ matrix $\mathbf{T}$, whose T_{ij} entry is the time at which waypoint i is visited by permutation j assuming there is no loitering, and 0 if waypoint i is not visited; and the row vector $\mathbf{c}$, whose c_j entry is the completion time for the j^{th} permutation, again, assuming there is no loitering. All of the permutations produced by this algorithm are guaranteed to be feasible given the associated UAV's capabilities.

4.1.3 Decision Variables

The overall objective is to assign one set of ordered waypoints to each vehicle that is combined into the mission plan, and adjust the loiter times for the team such that the cost of the mission is minimized and the time of task execution at each waypoint satisfies the timing constraints.

Selection of the Permutations:

In order to assign one permutation to one vehicle, the $N_M \times 1$ binary decision vector $\mathbf{x}$ is introduced whose x_j equals one if permutation j is selected, and 0 otherwise. Each waypoint must be visited once, and each vehicle must be assigned to one permutation, so

$$\sum_{j=1}^{N_M} V_{ij} x_j = 1, \qquad i = 1, \ldots, N_W \tag{4.1}$$

$$\sum_{j=N_p}^{N_{p+1}-1} x_j = 1, \qquad p = 1, \ldots, N_V \tag{4.2}$$

where the permutations of p^{th} vehicle are numbered N_p to $N_{p+1} - 1$, with $N_1 = 1$ and $N_{N_V+1} = N_M + 1$.

Loitering time:

We introduce the $N_W \times N_V$ loitering matrix $\mathbf{L}$, whose L_{ij} element expresses the loiter time at the i^{th} waypoint when visited by UAV j, as a set of new decision variables. $L_{ij} = 0$ if waypoint i is not visited by UAV j. This loitering matrix ensures that it is always possible to find a feasible solution as long as the timing constraints are consistent. In the MILP formulation, the time of the task execution at waypoint i, TOE_i, is written as

$$TOE_i = \sum_{j=1}^{N_M} T_{ij}\, x_j + LB_i, \qquad i = 1, \ldots, N_W \tag{4.3}$$

where the first term expresses the flight time from the start point to waypoint i at $v_{\max}$, and LB_i is the sum of the loiter times before executing the task at waypoint i.

As shown in Fig. 4-1, the loiter time at waypoint i is defined as the time difference between time of the task execution and the time of arrival at waypoint i. The UAVs are assumed to fly at the maximum speed between waypoints, and loiter before executing the task. Note that this formulation only allows loitering at waypoints, but it can also be regarded as flying at a slower speed between the waypoints, or loitering at the previous waypoint, flying towards

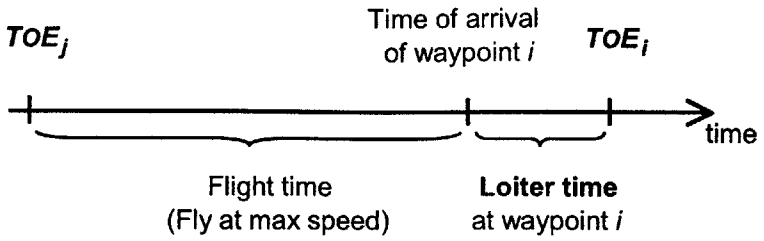

Figure 4-1: Flight time, loiter time, time of arrival, and time of task execution

the waypoint at the maximum speed, and executing the task. By changing the loiter time we can adjust the time of the tasks, and exactly how the loitering is executed is mission specific. There is no loitering at the starting positions of the UAVs since it is included in the loiter times of their first waypoints.

Define the sets $\mathcal{W}$ such that $\mathcal{W}_i$ is the list of waypoints visited on the way to waypoint i including i, so LB_i is calculated as

$$LB_i = \sum_{j \in \mathcal{W}_i} \sum_{k=1}^{N_V} L_{jk}\,, \qquad i = 1, \ldots, N_W \tag{4.4}$$

where $\sum_{k=1}^{N_V} L_{jk}$ expresses the loiter time at the j^{th} waypoint. Only one UAV is assigned to each waypoint, and each row of $\mathbf{L}$ has only one non-zero element. Note that LB_i depends on which UAV visits waypoint i, which is determined by the decision vector $\mathbf{x}$. For a set of permutations chosen for the UAVs, the loiter time $\mathbf{L}$ is determined to meet all the timing constraints, so the values L_{jk} also depend on $\mathbf{x}$.

To express the logical statement "on the way to", we introduce a large number M, and convert the one equality constraint Eq. 4.4 into two inequality constraints

$$LB_i \leq \sum_{j=1}^{N_W} \left(O_{ijp} \sum_{k=1}^{N_V} L_{jk} \right) + M \left(1 - \sum_{p=1}^{N_M} V_{ip} x_p \right) \tag{4.5}$$

and

$$LB_i \geq \sum_{j=1}^{N_W} \left(O_{ijp} \sum_{k=1}^{N_V} L_{jk} \right) - M \left(1 - \sum_{p=1}^{N_M} V_{ip} x_p \right) \tag{4.6}$$

where $\mathbf{O}$ is a three dimensional binary matrix that expresses waypoint orderings, and its O_{ijp} entry is 1 if waypoint j is visited before waypoint i (including $i = j$) by permutation p, and 0 if not. When waypoint i is visited by permutation p, the second term on the right-hand side of the constraints in Eq. 4.5 and 4.6 disappear since $\sum_{p=1}^{N_M} V_{ip} x_p = 1$. In that case, Eq. 4.5 and 4.6 can be combined to form the equality constraint

$$LB_i = \sum_{j=1}^{N_W} \left(O_{ijp} \sum_{k=1}^{N_V} L_{jk} \right) \tag{4.7}$$

which is the same as Eq. 4.4. Note that when waypoint i is not visited by permutation p, $O_{ijp} = 0$ for all j and $V_{ip} = 0$, so that both of the inequality constraints are relaxed and LB_i is not constrained.

4.1.4 Timing Constraints

The timing constraints of interest in this application are relative, as opposed to the absolute ones often considered [28, 29, 30, 31, 32]. The constraints can be written as

$$TOE_{C_{k2}} \geq TOE_{C_{k1}} + d_k\,, \qquad k = 1, \ldots, N_C \tag{4.8}$$

yielding a very general formulation. Recall matrix $\mathbf{C}$ contains indices of waypoints involved in each timing constraint k. If the k^{th} row of $\mathbf{C}$ is $[\ i \quad j\ ]$, Eq. 4.8 becomes $TOE_j \geq TOE_i + d_k$. Note that d_k can also be negative. This formulation allows us to describe all kinds of timing constraints. For example, although each waypoint i has only one time of execution TOE_i associated with it, this formulation can be used to describe several visits with timing constraints by putting multiple waypoints at that location.

4.1.5 Cost Function

The cost J to be minimized in the optimization problem is

$$J = \left(\max_{i \in \{1,\ldots,N_V\}} t_{F_i} \right) + \frac{\alpha}{N_V} \sum_{i=1}^{N_M} c_i x_i + \frac{\beta}{N_W} \sum_{j=1}^{N_V} \sum_{i=1}^{N_W} L_{ij} \tag{4.9}$$

where the first term expresses the maximum completion time amongst the UAV team, the second term gives the average completion time, and the third term gives the total loiter times. α weights the average flight time compared to the maximum completion time. If the penalty on average flight time were omitted, the solution could assign unnecessarily long trajectories to all UAVs except for the last to complete its mission. Similarly, $\beta \geq 0$ can be used to include an extra penalty that avoids excessive loitering times.

4.2 Simulation Results

This section presents several simulation results using the formulation in Section 2. The problems were solved using CPLEX (v7.0) software running on a 2.2GHz PC with 512MB RAM. The first result investigates how the timing constraints change the solution times. The second example considers the relationship between the complexity of timing constraints and the computation time.

4.2.1 Problem With and Without Timing Constraints

A large scenario that includes a fleet of 6 UAVs of 3 different types and 12 waypoints is used as our baseline. The UAV capabilities are shown in Figure 4-2 (top left). There are also several obstacles in the environment. The objective is to allocate waypoints to the team of UAVs in order to visit every waypoint once and only once in the minimum amount of time. For convenience, this problem without timing constraints will be referred to as the "original" problem. Figure 4-2 shows the solution of this original problem. All waypoints are visited subject to the vehicle capabilities in 23.91 time units. Time of task execution of

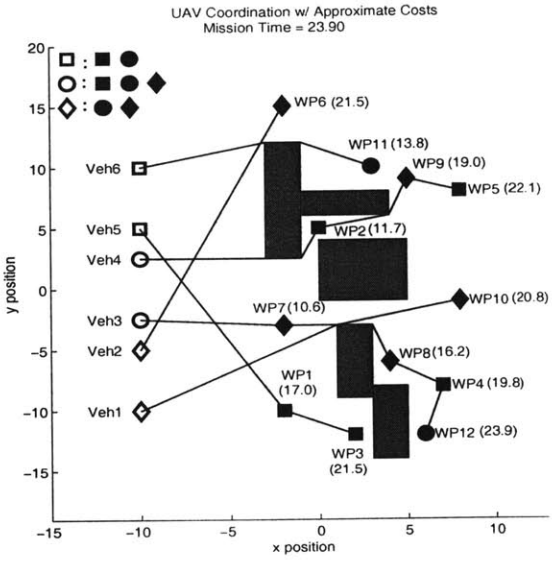

Figure 4-2: Scenario with 6 heterogenous UAVs & 12 waypoints. No timing constraints. Solved in 2sec.

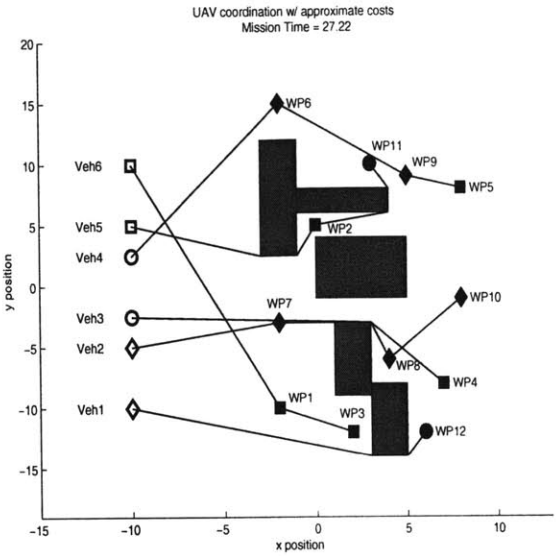

Figure 4-3: Same as Fig. 4-2, plus 7 timing constraints. Solved in 9sec.

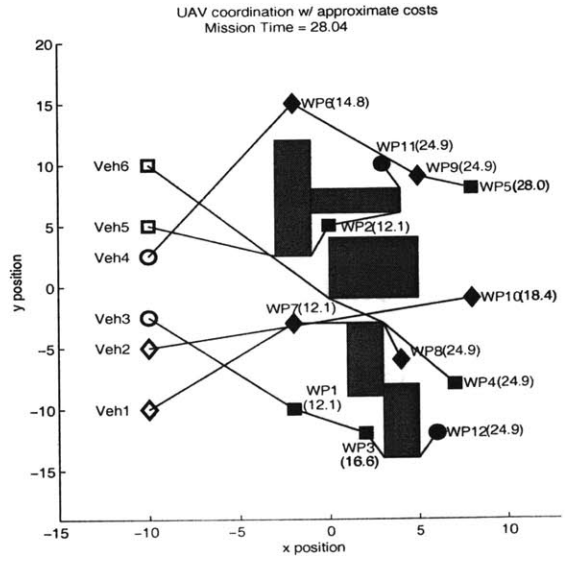

Figure 4-4: Same as Fig. 4-2, plus 11 timing constraints. Solved in 13sec.

each waypoint is also shown beside the waypoint in the figure.

The problem with simultaneous arrival and ordered task was also considered. Timing constraints in this scenario are as follows:

1. Waypoints 4, 8, 12 must be visited at the same time.
2. Waypoints 9, 11 must be visited at the same time.
3. Waypoints 4, 8, 12 must be visited before waypoints 9, 11.

The first two represent examples of scenarios that require the UAVs to simultaneously strike in force, and the third corresponds to a scenario that requires a SAM site be eliminated before a strike force is sent to a high value target.

The solution in this case is shown in Figure 4-3. In Figure 4-2, UAV3 visits waypoints 4, 8, and 12, whereas in Figure 4-3, three UAVs are assigned to these three waypoints since they must all be visited at the same time. Furthermore, in Figure 4-2, three UAVs (1, 3, and 5) are assigned to the waypoints in the lower half of the figure. However, in Figure 4-3, four UAVs are assigned to these points since the priority of waypoints 4, 8, 12 are higher than that of waypoints 9, 11 as a result of the timing constraints. The mission time for this scenario increased to 27.22 time units, and the computation time increased from 2 seconds to 9 seconds. To solve this problem in a reasonable time, the following approximations were made:

- Select only 1 best feasible permutation per combination. This avoids the combinatorial explosion, typically with a small degradation in performance.
- If there is a timing constraint $TOE_i \geq TOE_j + t_D$ $(t_D \geq 0)$, then the UAVs can loiter only at waypoint i, since we want to minimize the completion time of entire fleet.

In the solution in Figure 4-3, 3 UAVs (1, 2, 5) loiter before reaching waypoint 12, 8, 11 respectively. Thus this scenario could have been solved by adjusting only the starting times of the UAVs, as in Ref. [3].

A harder scenario was also investigated with the following timing constraint added to the previous case: Waypoints 1, 7, 2 must be visited at the same time. This represents a scenario where simultaneous attacks are required. The results are shown in Figure 4-4 which is quite

Table 4.1: Results with no constraints on loitering time.

Case	1	2	3	4
Avg. computation time (s)	3.3	20.6	4.6	23.9
% of prob. solved in 5 sec	97.0	27.3	80.0	13.9

Table 4.2: Result with constrained loitering times.

Case	1	2	3	4
Avg. computation time (s)	2.2	8.5	3.0	11.6
% of prob. solved in 5 sec	100.0	48.4	93.0	30.3

different from Figure 4-3 (*e.g.* Waypoint 4 is visited by UAV6, which is the farthest from it). In order to satisfy the many timing constraints, 4 UAVs loiter at 6 waypoints. UAV1 loiters on its way to waypoint 7 and 8, and UAV3 loiters on its way to waypoints 1 and 12. If time adjustment is allowed only on the initial position, a feasible solution cannot be found in this scenario. Since the loiter matrix **L** allows UAVs to loiter at any of the waypoints with timing constraints, problems with strongly coupled timing constraints are always solvable.

4.2.2 Complexity of Adding Timing Constraints

To investigate the impact of the timing constraints on the performance and computation time, we measured the computation time for the same problem in Section 4.2.1, with the following 4 different cases of timing constraints:

Case – 1: $TOE_i \geq TOE_j$

Case – 2: $TOE_i \geq TOE_j + 10$

Case – 3: $TOE_i \geq TOE_j \geq TOE_k$

Case – 4: $TOE_i \geq TOE_j + 5 \geq TOE_k + 10$

In each case, all feasible combinations of waypoints $(i,\ j)$ or $(i,\ j,\ k)$ were tested as the points associated with the timing constraints. The results are summarized in the histograms of Figures 4-5–4-8 and Tables 4.1 and 4.2.

Figures 4-5(a), 4-6(a), 4-7(a), and 4-8(a) show the results when all loitering times are included in the problem. Since there are 12 waypoints and 6 UAVs with different capabiilties,

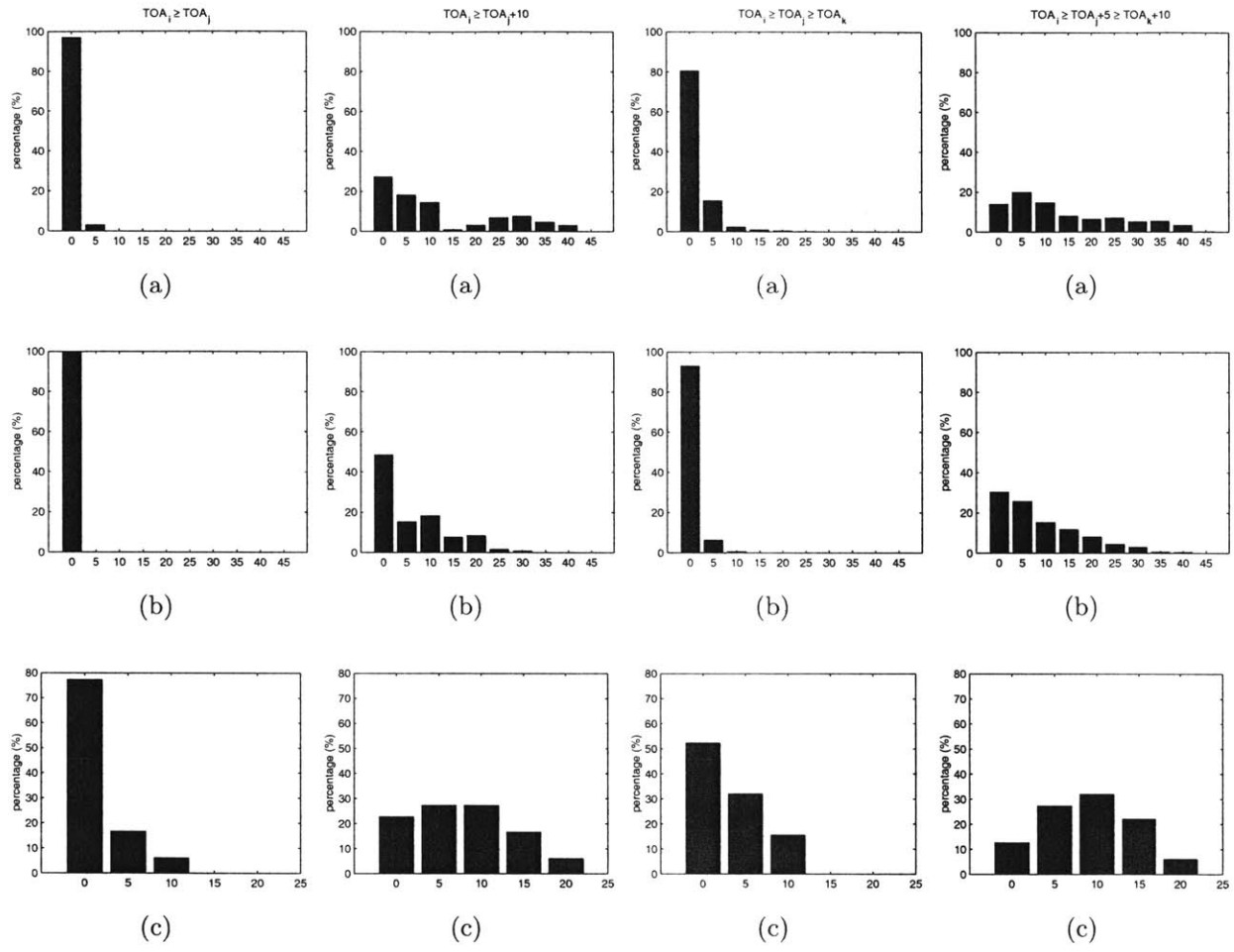

Fig. 4-5: Case –1 **Fig. 4-6**: Case –2 **Fig. 4-7**: Case –3 **Fig. 4-8**: Case –4

Figure (a) shows the computation time (sec) for the problem with no constraints on the loitering times; figure (b) shows the computation time (sec) for the problem with constrained loitering; and figure (c) shows the degree of "Unnaturalness" for the problem.

there are 52 extra degrees of freedom in the decision variable **L**. Figures 4-5(b), 4-6(b), 4-7(b), and 4-8(b) show the results when the constrained form of the loitering is used. This reduces the degrees of freedom in the loiter matrix **L** from 52 to 8–12, depending on the type of constraints.

Comparing Figures 4-5(a), 4-5(b) with Figures 4-6(a), 4-6(b), and, Figures 4-7(a), 4-7(b) with Figures 4-8(a), 4-8(b), it is clear that the computation time increases as more complicated timing constraints are imposed on the tasks (either by increasing the time gaps or by increasing the number of related tasks). It is also clear that, with fewer degrees of freedom, the constrained loitering approach solves faster.

To measure the complexity of these constraints, we introduce the concept of the "unnaturalness" of the timing constraints, which is a measure of the degree to which the timing constraint are violated by the solution of the original problem. Using the solution of the original problem to obtain the times associated with waypoints i and j (TOE_i' and TOE_j'), the unnaturalness of a timing constraint $TOE_i \geq TOE_j + t_D$ is defined as

$$\max\{TOE_j' + t_D - TOE_i', 0\} \tag{4.10}$$

Thus, if the solution of the original problem happens to satisfy the timing constraint, the unnaturalness is 0. The sum of the unnaturalness of each timing constraint is used as a measure of the unnaturalness for the constrained problem. Note that many other metrics are possible, including the number of timing constraints, and the extent to which they are tightly coupled together. However, experience has shown that these metrics can be misleading if the results are "naturally" satisfied by the solution to the unconstrained problem. The metric in Eq. 4.10 gives a direct (albeit approximate) measure of the extent to which the solution must be changed to satisfy the additional timing constraints.

Figures 4-5(c), 4-6(c), 4-7(c), and 4-8(c) show four histograms that give the unnaturalness of the basic problem with timing constraints (cases 1 – 4). As is readily apparent, the shapes of the 4 histograms reflect the computation time required to solve these problem. In particular, as the distribution of the unnaturalness shifts towards right (Figure 4-5(c)→

4-6(c) and 4-7(c)→ 4-8(c)), the distribution of the computation time also shifts to the right (Figure 4-5(b)→ 4-6(b) and 4-7(b)→ 4-8(b)). Further observations include:

- If all of the timing constraints are natural, then the computation time does not increase significantly, even if there are many timing constraints.
- Infeasible permutations must be pruned before the cost calculation of each permutation, so that the best permutation for each combination is always feasible. If all the timing constraints are natural, the best permutation is always feasible without pruning by timing constraints, but that is not the case if there are unnatural timing constraints.
- Additional permutations can be kept to account for unnatural timing constraints, but simulation results have shown that this can rapidly increase the computational time with a marginal improvement in performance.

4.3 Conclusions

This chapter presented an extension of the multiple UAV task allocation problem that explicitly includes the relative timing constraints found in many mission scenarios. This not only allows us to determine which vehicle should go to each waypoint, but it also allows us to account for the required ordering and relative timing in the task assignment. The allocation problem was also extended to include loiter times as extra (continuous) degrees of freedom to ensure that, even with very complicated timing constraints, feasible solutions still exist. Simulation results clearly showed that adding these timing constraints to the problem increases the computational time when the constraints are active (*i.e.*, "unnatural").

This formulation becomes computationally intractable for reasonable sized problems. However, it is shown that an approximate decomposition solution method can be used to overcome many of these computational issues and solve problems with highly coupled tasks and timing constraints.

Chapter 5

Hardware Experiments

This chapter presents several results of hardware experiments with the receding horizon controller (RHC) discussed in the previous chapters. Section 5.1 describes the assumptions on which the experiments are based, and clarifies the difference between MATLAB simulations and the real world experiments. Section 5.2 shows the testbed setup and how the RHC interacts with the real world through the hardware. Two key features of RHC are demonstrated in Sections 5.3 to 5.5: replanning to account for uncertainty in the environment and real-time trajectory generation. In particular, Section 5.3 integrates the on-board low-level feedback controller and the RHC. Section 5.4 examines the replanning capability of the receding horizon trajectory generation. Section 5.5 considers a scenario with a large change in the situational awareness that requires on-line reassignment of tasks among the vehicles.

5.1 Experiments Overview

This section gives an overview of the experiments presented in this chapter. Figure 5-1 shows a hierarchical approach to the control and coordination of multiple vehicles. In the following experiments, the planner, which is shown as a box with dashed lines in the figure, interacts with the real environment. Four different levels of control loops are closed, one at a time, in Section 5.2 to Section 5.5, which are shown as grey boxes in the figure.

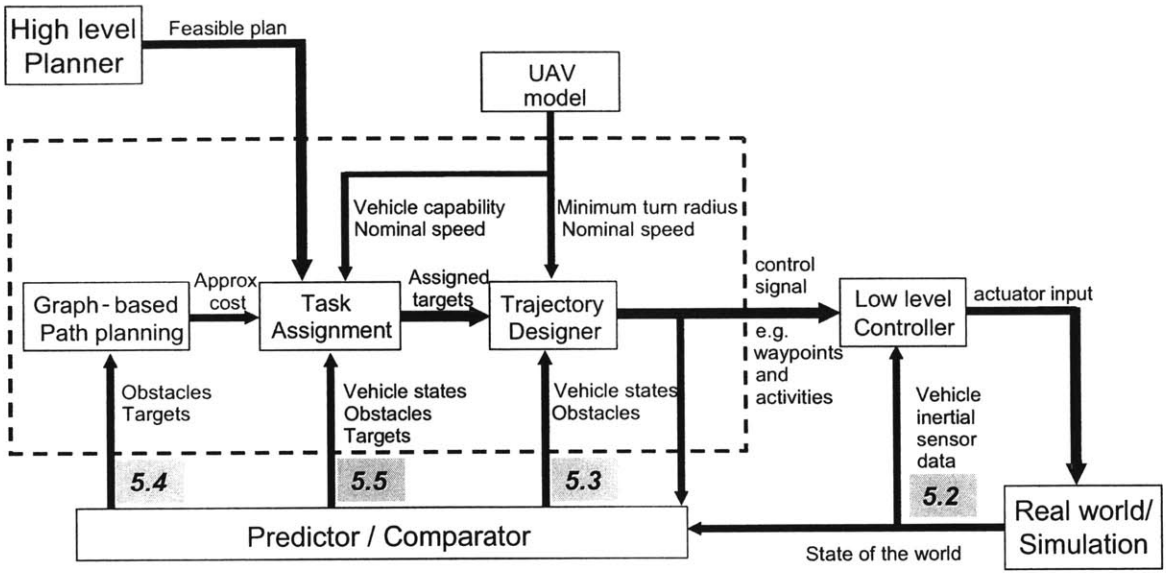

Figure 5-1: Loop closure at different levels. Numbers in gray boxes specify the section where the loop closure is discussed.

The first loop discussed in Section 5.2 is a traditional control loop between the actuator on the vehicles and the plant. This control loop receives a list of waypoints as a reference signal, and it outputs vehicle states. It is assumed that the low-level controller is able to follow the list of waypoints.

The second loop is closed in Section 5.3, which realizes on-line trajectory generation and execution. Compared to the first loop operating at 5 Hz, the second loop operates at a much lower frequency (updated once every 2$\sim$3 seconds) due to the heavy computational load of the trajectory optimization process and the time constant of vehicle dynamics. The following assumptions must hold to successfully close the second loop:

- The vehicle is able to execute the plan (*i.e.*, the plan is consistent with vehicle dynamics)
- A plan request is sent to the planner to initiate the trajectory planning. Very infrequent plan requests result in delayed trajectory generation, but overly frequent plan requests saturate the communication bandwidth.
- The plan request must be received by the planner, but in the real world, there is a

delay in this communication.

- The trajectory optimization problem is solvable.
- Before the vehicle finishes executing the current plan, the next plan is delivered to the vehicle.

These events must occur in this order until the vehicle completes the mission, which constitutes the *real-time* trajectory generation and execution.

When the third loop is closed in Section 5.4, the following assumptions are added to the ones stated above:

- Changes in the world are detectable and are reported to the planner.
- The changes in the situational awareness are captured by the predictor/comparator.
- Graph-based path planning rapidly updates the cost map.
- The trajectory designer can produce a plan that is consistent with the environment.

This allows the planner to account for the change in the situation awareness in real time at the trajectory design level.

The fourth loop is closed in Section 5.5. On-line task reassignment and trajectory generation by a centralized planner requires the additional assumptions:

- Each vehicle closes its loop with the planner at the same frequency. This is because the architecture presented here has one centralized planner that makes the plans for all the vehicles. This assumption can be removed if multiple planners are used in a distributed fashion.
- The low-level feedback controller enables each vehicle to reach the next waypoint at the time specified by the planner.

If any of the above assumptions does not hold, then the vehicles will exhibit abnormal behavior, such as a sudden stop, a go-around, or a significant deviation from the nominal path. The purpose of the experiments in this chapter is to verify the validity of these assumptions and to investigate the impact of unexpected disturbance sources present in the

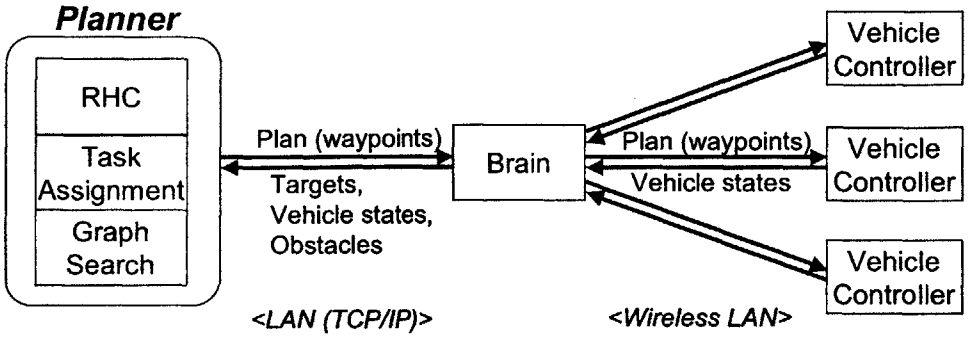

Figure 5-2: Planner and hardware integration

real world that the simulation fails to capture. This is accomplished by showing the testbeds controlled by the planning algorithm in real time with all loops closed.

5.2 Hardware Setup

This section describes two testbeds that were built to test the planning algorithms discussed in the previous chapters. First of all, Section 5.2.1 discusses the waypoint follower interface set up between the receding horizon trajectory designer and the two testbeds. In Section 5.2.2, the truck system is discussed as a ground-based testbed [33]. Section 5.2.3 describes the UAV testbed, which uses autopilots in a hardware-in-the-loop simulation.

5.2.1 Interface Setup

In the experimental demonstration, the RHC is used as a "high-level" controller to compensate for uncertainty in the environment. It designs a series of waypoints for each vehicle to follow. A "low-level" vehicle controller then steers the vehicle to move along this path. Figure 5-2 shows an interface set up between the planner and the testbed.

There is a central data manager labelled "Brain" that monitors the vehicle positions and sends plan requests to the planner, receives planned waypoints and sends them to each truck, and simulates changes in situation awareness such as obstacle detection and discovery

of new targets. Currently sensors are not implemented on the testbeds, thus the brain creates simulated sensor data based on the actual vehicle location. This allows us to evaluate how the different types of sensors impact the planning algorithm without actually implementing the hardware. This brain function fits in Figure 5-1 as a "Predictor/Comparator" block.

Both the ground-based truck and autopilot testbeds have the same interface to the planner, and the planning algorithm will be demonstrated on both. All of the data is exchanged between the planner, brain, and testbed vehicles via TCP/IP local area network connections, which can flexibly accommodate additional vehicles or another module such as a mission level planner and GUI for a human operator. This LAN communication has a bandwidth of 10Mbps, which is high enough to send vehicle states and planned waypoints. The CPU of the planner laptop is a Pentium IV 2.0GHz with 1 GB RAM, the fastest laptop available in 2002.

5.2.2 Truck Testbed

The truck testbed has been built with a view for future UAV control use. It represents models of UAVs, which would typically operate at a constant, nominal speed, flying at a fixed altitude, and with the turning rate limited by the achievable bank angle. The testbed described here consists of three remote-controlled, wheel-steered miniature trucks, as shown in Figure 5-3. In order to capture the characteristics of UAVs, they are operated at constant speed. Due to the limited steering angles, the turn rate of the trucks is also restricted.

Figure 5-4 is a block diagram of the truck testbed. The central base station has a fixed GPS antenna to enable differential GPS. Each truck has a Pentium III 850MHz laptop, a GPS antenna, a GPS receiver, and a PWM board that converts commands from the laptop into PWM commands for the steering and drive motors. Doppler velocity measurement provided by the GPS NAVSTAR constellation has high accuracy (standard deviation of 1-2 mm/sec) and is integrated to produce position measurement data [33, 34]. Each truck and base station runs the same GPS estimation program and they communicate via a built-in wireless LAN. This produces position estimates accurate to about 10 cm for the length of the experiments

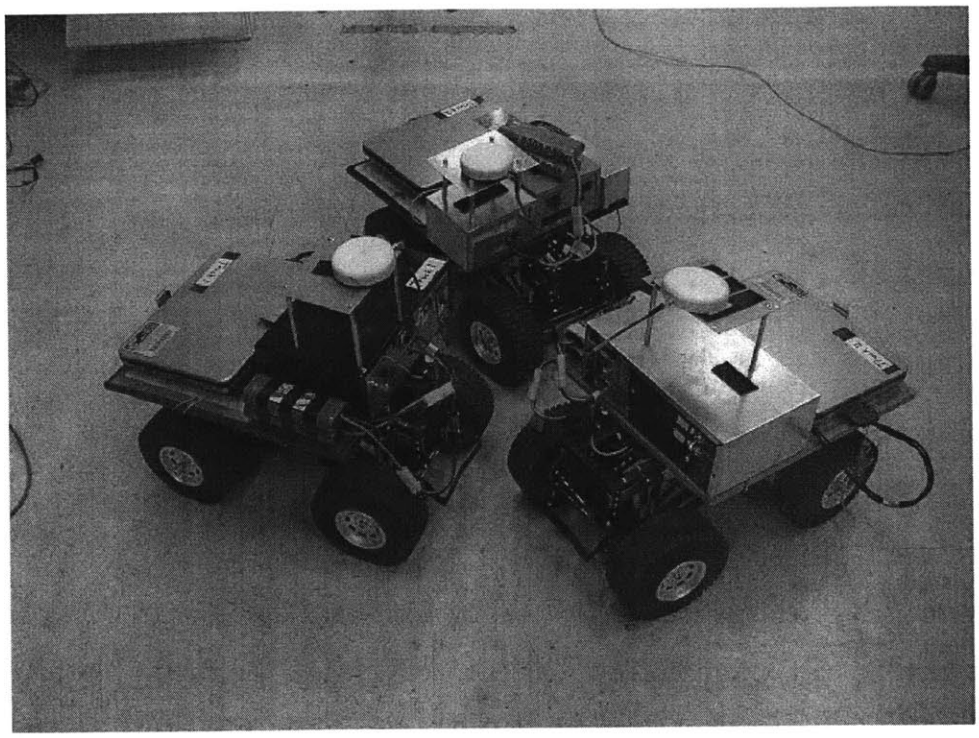

Figure 5-3: Three truck testbed showing the GPS antennas, the Sony laptops, and the electronics package.

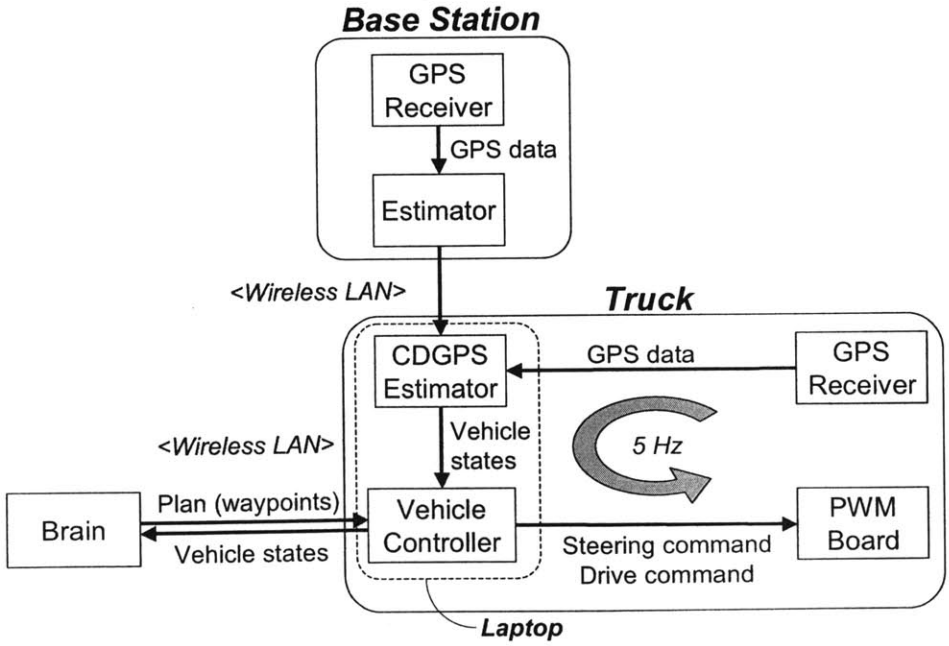

Figure 5-4: Truck testbed system diagram

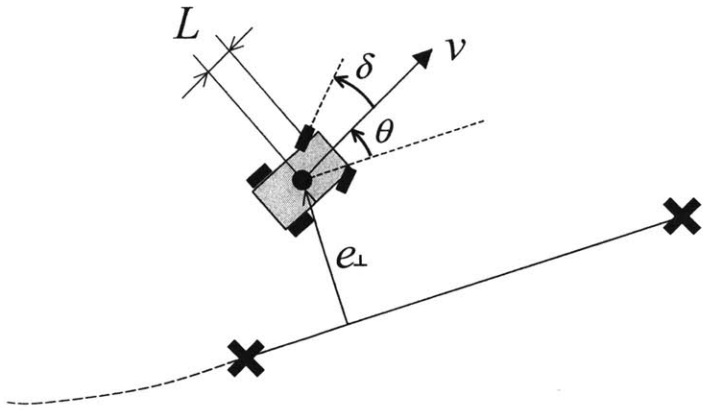

Figure 5-5: Waypoint following method for truck testbed

shown here. With an on-board laptop that performs the position estimation and low level control, the trucks can autonomously follow the waypoint commands. The more complex path planning is then performed off-board using the planner computer. This separation greatly simplifies the implementation (eliminates the need to integrate the algorithms on one CPU and simplifies the debugging process) and is used for both testbeds.

The on-board laptop controls the cross-track error and the in-track error separately, to follow the waypoint commands. The waypoint following algorithms are discussed in the next subsections.

Heading Controller

The trucks are capable of steering with only the front wheels to change their heading. The heading controller uses the latest two waypoints received from the planner as shown in Figure 5-5, which are updated once it obtains a new plan or once it reaches the waypoint that the vehicle is aiming for. A simple bicycle model [35] is used to capture the dynamics of the truck, which is written as

$$\dot{\theta} = \frac{v}{L}\tan\delta \simeq \frac{v}{L}\delta \tag{5.1}$$

$$\dot{e}_{\perp} = v\sin\theta \simeq v\theta \tag{5.2}$$

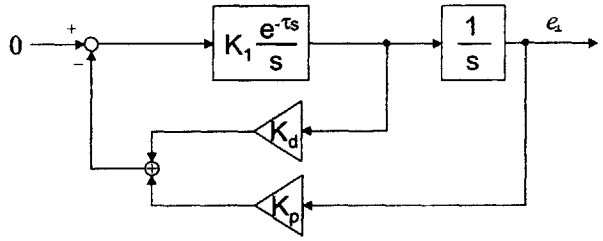

Figure 5-6: Heading control loop

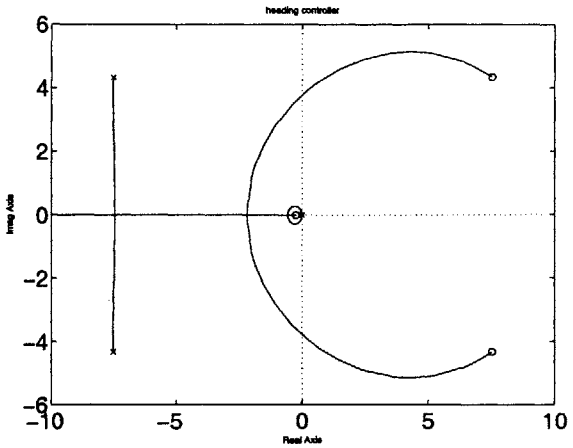

Figure 5-7: Root locus of the heading controller

$$\delta \simeq K_0 \, u_{\text{PWM}} \tag{5.3}$$

where L is an arm length from the center of mass to the center of the front steering axle, δ is the steering angle, $e_\perp$ is the cross-track position error, u_{PWM} is the command input to the PWM motor controller, and K_0 is a constant. The transfer function from the motor command to the cross-track error is

$$\frac{e_\perp(s)}{u_{\text{PWM}}(s)} = \frac{K_1}{s^2} \tag{5.4}$$

where $K_1 = v^2 K_0 / L$ is a constant. The system has been measured to have a transmission delay τ of approximately 0.4 seconds. By approximating the delay using a second order Padé approximation, the plant model G is

$$G(s) = \frac{K_1 e^{-\tau s}}{s^2} \simeq \frac{K_1 \left(1 - \frac{\tau s}{2} + \frac{(\tau s)^2}{12}\right)}{s^2 \left(1 + \frac{\tau s}{2} + \frac{(\tau s)^2}{12}\right)} \tag{5.5}$$

A double integrator system with delay can be stabilized using a PD controller. Figure 5-6 shows the block diagram of a heading control loop, and Figure 5-7 shows a root locus with

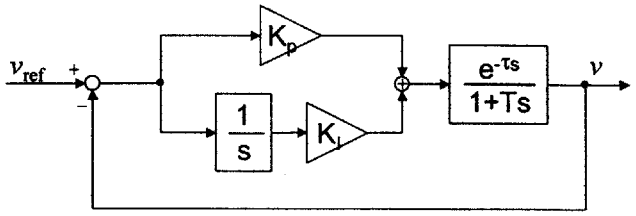

Figure 5-8: Speed control loop

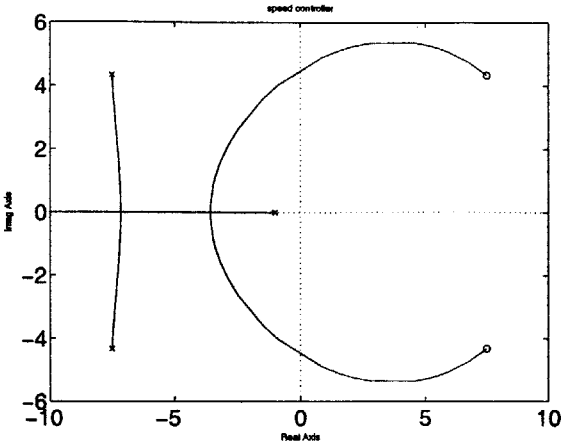

Figure 5-9: Root locus of the speed controller

a fixed compensator zero at -0.25.

Speed Controller

Figure 5-8 shows a control block diagram for the speed control loop. The speed motor is modelled as a first-order lag with the same transmission delay. It tracks the nominal speed while rejecting disturbances from the roughness of the ground and slope changes. In order to nullify any steady state error, a PI controller is implemented in this case. Figure 5-9 shows a root locus with a fixed compensator zero at -2. A more detailed analysis is given in Ref. [36]

5.2.3 UAV Testbed

A multi-aircraft testbed has also been built to test the control algorithms in real time. While the hardware testbed is being completed, we use the autopilots to perform hardware-in-the-loop simulations that give a high fidelity test of the planning algorithms for future outdoor experiments.

Figure 5-12 shows a block diagram of the UAV testbed with the autopilots. The autopilot on each aircraft controls the surfaces of the aircraft to make it follow a given list of waypoints.

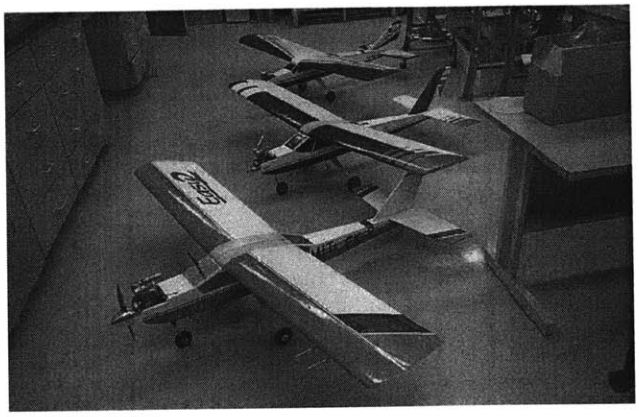

Fig. 5-10: PT40 Aircraft of the UAV testbed. Six aircraft are currently available.

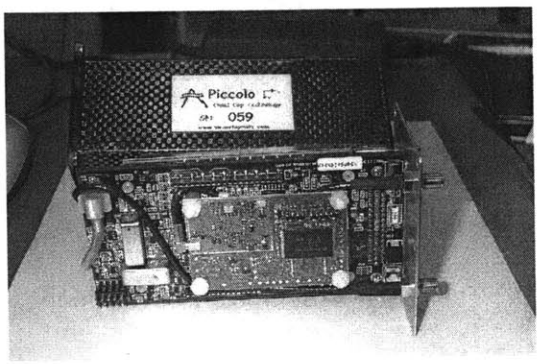

Fig. 5-11: The Cloudcap Piccolo^{TM} autopilot for the UAV testbed

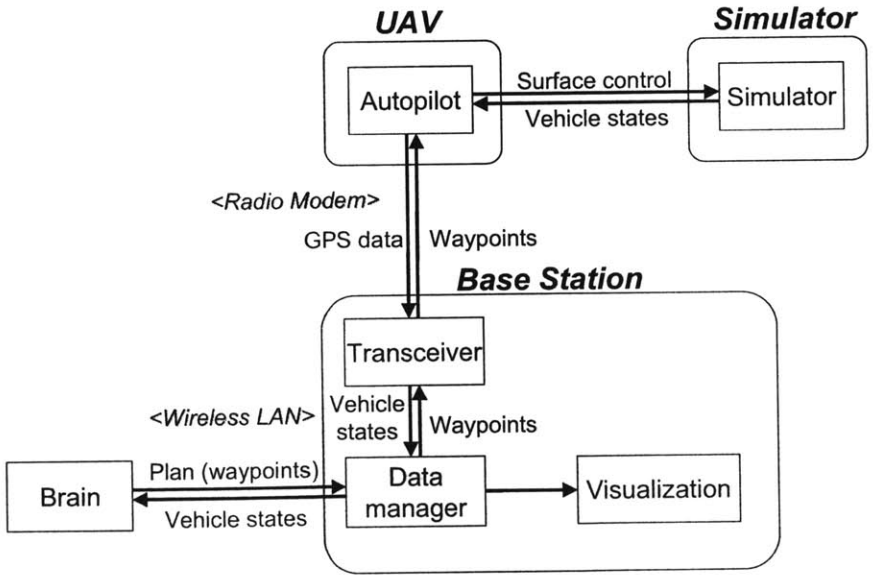

Figure 5-12: Autopilot testbed system diagram

It stores beforehand a list of precalculated waypoints for a circular holding pattern, and has the capability to operate autonomously, even in the absence of communication with the ground station. Each control surface has a PID controller and the signals are filtered to eliminate high frequency disturbances. The lateral track control loop is closed around these low-level controllers, as discussed in Ref. [37], and it coordinates the aileron and rudder when making a turn. The speed controller tracks the reference speed, but it also maintains the nominal altitude of an aircraft.

Each testbed has different strengths. The trucks are physically moving vehicles and allow the tests to be conducted in a real environment; it is also able to stop, which makes debugging easier than with the flying vehicles; the test area does not need to be vast since they can move at a much slower speed. The UAV testbed gives flight data based on actual aircraft dynamics, which allows us to evaluate the aircraft dynamics model used in the planning/simulations; the hardware-in-the-loop tests done here are exactly the same as it will be when the actual flight tests are conducted; it also enables a lot of trials in a complex environment without the risk of actually losing a vehicle.

5.3 Receding Horizon Controller with Low-Level Feedback Controller

This section demonstrates that the receding horizon controller presented in Chapters 2 and 3 can actually be implemented on the hardware testbed presented in Section 5.2 and is continually able to generate a plan in real time.

5.3.1 On-line Replanning Concept

Figure 5-13 illustrates a time-line of an on-line receding horizon trajectory generation. The horizontal axis represents time and the vertical axis represents distance. A vehicle moving at a constant speed v is expressed as a straight line with slope v in this figure. A gray box with a plan number expresses the computation task of the planner: the height represents the

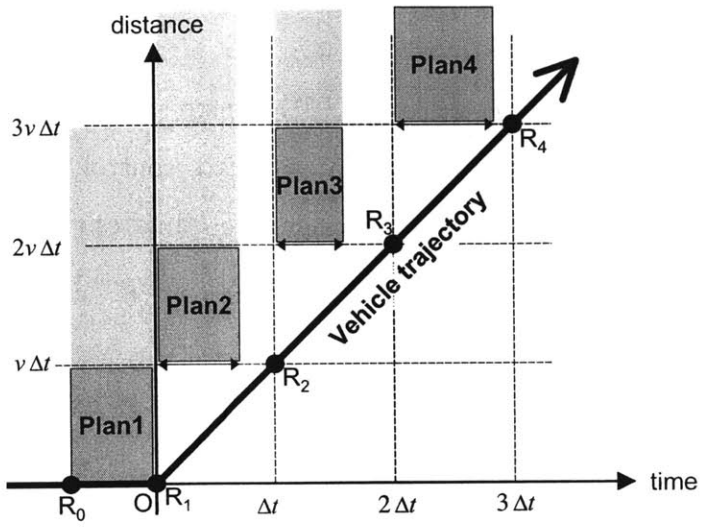

Figure 5-13: Distance travelled and elapsed time

range covered by the plan and the width represents computation time. As an example, the execution horizon is set to be one step and the planning horizon is three steps in this figure.

Before starting, the vehicles need to be navigated to the initial location for the planner. By then, the first plan for time $0 \leq t \leq \Delta t$ is generated. Unlike the UAV testbed, with the truck testbed, the planner is able to use the initial positions of the trucks as initial states, because they are able to stop. While the vehicle is executing plan 1, the next plan (plan 2 in the figure), which starts on the execution horizon of plan 1, is solved. Plan 2 must be generated before the vehicle reaches the end of plan 1 (marked $\mathbf{R}_2$): more generally, the gray boxes must not intersect the straight line representing the vehicle trajectory. Otherwise, the vehicle has no waypoints to follow. When it reaches $\mathbf{R}_2$ and starts executing plan 2, a plan request is sent to the planner and the planner starts solving for plan 3. In summary, the replanning procedure is as follows:

1. Compute the cost map.
2. Solve MILP minimizing J in Eq. 2.56 subject to Eqs. 2.2 to 2.57, starting from the last waypoint uploaded (*or initial state if starting*).
3. Upload the first n_e waypoints of the new plan to the vehicle.

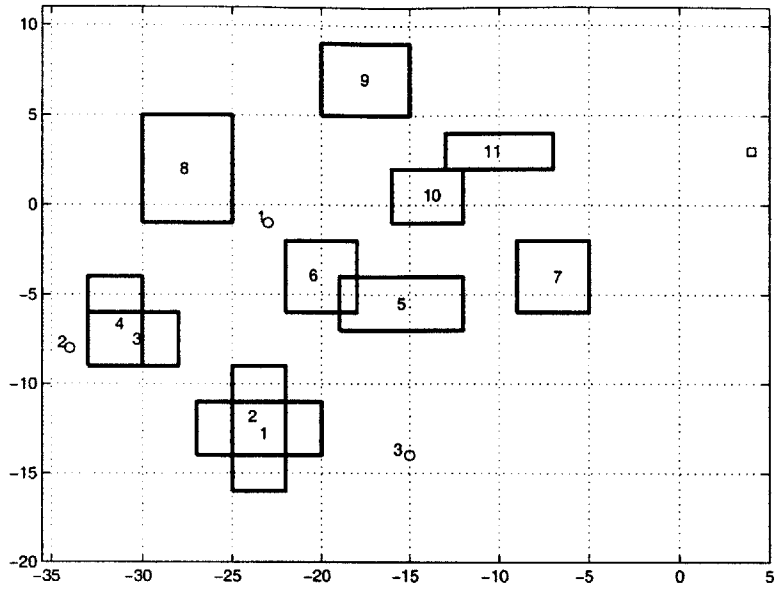

Figure 5-14: Complex scenario for one vehicle

4. Wait until the vehicle reaches the execution horizon of the previous plan.
5. Go to 2.

It is assumed that the low-level controller can bring the vehicle to the execution horizon of the plan in step 4. If the vehicle deviates from the nominal path, it is possible to use the propagated states as the next initial state in step 2, instead of the last waypoint uploaded to the vehicle.

5.3.2 Scenario

The following parameter values are used in the truck demonstration to test the algorithm shown above. Since the test area has a limited space, the nominal speed v is set to be as small as possible, which is 0.5 m/s for the current truck testbed. Since the trucks have a limited steering angle, a minimum turning radius $r_{\min}$ of 1.5 m is used. The step size $v\Delta t$ of 1.3 m has been selected to allow for the damping of cross-track error by the low-level feedback controller. This gives Δt of 2.6 sec, a requirement on the planning time to close the loop in real time. With these parameter values, a margin of three steps is required for a

stable controller, as was shown in Table 3.2. Vehicle states are reported at 2 Hz so that ~5 data points are obtained between each waypoint.

Figure 5-14 shows a complicated scenario where three goals marked with circles are located in an area with 11 obstacles. The initial location of the vehicle is marked with a small square in the upper right of the figure. The goals are already ordered with the label next to each target showing the order. Several path decisions can be made when visiting these three goals in this order.

The results of the on-line planning and execution are summarized in Figures 5-15 to 5-18. Figure 5-15(a) shows the entire trajectory of the plan (marked with $\times$) and the actual vehicle position marked with $\bullet$. The low-level feedback controller enables the vehicle to follow the planned waypoints with high accuracy while rejecting disturbances from the ground such as bumps and slope changes, as expected. The original obstacles were not penetrated by the actual truck. Figure 5-15(b) is a closeup of the tight turns around the obstacle at the left of (a). Note that there is some overshoot due to the tight turns, but this is sufficiently small.

Figure 5-16 shows the computation time of each plan, which is an elapsed time from when the planner receives a plan request to when it sends back a new plan. The peaks are observed when the vehicle goes through narrow passages (at plan numbers 11 and 38), when the vehicle makes a sharp turn (plan number 34), and when there is more than one option for a similar cost-to-go (plan number 13 as shown in Figure 5-17). However, all the plans are made in less than $\Delta t = 2.6$ [sec]. If the planning time is too long and the truck reaches the execution horizon without the next plan to execute, it will stop. However, the speed profile of the mission (Figure 5-18) demonstrates that this did not happen. The results in this section show a successful integration of the receding horizon controller and the on-board low-level feedback controller to provide an on-line planning capability.

The new pruning algorithm presented in Chapter 3 had not been implemented when we conducted this experiment. However, the computation time for the same scenario with this new algorithm was predicted using a simulation, and the results are shown in Figure 5-19. The results clearly show that the algorithm significantly reduces the computation time, while

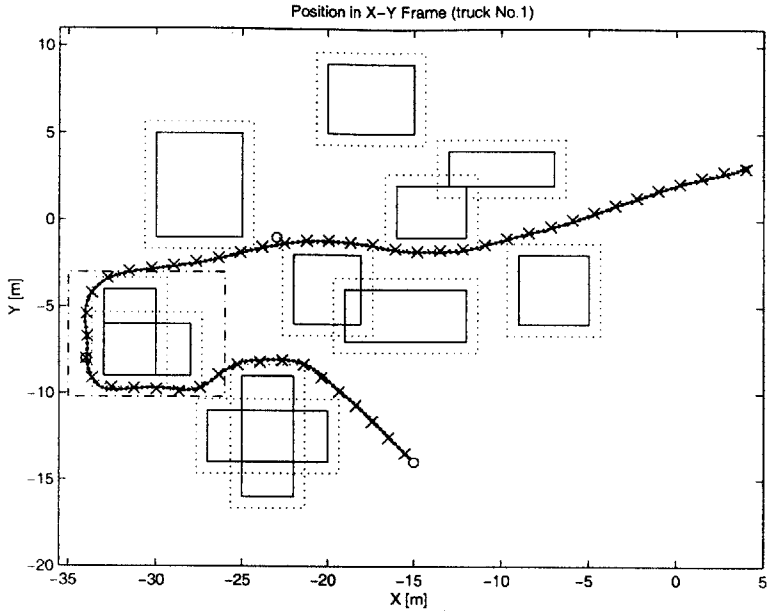

(a) Entire trajectory

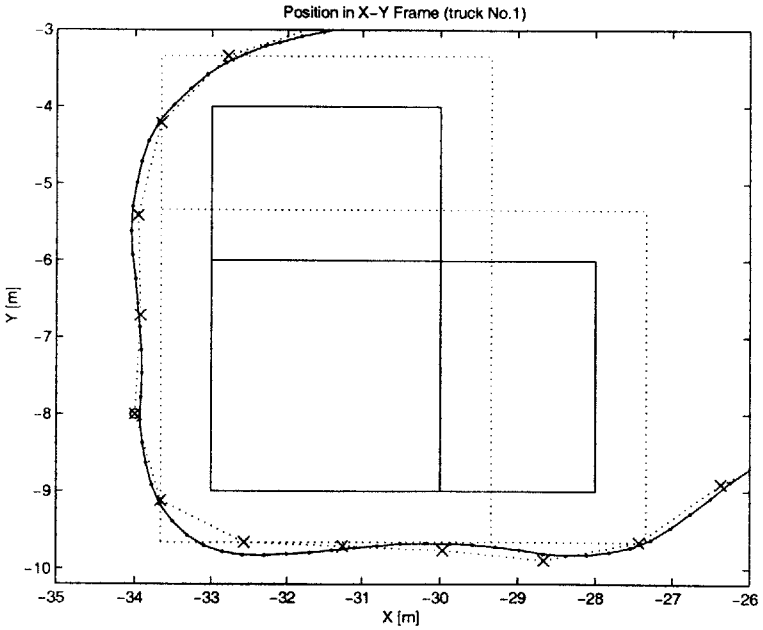

(b) Close-up of

Figure 5-15: Planned waypoints and actual position data of truck

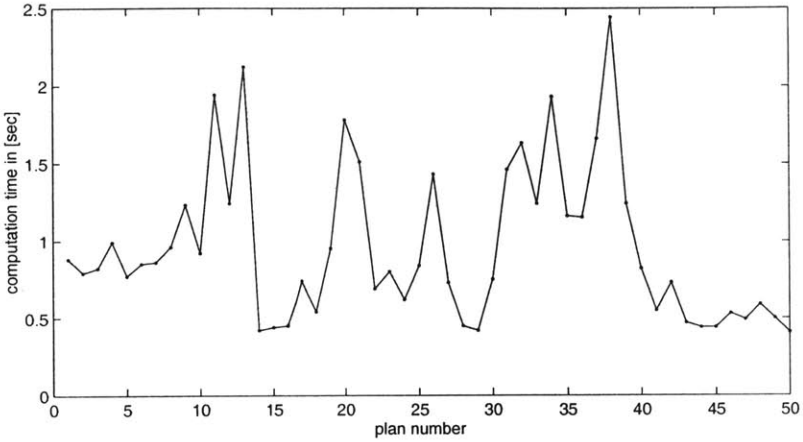

Figure 5-16: Computation time

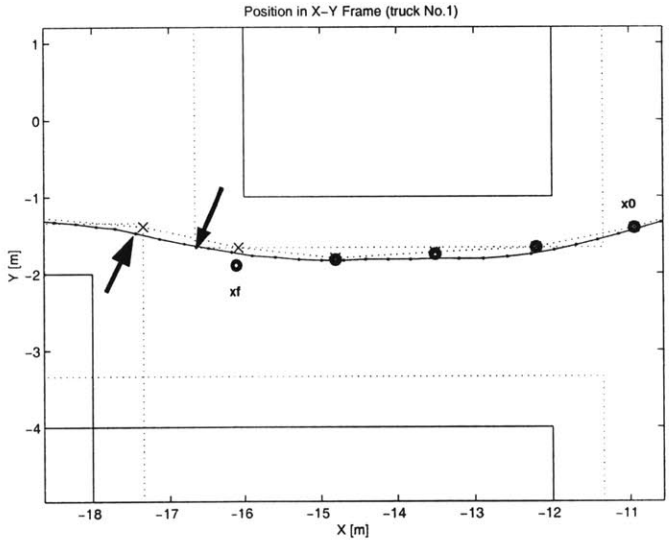

Figure 5-17: Close-up of the trajectory of plan number 13. The arrows specify two cost points that result in the very similar terminal costs. The initial point is on the right, and • marks show the detailed trajectory starting from the initial point. At plan number 13, the left cost point is chosen as the visible point. Sequential receding horizon optimization refines this selection as the vehicle proceeds. The resultant trajectory is shown with × marks.

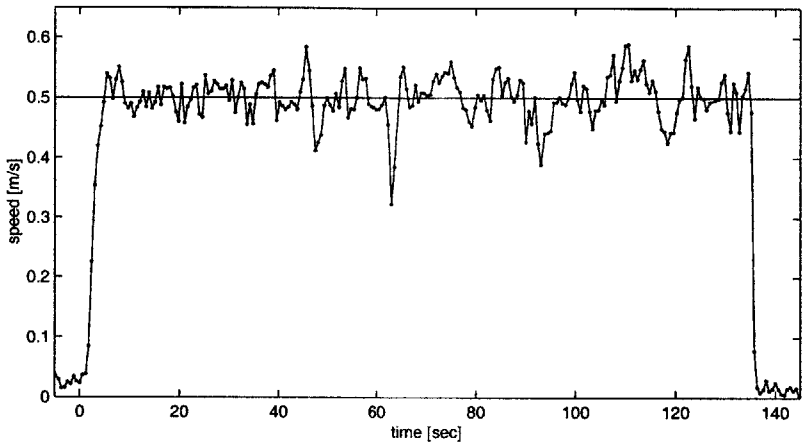

Figure 5-18: Speed profile. Actual average speed is 0.4979 m/s. The nominal speed of 0.5 m/s is also shown.

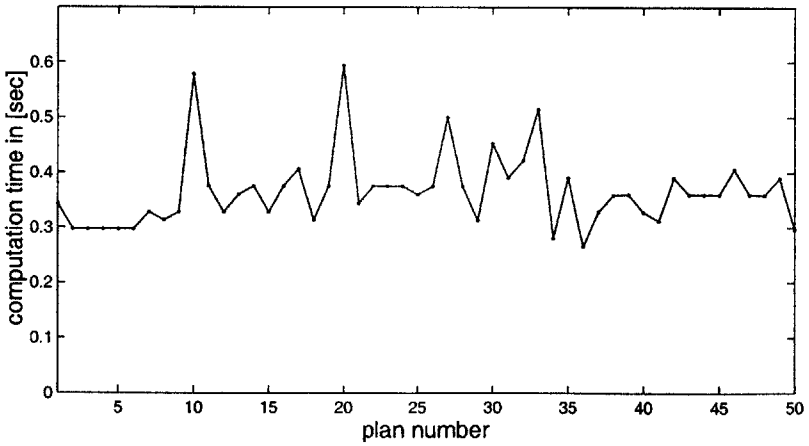

Figure 5-19: Computation time of the planner with the improved pruning algorithm

producing the same waypoints used during the experiments on the testbed. Future work will confirm that this algorithm achieves the same performance in the real environment with this much lower computation.

5.4 On-line Trajectory Regeneration

The previous section demonstrated an on-line trajectory generation using the MILP RHC in a static environment. In this case, the entire plan can be made off-line under the assumption that the low-level feedback controller always rejects disturbances and brings the vehicle back to the nominal path. However, UAVs flying in an uncertain world typically discover new information along the way to the target. This section demonstrates the flexibility of the RHC when the previous decision is no longer a good option.

5.4.1 Obstacle Detection

This subsection addresses the way to handle new information about obstacles. Obstacles exist between the vehicle and its goal, but the controller does not become aware of unknown obstacles until the vehicle is within a "detection horizon" of the obstacle. This simulates the operation of sensors with a limited range, such as laser radar, which can detect obstacles only within a certain radius. When a vehicle finds a new obstacle, the planner should be able to autonomously avoid it and guide the vehicle to the goal along the best available path.

Detection scheme

When a new obstacle is detected, the obstacle size has to be estimated. As a baseline, the first detection scheme provides the exact obstacle size [14]. The assumption here is that the vehicle has information about the shape of the obstacle and only its location is unknown. In this scheme, once any portion of an obstacle is detected by the vehicle, the entire obstacle becomes known, and the cost map is updated accordingly.

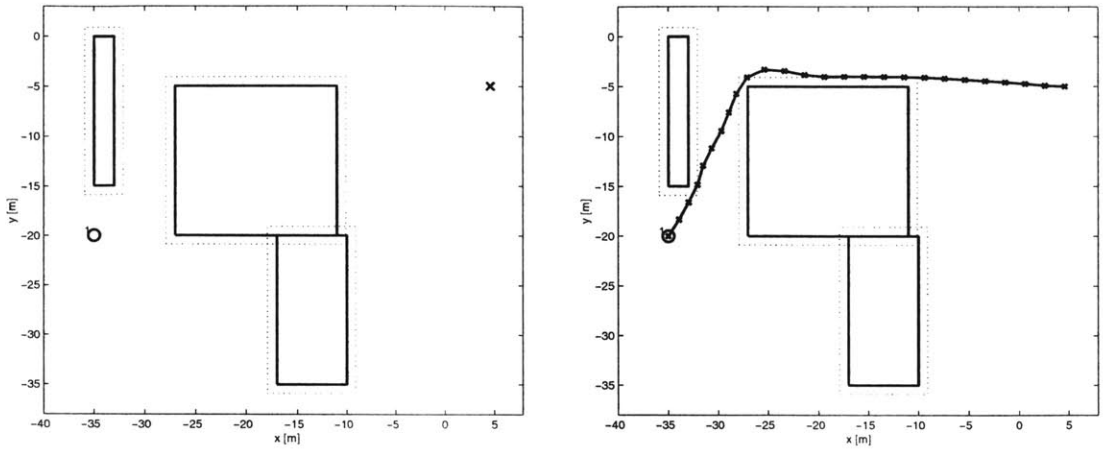

Figure 5-20: Scenario and trajectory based on full knowledge of the environment.

The next detection scheme assumes that the obstacle is small. In this optimistic estimate, there is no unknown obstacle beyond its detection horizon. Once a new obstacle is detected, only the detected portion is considered as an obstacle and the smallest possible rectangle is used to update the cost map.

The third detection scheme assumes that the newly detected obstacle is large. In this pessimistic approach, once the edge of an obstacle is detected, the edge is considered to be fairly long unless a corner of the obstacle is detected. Note that the RHC requires a feasible cost map to estimate the unplanned part of the path, and the estimated edge length must be finite.

In order to show the difference between these detection schemes, these three approaches are applied to the same scenario, shown in Figure 5-20(a). The vehicle starts at the upper right $\times$ mark, and goes to the goal marked with a circle in the lower left of the figure. There are three obstacles, but only the one in the center is unknown. Figure 5-20(b) shows the optimal trajectory that would be obtained by the RHC if the vehicle had perfect knowledge of the environment.

Figure 5-21 shows the simulation results of the first detection scheme. The large circle in Fig. (a) shows the detection range of the vehicle. When the detection circle intersects the

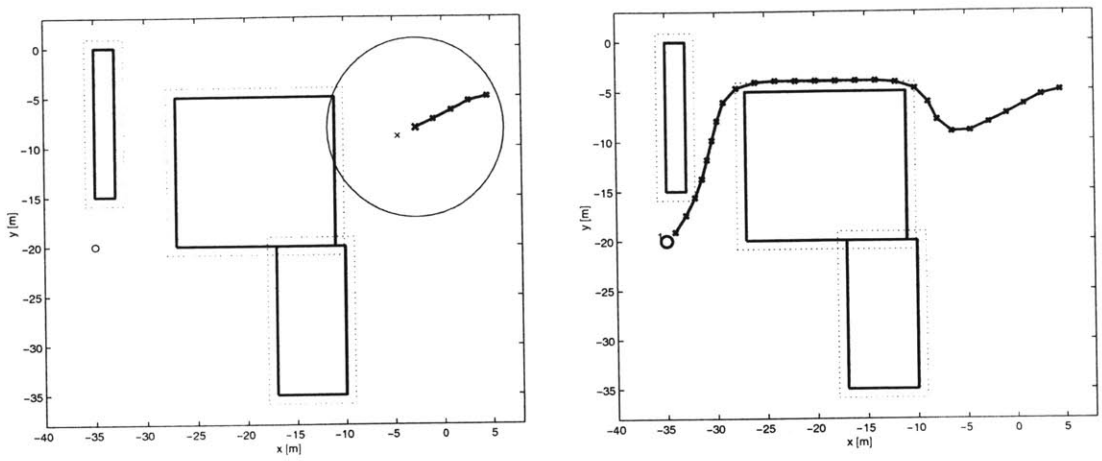

(a) (b)

Figure 5-21: Detection of an obstacle with previously known shape.

actual obstacle, the whole obstacle pops up. The trajectory designed afterwards takes it into account (Fig. (b)). The RHC made the best decision based on the available information, but the trajectory is longer than the optimal trajectory shown in Figure 5-20(b), and it requires a sharp turn after the obstacle detection.

Figure 5-22 shows the trajectory generated by the optimistic approach. The actual edges of the unknown obstacle are represented with dotted lines. The box with the dashed lines are the estimated obstacle used in the MILP planner. When the detection horizon intersects the unknown obstacle (Fig. (a)), only a portion of the obstacle in the detection horizon is considered to be an obstacle. As stated in Eq. 2.21, the obstacle is enlarged by $v\Delta t/2\sqrt{2}$ to form the estimated obstacle for the planner. In this optimistic case, the vehicle tries to go between the partially known obstacle and the lower obstacle (Fig. (b)). However, as the vehicle proceeds, more of the obstacle is found and it realizes that the two obstacles are actually connected (Fig. (c)). Furthermore, since going below both of them will result in a longer path than going above them, the planner changes the path decision (Fig. (d)), still basing this decision on an optimistic view of the world. As the vehicle proceeds, the size of the estimated obstacle keeps growing until the vehicle discovers three corners of the rectangle and determines the whole shape (Fig. (e)). The whole trajectory shown in Fig. (f) is quite

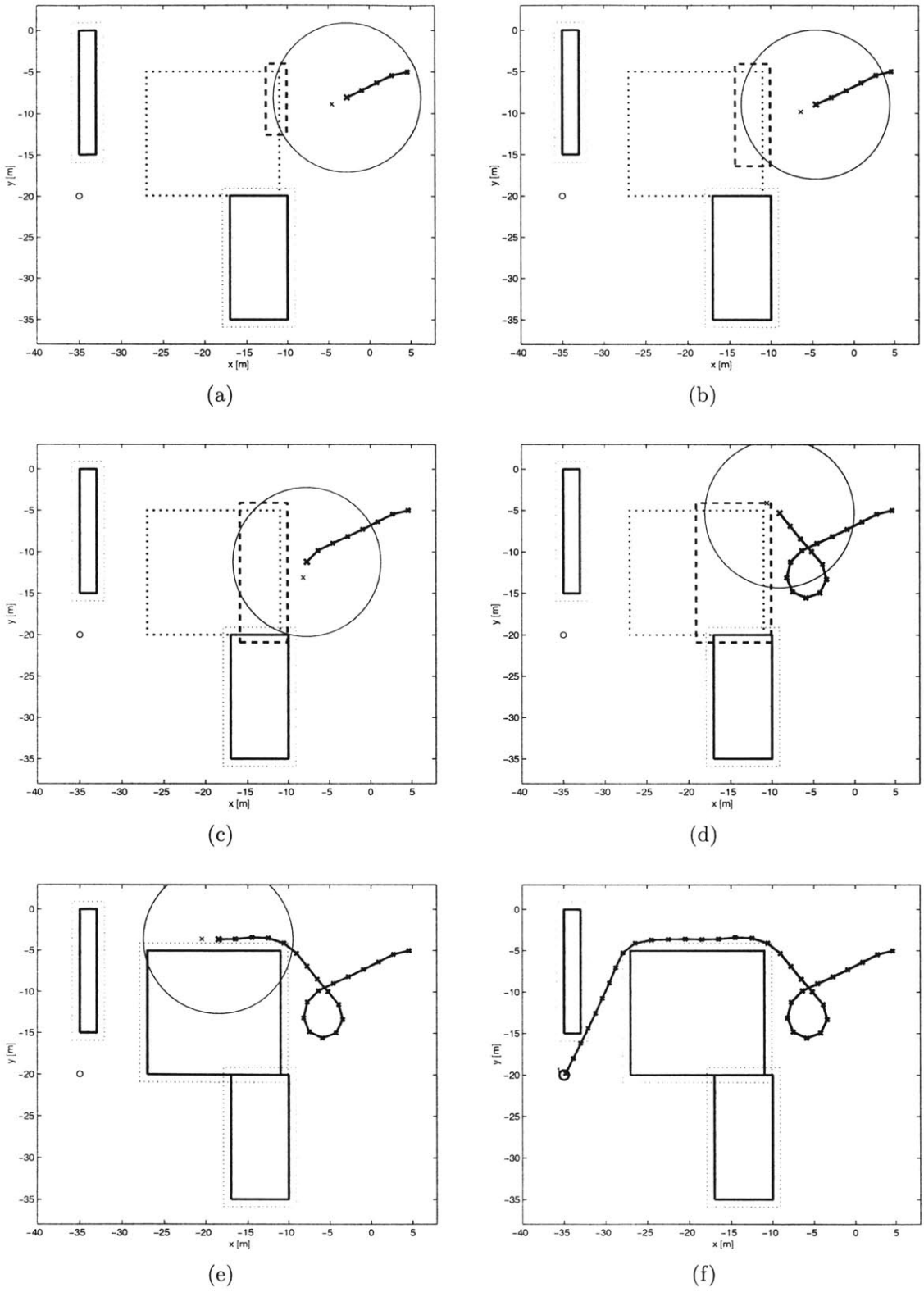

Figure 5-22: Estimation of an obstacle with an optimistic view of the world.

different from Figure 5-21(b) because of the original optimistic view of the world: when the vehicle detected the obstacle, the planner had to make a suboptimal decision.

Figure 5-23 shows the case of a pessimistic estimate of partially known obstacles. In this case, if the end points of an obstacle boundary are unknown, then they are assumed to be three times longer than the detection range. When the vehicle first detects the obstacle in Figure 5-23(a), only one of the four corners is known, and thus the obstacle is estimated to be two long walls around the known corner. As a result, the vehicle aims for the upper edge of the obstacle in the upper left (Fig. (b)) since it assumes that the partially known obstacle is large. When another corner is detected (Fig. (c)), the vehicle finds a better path between the two obstacles, and changes its decision.

The optimistic detection scheme allows the vehicle to aggressively approach a narrow passage assuming it is there, but can pay a higher price if it is not. This seldom happens in a scenario where obstacles are sparse. In such a case, the optimistic detection scheme outperforms the pessimistic scheme. The more pessimistic estimate tends to go around most of the obstacles, but it gives a safer trajectory. The larger detection horizon allows the vehicle to react to pop-up obstacles at an earlier stage, and also enables the planner to produces safer trajectories. Thus, the pessimistic approach is preferred for less agile vehicles. The selection of detection scheme is scenario/vehicle specific and can be determined by a human operator.

Truck Experiments

This section describes the application of the previous section's formulation to the truck testbed. The low-level feedback controller has the responsibility of ensuring that the vehicle reaches the prescribed waypoint. The high-level MILP controller closes a different real-time loop, as it compensates for obstacle information that only becomes available as the vehicle moves. The truck was modelled as having a nominal speed of 0.5 m/s, equal to the nominal running speed. The modelled maximum turn rate was 10 deg/s, chosen to give smooth operation when using the low-level steering controller. This produces a minimum turning

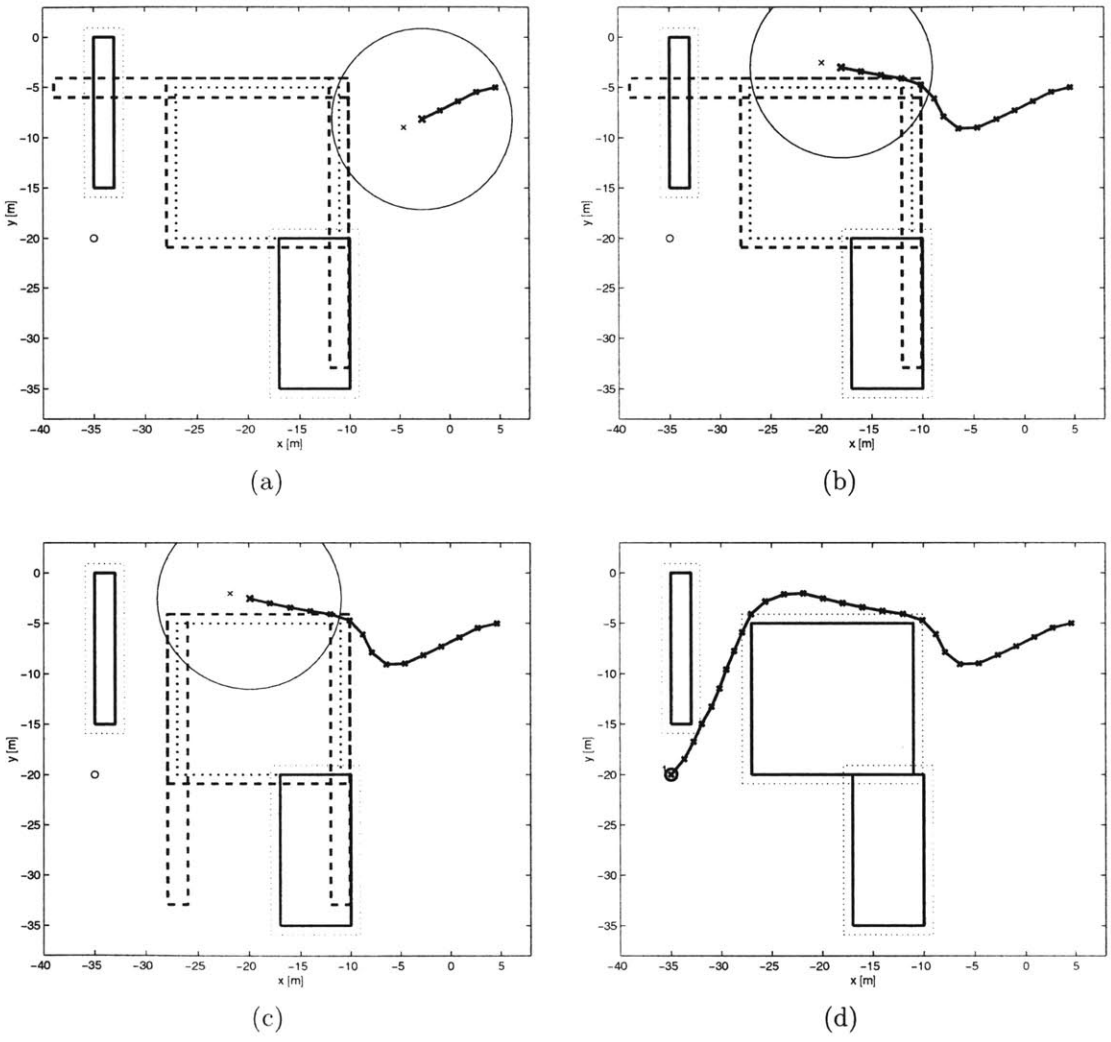

Figure 5-23: Estimation of an obstacle with a pessimistic view of the world.

radius of 2.8 m. The system was discretized with a time step length of 4 seconds, long enough for the transient of the low-level steering controller to decay. The planning horizon was five steps, equivalent to 10 m. The execution horizon was one step: before each plan was found, only one new waypoint was executed by the truck.

The detection horizon was 9.5 m, which enables the truck to perform collision avoidance maneuvers once it detects a new obstacle. Initially, the cost map is computed using only known obstacles and those within the detection horizon of the starting point. At each step, before the trajectory design phase, the circle around the current position called the detection horizon is checked for intersections with new obstacles. If any are "found," the cost estimation is repeated with the updated obstacle information. This cost estimation process can be extended to incrementally update the cost map using local information.

In summary, the control scheme is as follows[1]:

1. If the detection circle intersects any "unknown" part of the obstacles (*or if starting*), compute the cost map, including all obstacles currently known.
2. Solve MILP minimizing J in Eq. 2.56 subject to Eqs. 2.2 to 2.57, starting from the last waypoint uploaded (*or initial state if starting*).
3. Upload the first n_e waypoints of the new plan to the vehicle.
4. Wait until the vehicle reaches the execution horizon of the previous plan.
5. Go to 1.

The optimistic approach of the detection scheme is selected as a test scenario since, with this approach, the vehicle constantly updates the obstacle information as it gets closer to the obstacle. The scenario can be seen in Figure 5-24(a). The truck begins at $(4.5, 5)$, heading in the direction of the goal $(-35, -20)$. Two obstacles marked by the solid black line are initially known. There is another obstacle, marked by dots, blocking the direct path to the goal. However, it is not initially known to the planner. To successfully complete the test, the vehicle must move around the obstacle, once aware of its presence, and reach the goal.

[1]Compare with the one for a stationary environment (p.101).

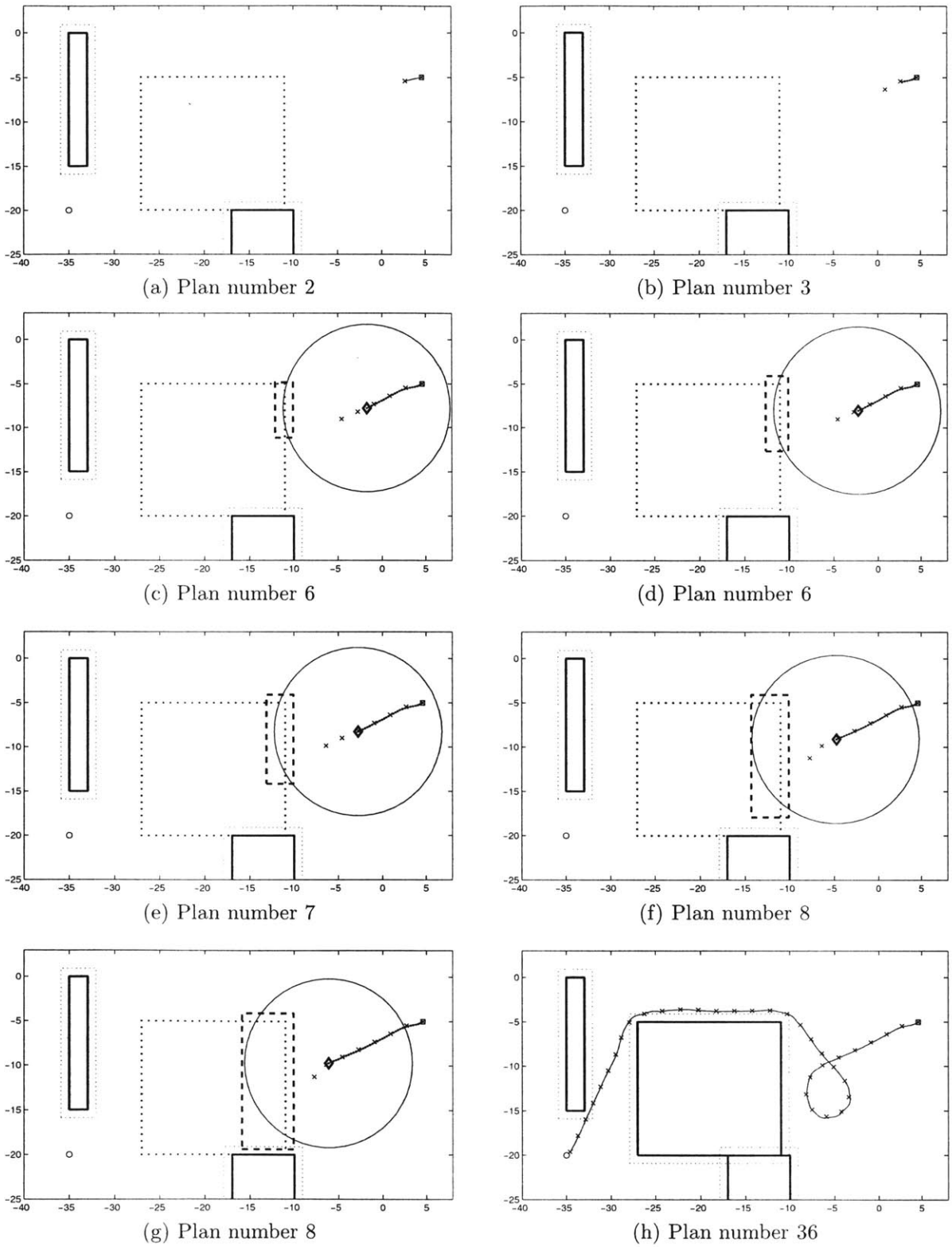

(a) Plan number 2

(b) Plan number 3

(c) Plan number 6

(d) Plan number 6

(e) Plan number 7

(f) Plan number 8

(g) Plan number 8

(h) Plan number 36

Fig. 5-24: Planned waypoints ($\times$) and actual truck trajectory ($\cdot$). The large circle is the detection range centered at the $\diamond$ mark.

The result is shown in Figure 5-24. In Fig. (a), the first plan from the initial position over the execution horizon has been sent to the truck controller. Since it is not aware of the obstacle in the middle, the planner has commanded a path directly towards the goal. The truck starts moving and the planner starts solving for the next plan, starting from the execution horizon of the previous plan.

One second later, having completed the new plan, the next waypoint has been uploaded. When the truck is about to reach the waypoint sent from the first plan as shown in Fig. (b), it sends a plan request. The obstacle has not yet been detected, and the path to be designed is still headed straight to the goal.

In Fig. (c), the unknown obstacle is detected when it comes within the detection horizon of the truck. Note that obstacle detection is based on actual truck position and obstacles. The next waypoint is uploaded, with the trajectory still heading straight to the goal since the last plan was not aware of the obstacle. However, when the next plan request is received (Fig. (d)), the planner recomputes the cost map including the detected part of the obstacle before making the next plan. The new map includes the enlarged obstacle, shown by the dashed line. The next plan obtained in Fig. (e) reflects the detected obstacle information and leads the truck to go below the obstacle. Since this plan is based on the obstacle information in Fig. (d), the change is not immediately apparent. The size of the detected obstacle keeps growing as the vehicle proceeds, however, and the next plan in Fig. (f) is based on the larger obstacle.

As stated above, there is a delay between the obstacle detection and the newly generated plan based on the detection. A more reactive controller could be incorporated to reduce this delay: when it detects a new obstacle, the reactive controller rapidly makes a feasible path based on local information, and gives the terminal point to the MILP controller as the initial state of the next plan. The MILP RHC would then solve for the next optimal plan starting from this propagated initial state while the truck executes a plan generated by the reactive controller. A reactive planner is currently being implemented on the testbed to evaluate the feasibility of this approach.

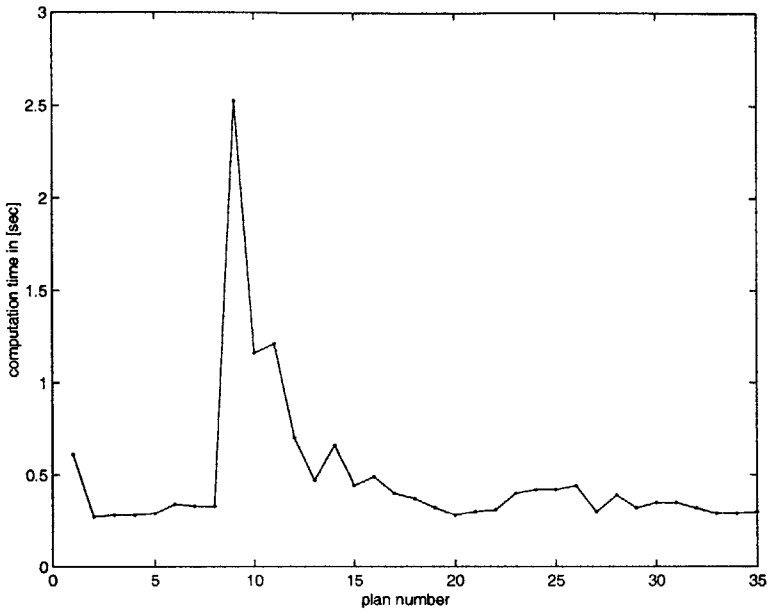

Figure 5-25: Computation time for obstacle detection scenario

When the partially known obstacle overlaps another obstacle, as shown in the bottom of Fig. (g), the vehicle needs to go above both obstacles, and the next couple of planned waypoints require a very sharp turn at the minimum turning radius. Figure 5-24(h) shows all of the planned waypoints with $\times$ marks and the vehicle trajectory marked with a solid line. Note that, even with the very large unknown obstacle in the environment, the truck successfully completed the maneuvers and visited the goal.

The computation time for each plan generation is shown in Figure 5-25. All of the computation was done within the 4 second time step, which demonstrates the real-time implementation of MILP. The longest computation time occurred for the ninth plan, when the initial heading of the vehicle was pointing at the bottom of the figure and the best visible node was behind the vehicle. This is the worst case scenario for the vehicle; designing a feasible path requires that the constraints on maximum acceleration, maximum speed, and minimum speed are all active for each waypoint in the plan. These results clearly show that the receding horizon MILP can be used to navigate an uncertain environment with obstacles. They also show the scenarios that lead to worst case computation times. Current work is focused on developing techniques to reduce this computation time. The two-level con-

trol architecture allows the on-line planner to compensate for obstacle discovery beyond the execution horizon while low-level feedback rejects vehicle disturbance within that horizon.

5.4.2 Collision Avoidance Maneuver

The control laws for the low-level feedback loops described in Section 5.3 account for the error in the cross-track direction and the error from the nominal reference speed. Although the PI speed controller does not have a steady state speed error, it cannot completely nullify the in-track position error. This in-track error translates into an error in the time-of-arrival at each waypoint. Failure to meet a timing constraint can cause a significant problem when coordination of multiple vehicles is required. This subsection demonstrates, using an example based on a collision avoidance maneuver, that the MILP RHC can re-optimize the trajectory on-line, accounting for in-track position errors. It also modifies the cost-to-go to improve the performance of the collision avoidance maneuver.

Cost-To-Go in Relative Frame

In the trajectory design problems for multiple UAVs, the vehicle avoidance constraints become apparent only when the two vehicles come close to each other. This allows us to solve the trajectory optimization problem without including the full set of vehicle avoidance conditions, which reduces the number of binaries and the computation load. However, when the planned trajectories for the multiple vehicles intersect with each other, another algorithm is required that focuses on avoiding collisions.

The cost-to-go method presented in Section 2.4 does not take into account the vehicle collision avoidance beyond the planning horizon if it is applied to more than one vehicle. Figure 5-26 shows that this approach can lead to a sub-optimal decision if collision avoidance is a dominant factor in determining the trajectory. In this example, the two vehicles start at the right heading towards the left. Their goals are placed such that the two vehicles must switch their positions in the y direction. Fig. (b) shows the relative positions beginning at the top of the figure and descending to the goal marked with $\circ$, where the relative frame for

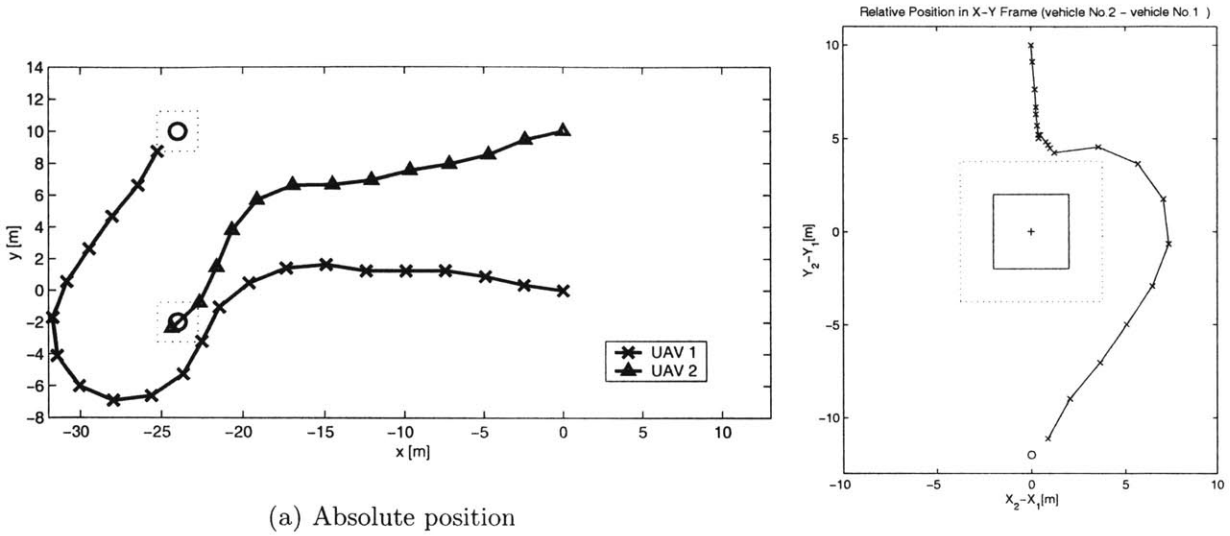

(a) Absolute position

(b) Relative position

Figure 5-26: Collision avoidance maneuver with naive cost-to-go.

two vehicles 1 and 2 is defined as $\boldsymbol{x}_2 - \boldsymbol{x}_1$. The square in the center represents the vehicle avoidance constraints.

Each vehicle tries to minimize the distance from its planning horizon to its goal in the absolute frame, while satisfying vehicle avoidance constraints over the planning horizon. In the relative frame, this is equivalent to moving straight to the goal, neglecting the vehicle avoidance box. The two vehicles do not start the collision avoidance maneuver until the vehicle avoidance constraints become active. As shown in Fig. (a), when they get closer to their goals, one of them chooses to arrive at the goal in the planning horizon to reduce the terminal penalty (TOA in Eq. 2.55). This decision causes the second vehicle to go around the vehicle, resulting in a much longer trajectory, both in the absolute frame (Fig. (a)) and in the relative frame (Fig. (b)).

The problem formulation can be improved by including the relative vehicle positions in the cost function. As shown previously, the optimal trajectory for a vehicle flying in an environment with obstacles tends to touch the obstacle boundaries. In this case, the heuristic in Ref. [13] that uses the obstacle corners as cost points successfully finds the shortest path.

In the vehicle avoidance case, a similar heuristic is that the optimal trajectory will tend to "follow" the vehicle avoidance box in the relative frame. Therefore, the modified formulation presented here uses the four corners of the vehicle avoidance box and a relative position of the two goals as the cost points $[\boldsymbol{x}_{\text{cp}}, \boldsymbol{y}_{\text{cp},}]^T$ in the relative frame. Eqs. 2.29 to 2.38 in Chapter 2 are replaced with the following equations. For any pair of two vehicles j and k $(j < k)$,

$$c_{\text{vis},jk} = \sum_{i=1}^{5} c_i \, b_{\text{cp},ijk} \tag{5.6}$$

$$\sum_{i=1}^{5} b_{\text{cp},ijk} = 1 \tag{5.7}$$

$$\begin{bmatrix} x_{\text{vis},jk} \\ y_{\text{vis},jk} \end{bmatrix} = \sum_{i=1}^{5} \begin{bmatrix} x_{\text{cp},ijk} \\ y_{\text{cp},ijk} \end{bmatrix} b_{\text{cp},ijk} \tag{5.8}$$

$$\begin{bmatrix} x_{\text{LOS},jk} \\ y_{\text{LOS},jk} \end{bmatrix} = \begin{bmatrix} x_{\text{vis},jk} \\ y_{\text{vis},jk} \end{bmatrix} - \begin{bmatrix} (x_{n_p})_k - (x_{n_p})_j \\ (y_{n_p})_k - (y_{n_p})_j \end{bmatrix} \tag{5.9}$$

$$\begin{bmatrix} x_{\text{test},jkm} \\ y_{\text{test},jkm} \end{bmatrix} = \begin{bmatrix} (x_{n_p})_k - (x_{n_p})_j \\ (y_{n_p})_k - (y_{n_p})_j \end{bmatrix} + \frac{m}{n_t} \begin{bmatrix} x_{\text{LOS},jk} \\ y_{\text{LOS},jk} \end{bmatrix} \tag{5.10}$$

$$x_{\text{test},jkm} \leq -(d_j + d_k) + M \, b_{\text{vis},1jkm} \tag{5.11}$$

$$y_{\text{test},jkm} \leq -(d_j + d_k) + M \, b_{\text{vis},2jkm} \tag{5.12}$$

$$x_{\text{test},jkm} \geq (d_j + d_k) - M \, b_{\text{vis},3jkm} \tag{5.13}$$

$$y_{\text{test},jkm} \geq (d_j + d_k) - M \, b_{\text{vis},4jkm} \tag{5.14}$$

$$\sum_{n=1}^{4} b_{\text{vis},njkm} \leq 3 \tag{5.15}$$

$$j = 1, \ldots, n_v - 1, \qquad k = j+1, \ldots, n_v, \qquad m = 1, \ldots, n_t$$

where n_t represents a number of test points placed between the planning horizon and the selected cost point to ensure the visibility in the relative frame [14]. Note that $\boldsymbol{x}_{\text{cp}}, \boldsymbol{x}_{\text{vis}}, \boldsymbol{x}_{\text{LOS}}, \boldsymbol{x}_{\text{test}}$ are in the relative frame whereas $\boldsymbol{x}_{n_p}$ is measured in the absolute frame. The cost function includes, together with the cost-to-go at the selected point, the length of the line-of-sight vectors in the absolute frame (denoted by l_i for the i^{th} vehicle) and relative frame (denoted

by $l_{\text{rel},jk}$ for a pair of vehicles j and k). Therefore, the objective J_2 to be minimized is

$$J_2 = \sum_{i=1}^{n_v} l_i + \sum_{j=1}^{n_v-1} \sum_{k=j+1}^{n_v} (\alpha\, l_{\text{rel},jk} + \beta\, c_{\text{vis},jk}) \tag{5.16}$$

$$l_i \geq \begin{bmatrix} x_{\text{goal},i} - (x_{n_p})_i \\ y_{\text{goal},i} - (y_{n_p})_i \end{bmatrix} \boldsymbol{i}_m \tag{5.17}$$

$$l_{\text{rel},jk} \geq \begin{bmatrix} x_{\text{LOS},jk} \\ y_{\text{LOS},jk} \end{bmatrix} \boldsymbol{i}_m \tag{5.18}$$

$$\boldsymbol{i}_m = \begin{bmatrix} \cos\left(\dfrac{2\pi m}{n_l}\right) \\ \sin\left(\dfrac{2\pi m}{n_l}\right) \end{bmatrix} \tag{5.19}$$

$$i = 1, \ldots, n_v, \qquad j = 1, \ldots, n_v - 1, \qquad k = j+1, \ldots, n_v, \qquad m = 1, \ldots, n_l$$

where α is a weighting factor for the line-of-sight vector in the relative frame, as defined in Eq. 5.9, and β is a weighting factor for the cost-to-go at the cost point in the relative frame. If the goal is not visible from the initial position in the relative frame, (*i.e.,* the paths of the two vehicles intersect in the absolute frame), the weights α and β navigate the vehicle to "hug" around the vehicle avoidance box, initiating the collision avoidance action. Larger α and β navigate the relative position towards the goal faster in the relative frame, but overly large weights delay the arrival at the goals in the absolute frame because the distances from the vehicles to their goals have a smaller effect on the objective function.

Note that if there are three vehicles involved, three relative positions (2–1, 3–2, 1–3) must be accounted for. However, this situation seldom happens because the typical UAVs operate with a large separation distance compared to their vehicle size.

This formulation is applied to the same scenario presented in Figure 5-26, and the result is shown in Figure 5-27. In contrast to Figure 5-26(a), vehicle 2 begins a collision avoidance maneuver immediately. Figure 5-27(b) shows that the relative trajectory successfully avoids the separation box, with some waypoints falling on the boundary.

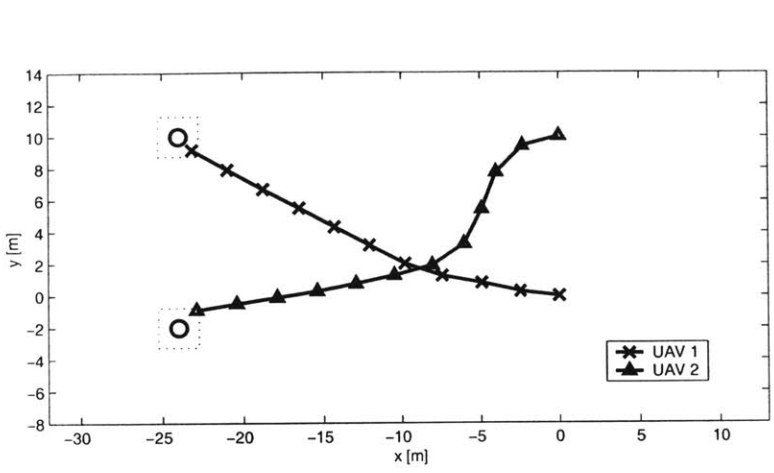

(a) Absolute position

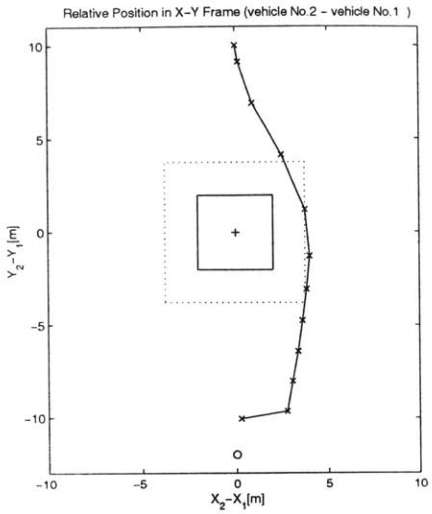

(b) Relative position

Figure 5-27: Collision avoidance maneuver with improved cost-to-go

Truck Experiments

The improved formulation for collision avoidance maneuver is experimentally tested using two trucks. In the single vehicle case shown in Subsection 5.3.2 and Subsection 5.4.1, a plan request is sent when the vehicle reaches the execution horizon, and the receding horizon controller re-optimizes the trajectory before the system reaches the end of the plan. In this two-truck case, a plan request is sent when either one of the vehicles reaches its horizon point. The speed controller in this experiment has a low bandwidth, and the MILP RHC controls the in-track position by adjusting the initial position of each plan, so that the vehicles reach waypoints at the right time. To see the effect of in-track adjustment by the RHC, three trials are conducted with different disturbances and control schemes:

Case–1: Small disturbance. No adjustment of in-track position.

Case–2: Small disturbance. Adjustment of in-track position by RHC.

Case–3: Large disturbance. Adjustment of in-track position by RHC.

The following parameters are used:

- $v\Delta t = 3.5$ [m]
- $v = 0.5$ [m/s]
- $r_{\min} = 5$ [m]
- $n_p = 4$
- $n_e = 1$
- Safety box for each truck: 0.8 [m] $\times$ 0.8 [m]

Figure 5-28(a) shows the planned waypoints of the first scenario. The two vehicles start in the upper right of the figure and go to the lower left while switching their relative positions. In Figure 5-28(b) and Figure 5-29, $\times$ marks represent the planned waypoints, and dots represent the position data reported from the trucks. The relative position starts in the lower right of Fig. (b) and goes to the upper left. Although the vehicles avoided a collision, the relative position deviates from the planned trajectory by as much as 1.8 m. This error is mainly caused by the ground roughness in the test area, which acts as a disturbance to the speed control loop, resulting in in-track position errors for both vehicles.

One way to improve this situation is to introduce an in-track position control loop in the low-level feedback controller. This requires the use of the time stamp placed by the planner at each waypoint. Another approach presented here is to feed the in-track error back into the receding horizon control loop. Figure 5-30 illustrates this procedure. Let $d_{//}$ denote the in-track distance to the next waypoint. When $d_{//}$ of either one of the vehicles becomes smaller than a threshold, the vehicle sends a plan request to the planner. If vehicle 2 is slower than vehicle 1, as is the case in Figure 5-30, the position difference in the in-track direction $(d_{//})_2 - (d_{//})_1$ is propagated to the initial position of vehicle 2 in the next plan. This propagation is accomplished by moving the next initial position backward by $(d_{//})_2 - (d_{//})_1$. Note that the truck positions are reported at 2 Hz, and an in-track distance $d_{//}$ at a specific time is obtained through an interpolation.

Figures 5-31 to 5-33 show the result of case–2, where the in-track position is propagated and fed back to the next initial condition by the RHC. The outcome of the in-track position adjustment is apparent in Figure 5-31(b) as the discontinuous plans. The lower right of Figure 5-31(b) is magnified and shown in Figure 5-32 with further explanation. When the

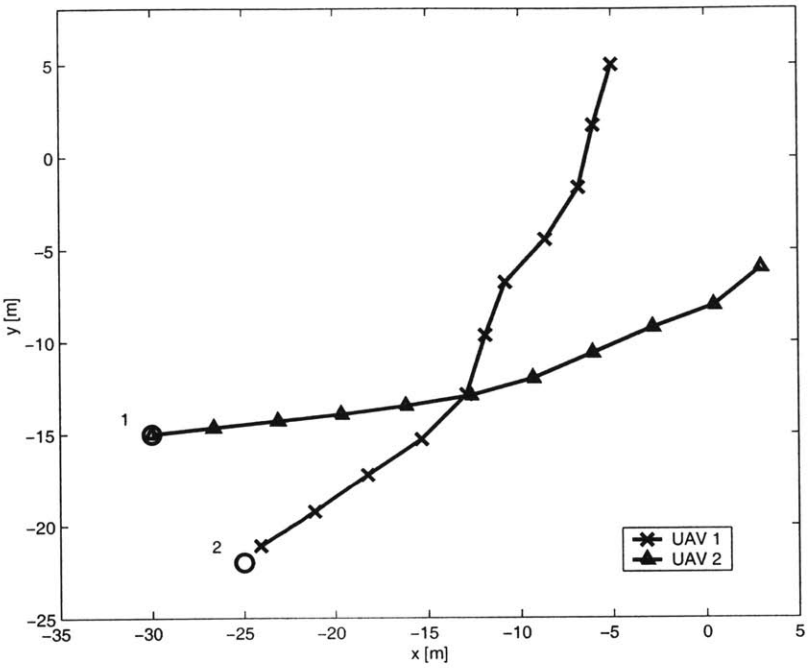

(a) Absolute position

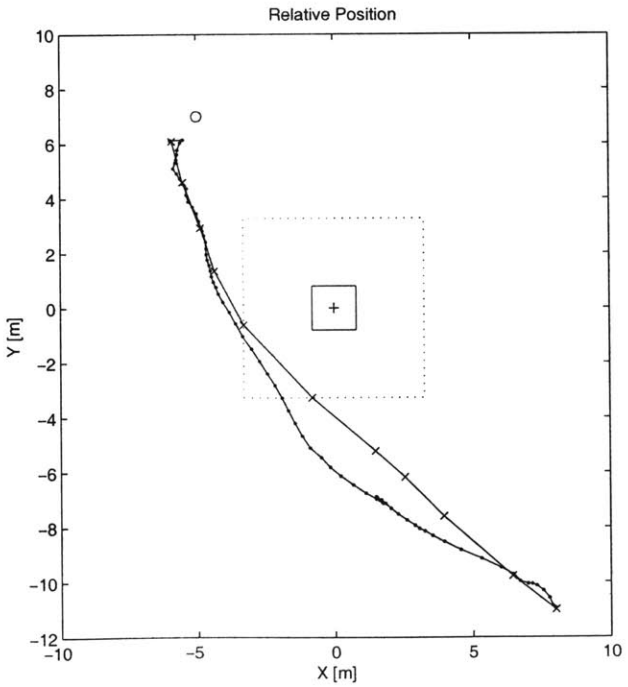

(b) Relative position

Figure 5-28: Case–1. Cost-to-go in relative frame, no adjustment of in-track position

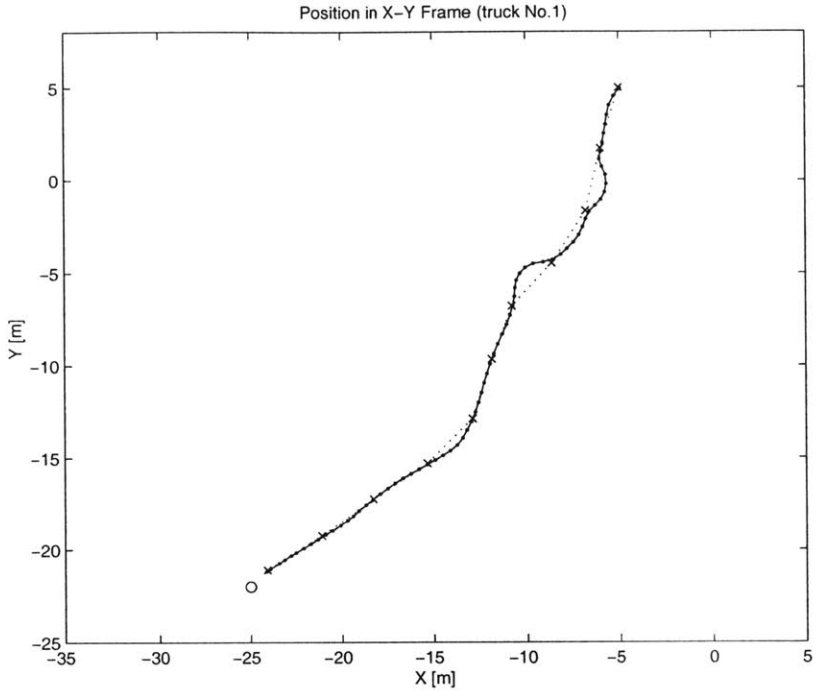

(a) Truck 1

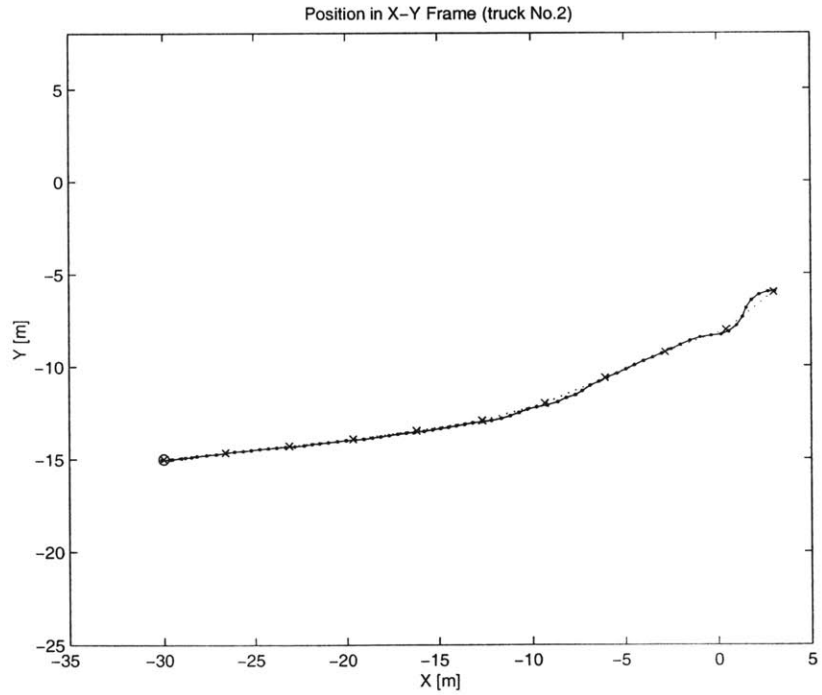

(b) Truck 2

Figure 5-29: Case–1. Cost-to-go in relative frame, no adjustment of in-track position. Actual position data in absolute frame is shown.

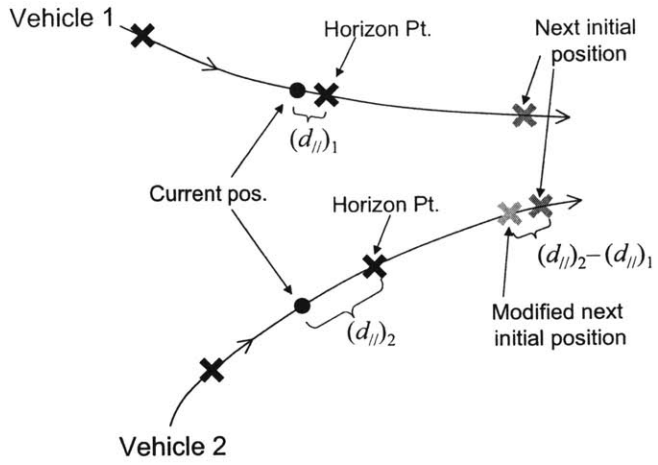

Figure 5-30: Adjustment of in-track position for the next optimization.

second plan request is sent, the difference between the planned relative position and the actual relative position is obtained (A), and is added as a correction term to the initial position of the next plan (A'). When the third plan request is sent, the difference at point B is fed back in the start position of the next plan (B'). This demonstrates that the replanning by the RHC can account for the relative position error of the two vehicles. Note that this feedback control by the RHC has a one-step delay, due to the computation time required by the MILP RHC. However, the computation time in this scenario is much smaller than the $\Delta t = 7$ [sec], and a much more frequent update is possible. Further research is being conducted to investigate this issue.

In case–3, a larger disturbance was manually added to truck 2. As shown in Figure 5-34, vehicle 2 goes behind vehicle 1 as opposed to the results of case–2 shown in Figure 5-31. This demonstrates the decision change by the RHC in an environment with strong disturbances. Further observations include: replanning by the RHC was able to correct the relative position errors; overly large disturbances can make the MILP problem infeasible; improvements of the current control scheme, which has a one step delay, will enable a further detailed timing control; similar performance could be achieved by updating the reference speed of the low-level PI speed controller. Future experiments will compare these two approaches.

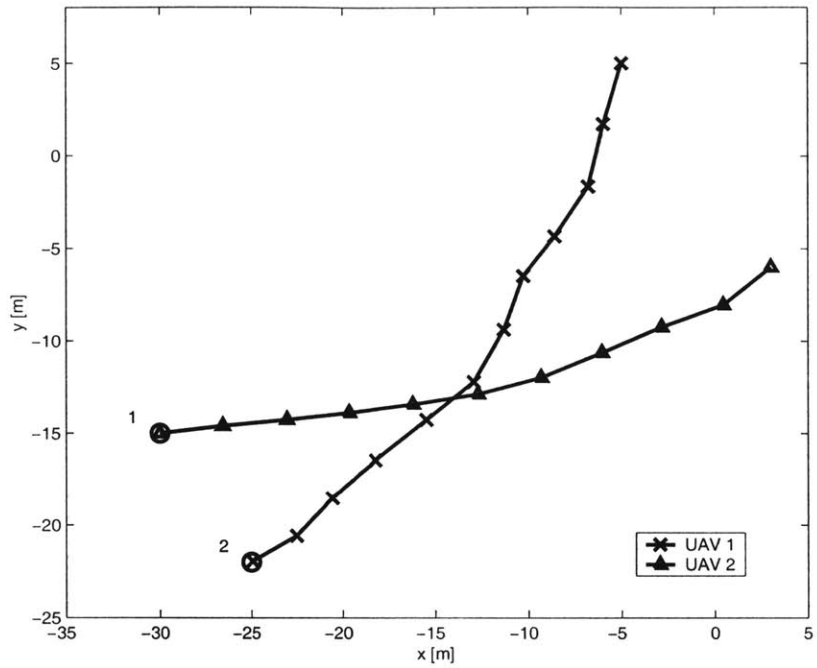

(a) Absolute position

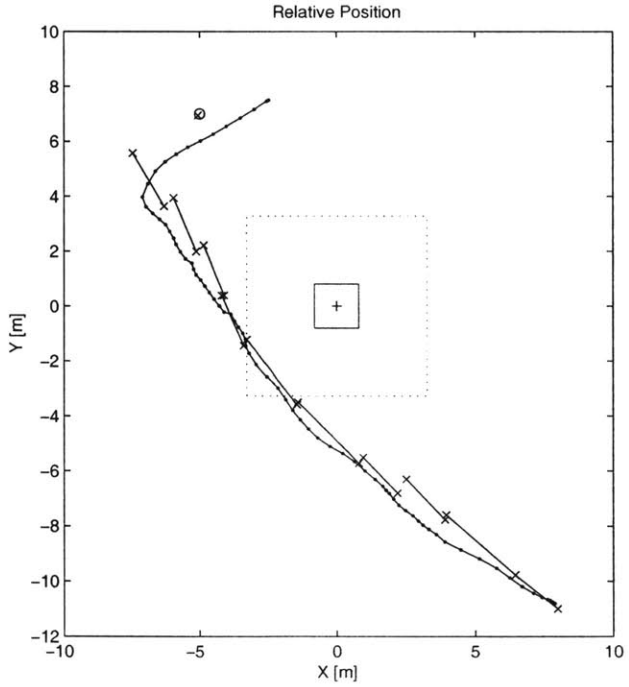

(b) Relative position

Figure 5-31: Case–2. Cost-to-go in relative frame, with adjustment of in-track position

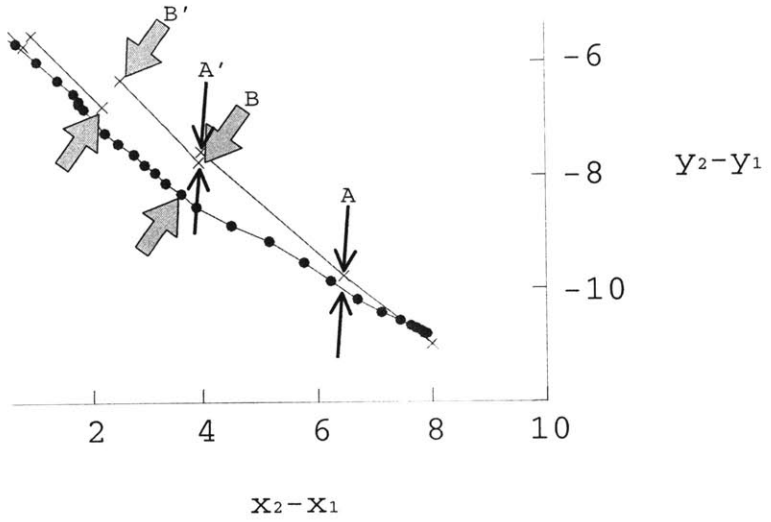

Figure 5-32: Close-up of lower right corner of Figure 5-31(b). The position difference between the planned waypoint and the actual relative position (A) is fed back to the next initial position (A'). When the next initial position is reached, the position difference (B) is fed back such that the next-next start position is modified (B').

5.5 On-Line Task Reassignment

In the previous sections, the receding horizon controller generates a detailed trajectory (a list of waypoints) for each vehicle given a list of goals. In a multiple vehicle case, however, a change in the environment such as the discovery of new targets and/or the pop-up of an obstacle requires a re-allocation of the tasks amongst the fleet of vehicles to accomplish the overall mission more effectively. This re-allocation corresponds to the fourth control loop shown in Figure 5-1. The control scheme presented on p.112 is enhanced as follows:

1. If there is a change in the situation awareness due to the detection of an unknown obstacle or the identification of new targets (*or if starting*): compute the cost map and reassign (*or assign if starting*) tasks among the vehicles.
2. Solve MILP minimizing J in Eq. 2.56 subject to Eqs. 2.2 to 2.57, starting from the last waypoint uploaded (*or initial state if starting*).
3. Upload the first n_e waypoints of the new plan to the vehicle.

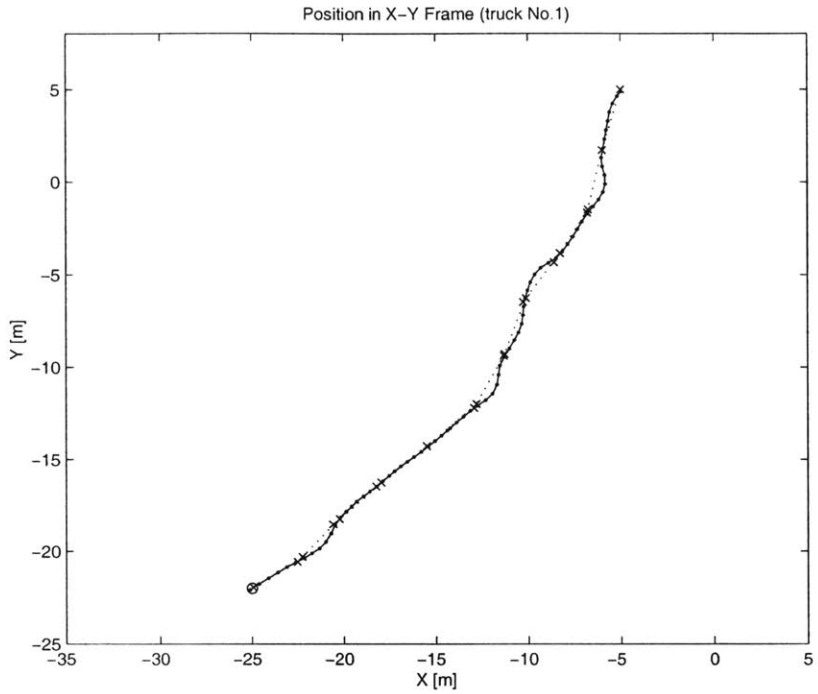

(a) Vehicle 1

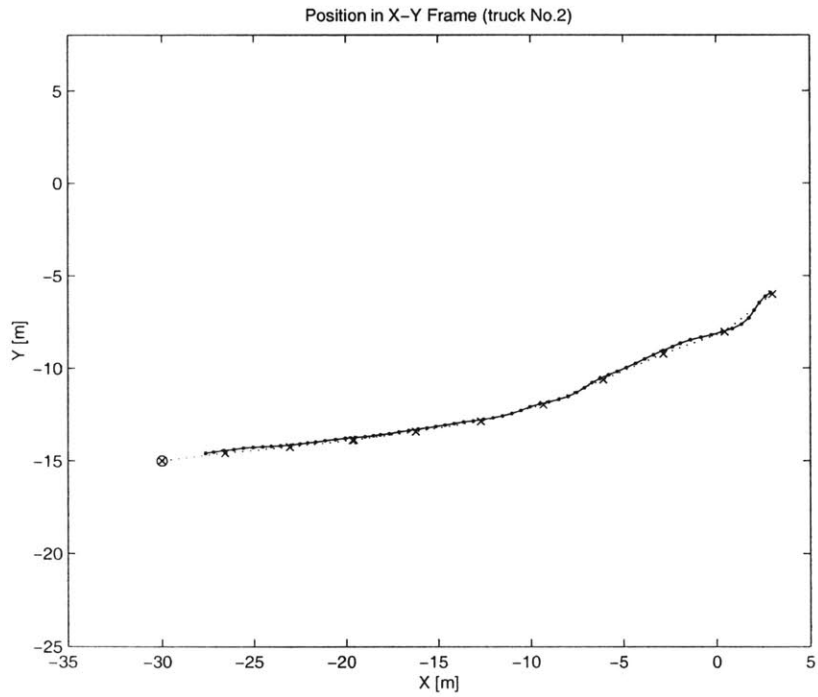

(b) Vehicle 2

Figure 5-33: Case–2. Cost-to-go in relative frame, with adjustment of in-track position. Actual position data in absolute frame is shown.

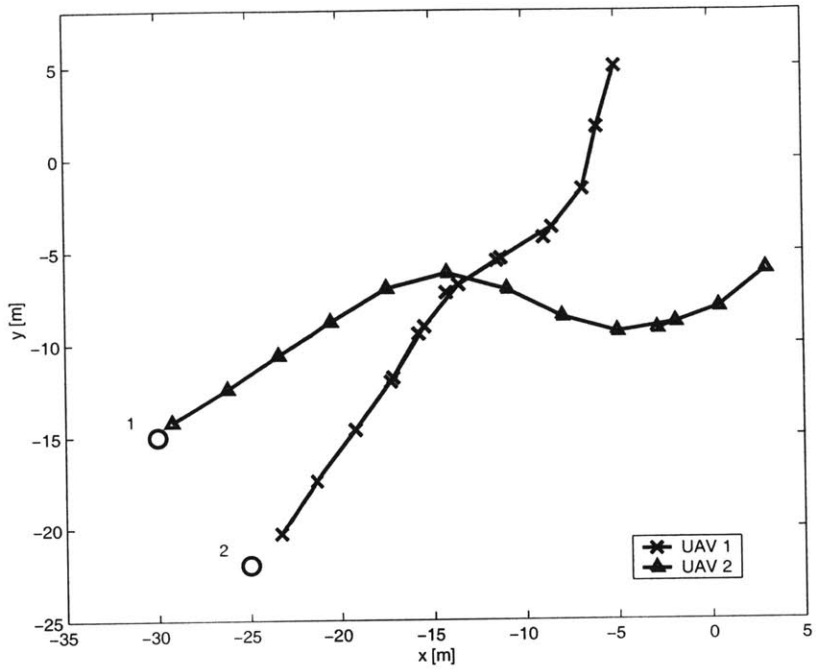

(a) Absolute position

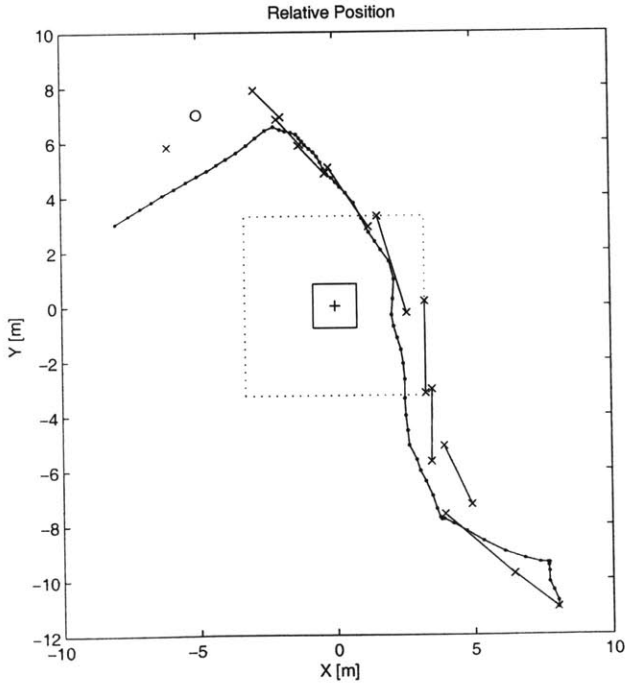

(b) Relative position

Fig. 5-34: Case–3. Cost-to-go in relative frame, with adjustment of in-track position. Large disturbance has been added. The square in solid lines is an actual vehicle avoidance box, and the square in dashed lines is an expanded safety box. The vehicle avoidance box is expanded to account for the time discretization, as illustrated in Figure 2-6.

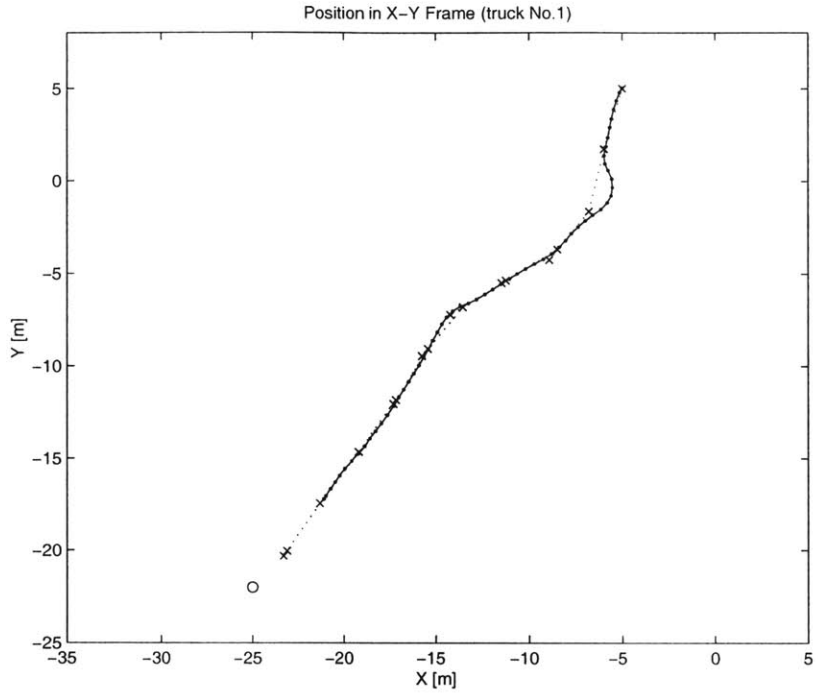

(a) Vehicle 1

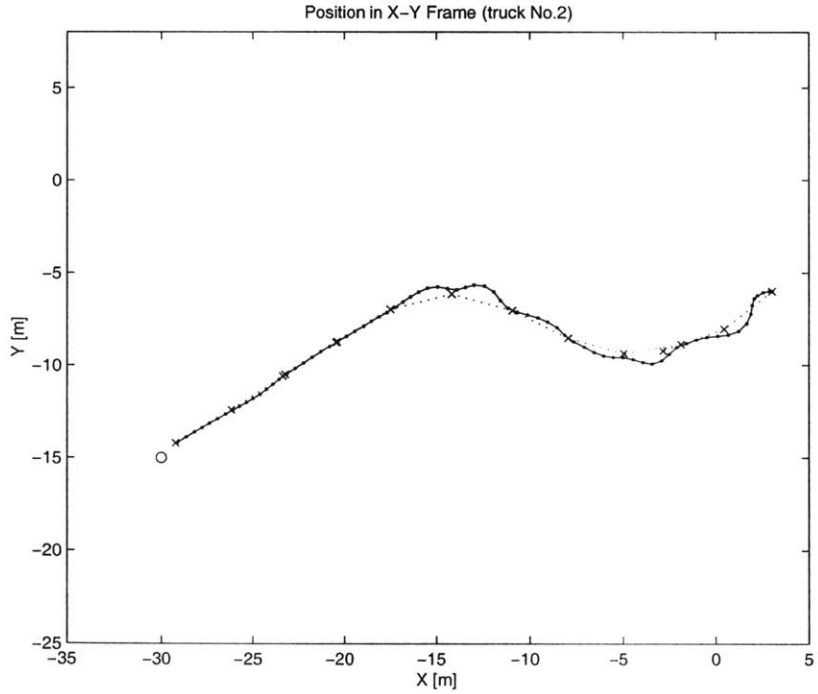

(b) Vehicle 2

Figure 5-35: Case–3. Cost-to-go in relative frame, with adjustment of in-track position. Actual position data in absolute frame is shown.

4. Wait until one of the vehicles reaches the execution horizon of the previous plan.
5. Go to 1.

5.5.1 Scenario Description

This section describes a scenario that requires coordination of three vehicles. This scenario was tested on the autopilot testbed described in Subsection 5.5.2. There are three targets of two types: two high-value targets (HVTs) and one low-value target (LVT). The HVT requires reconnaissance before a strike, and damage assessment must follow the strike. If the strike is unsuccessful, it requires another strike. The LVT requires only a strike. Timing constraints in the task assignment phase are necessary: reconnaissance must occur before the strike and the assessment must occur after the strike. The human operators or higher level planners could also add extra timing constraints as mission requirements, such as requiring that the HVT must be visited before the LVT.

There are three UAVs of two types: one reconnaissance vehicle and two combat vehicles. The role of the reconnaissance vehicle is to identify the exact location of the HVTs, and do the bomb damage assessment (BDA) after the strike. The role of the combat vehicles is to strike either the HVT or LVT.

Figure 5-36 shows the target locations (○), vehicle initial locations (□), and obstacles (distances are in meters). The thin obstacle at $[x_l, y_l, x_u, y_u] = [-1300, -850, -500, -800]$ is not initially known. The location of the obstacle could be identified by any of the vehicles. The three vehicles are assumed to have the same situational awareness, and once a vehicle updates information on the environment, it is shared by all the vehicles. There is a centralized planner that makes the plans for all three vehicles with one global cost map.

Table 5.1 explains the indices associated with the targets. HVTs must be visited at least three times for reconnaissance, strike, and BDA. For this reason, more than one point is put at the same location to pose a task assignment problem in the MILP form (see p.80). Vehicles 1 and 2 are the combat vehicles, and are able to visit HVT A (labelled 1-4), HVT B (labelled 5-8), and LVT (labelled 9). Vehicle 3 can visit HVT A and HVT B only for the

Table 5.1: Types of each target.

index	Name	Description	Vehicle capability
1	HVT A	Reconnaissance (assumed location)	3
2	HVT A	Strike (assumed location)	1, 2
3	HVT A	Strike (actual location)	1, 2
4	HVT A	BDA (actual location)	3
5	HVT B	Reconnaissance (assumed location)	3
6	HVT B	Strike (assumed location)	1, 2
7	HVT B	Strike (actual location)	1, 2
8	HVT B	BDA (actual location)	3
9	LVT	low value target	1, 2
10	Base	base area	1
11	Base	base area	2
12	Base	base area	3

Table 5.2: Timing constraints for the scenario.

Description	Pair (i, j)
HVT first, LVT next	(2,9), (3,9), (6,9), (7,9)
HVT A first, then HVT B	(1,5), (4,8), (3,7)
Base last (Vehicle 1)	(2,10), (3,10), (6,10), (7,10), (9,10)
Base last (Vehicle 2)	(2,11), (3,11), (6,11), (7,11), (9,11)
Base last (Vehicle 3)	(1,12), (4,12), (5,12), (8,12)
Reconnaissance, then BDA	(1,4), (5,8)
Strike, then BDA	(3,4), (7,8)
Reconnaissance, then Strike	(1,2), (5,6)

purposes of reconnaissance and BDA. In the reconnaissance mission, vehicle 3 updates the actual locations of HVT A and HVT B from the original predictions.

Time dependencies between the waypoints are summarized in Table 5.2. A pair (i, j) represents a timing constraint $TOA_i \leq TOA_j$. Some of the timing constraints can be deduced by a higher-level planner [38] (*e.g.*, base station must be visited last after visiting all the targets), and the others can be imposed by the mission operator (*e.g.*, HVT A has a higher priority than HVT B).

Note that each waypoint can take three states: unknown, known but unvisited, and visited. Only the waypoints that are known and unvisited are used in the MILP task assignment

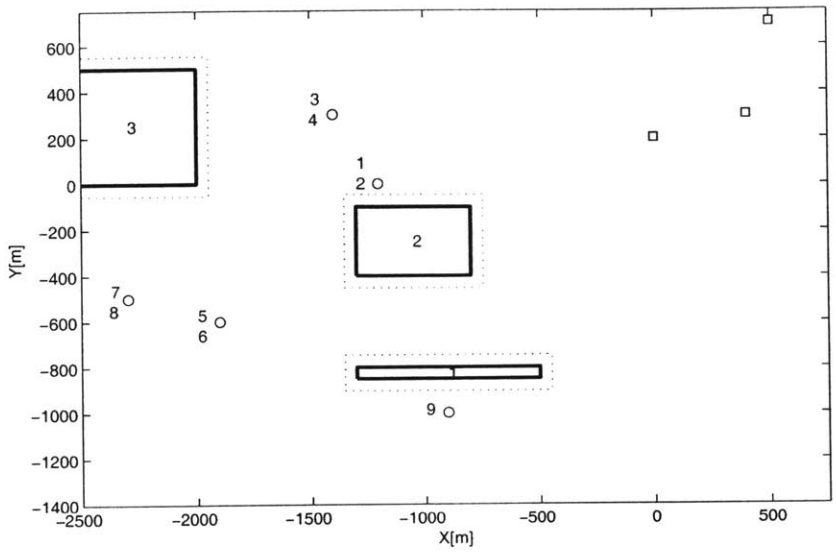

Figure 5-36: Scenario with tightly coupled tasks

algorithm.

5.5.2 Demonstration

As discussed in Section 5.1, a number of assumptions must hold in order to close all the control loops. Another objective of this demonstration is a verification of the vehicle dynamics model that has been used in the simulation. Three types of scenarios with dynamic/stochastic events are used in the hardware-in-the-loop simulations using the autopilots described in Section 5.2.3:

Scenario 1. Sudden detection of the obstacle which changes the assignment of tasks;

Scenario 2. Unsuccessful strike of HVT A identified by the BDA mission;

Scenario 3. Sudden loss of a combat vehicle.

The following parameters refer to the actual vehicle characteristics. The nominal speed of 20 [m/s] is based on the specification of our aircraft PT40 shown in Figure 5-10. A step size of 150 [m] and the minimum turning radius of 200 [m] were determined such that the waypoint following controller gives a smooth response for the time constants of this vehicle. The minimum separation distance between the obstacles was assumed to be larger than

$r_{\min}$ such that the planning horizon of three steps guarantees the stability of the RHC. The execution horizon is one step.

Figures 5-37 to 5-40 show the entire trajectory of three UAVs in the first scenario. In Figure 5-40, $\times$ marks show the planned waypoints, and $\bullet$ marks show the flight data obtained through hardware-in-the-loop simulation.

At the start of this demonstration, the three vehicles wait in a loiter circle. They then enter the picture from the upper right. Vehicle 3 reaches HVT A first, only to find its actual location is different from the assumed position by 360 [m] (Figure 5-37). Vehicle 1, which is assigned to strike HVT A, then changes its path to HVT A. Before vehicle 2 visits HVT B, vehicle 3 updates its location (Figure 5-38), and thus vehicle 2 also changes its heading. After completing the mission at HVT A, vehicle 1 aims for the LVT at location $[-900 - 1000]^T$. However, vehicle 1 then detects an unknown obstacle (Figure 5-39), which makes the path of vehicle 1 to the LVT significantly longer. Thus, it is better to assign vehicle 2 to the LVT instead of vehicle 1, and vehicle 1 returns to the base area (located to the middle right of the figure). Note that this sequence assumes that complete knowledge of the obstacle is available as soon as part of it is detected. Vehicle 3 visits the actual target locations of HVT A and HVT B to assess the strike missions conducted by the two combat vehicles. This example demonstrates the on-line task reassignment due to a dynamic change in the situational awareness, such as obstacle detection. It also shows the coordinated mission accomplished by the three vehicles with different capabilities. The flight data and the planned waypoints verifies the validity of the vehicle dynamics model discussed in Chapter 2.

In scenario 2, everything is the same as in scenario 1 until vehicle 3 discovers the unsuccessful strike of the HVT A (Figure 5-41). Vehicle 1, which is on its way to the base, is then assigned to re-strike HVT A. Vehicle 3 does the BDA after the re-strike, and confirms that the second strike is successful (Figure 5-42). The full set of trajectories for each vehicle is shown in Figure 5-43.

In scenario 3, vehicle 2 suddenly gets lost on its way to the LVT (Figure 5-44). Vehicle 1, which is the only combat UAV left, has to go back to visit the LVT (Figure 5-45). Scenarios 2

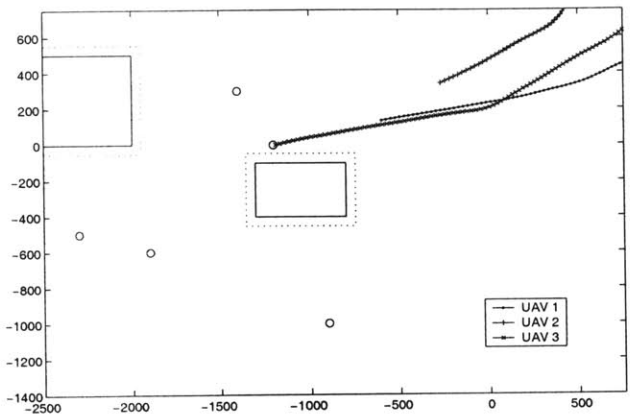

Figure 5-37: Scenario 1: Vehicle 3 updates the position of HVT A

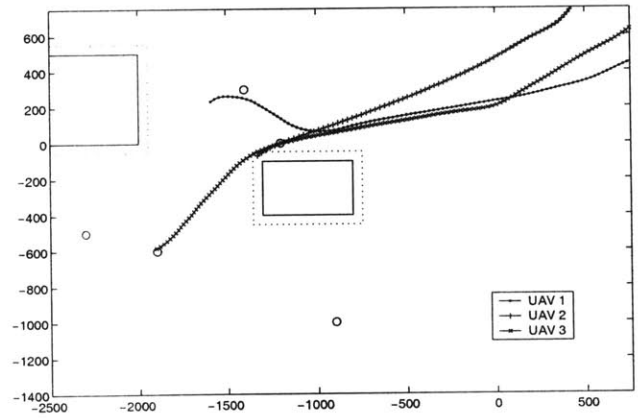

Figure 5-38: Scenario 1: Vehicle 3 updates the position of HVT B

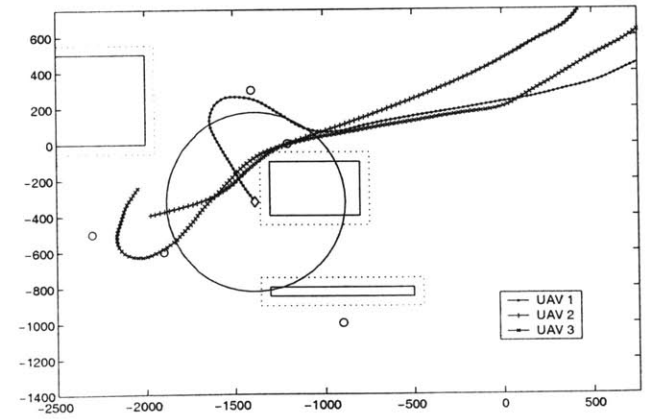

Figure 5-39: Scenario 1: Vehicle 1 detects a new obstacle. Circle in the center shows the detection range of vehicle 1.

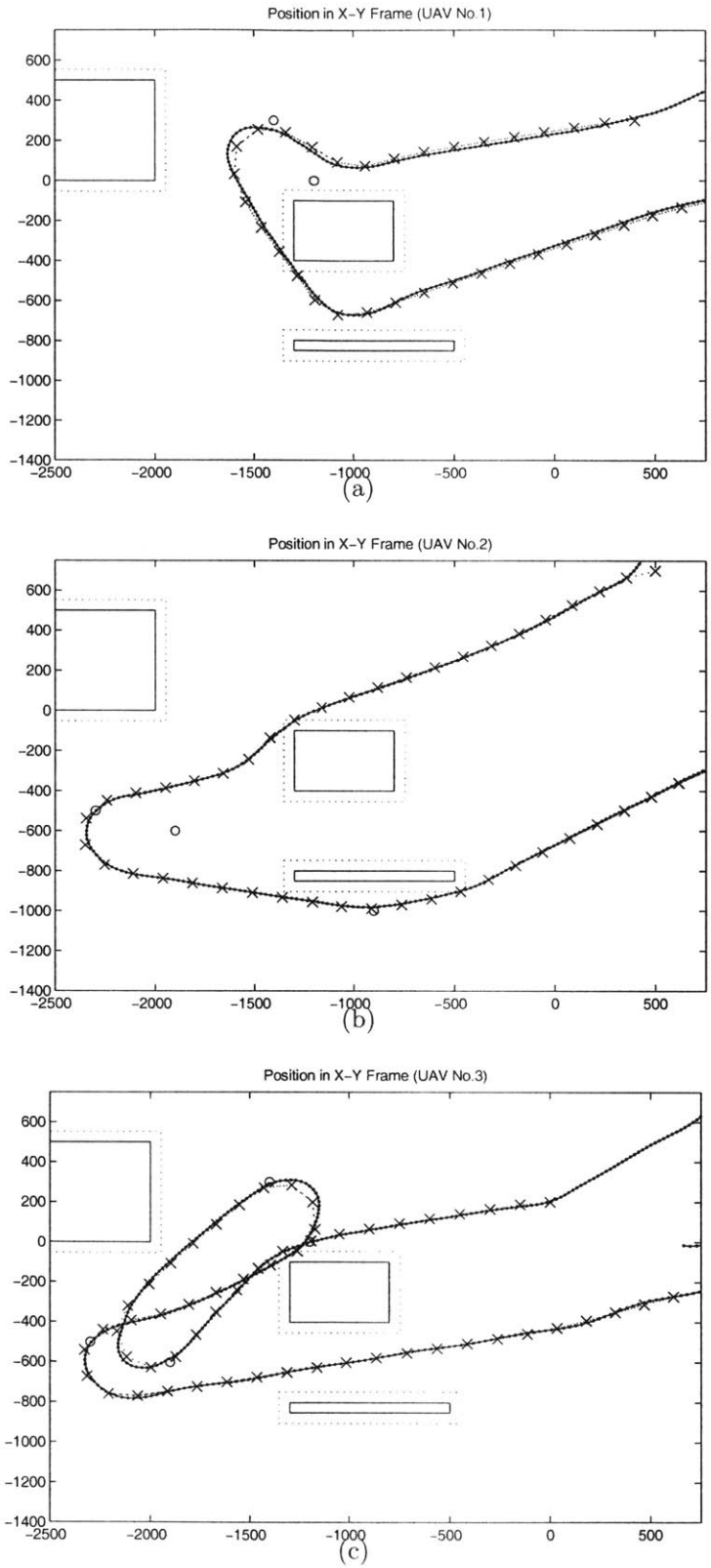

Figure 5-40: Planned waypoints and actual UAV trajectories for Scenario 1

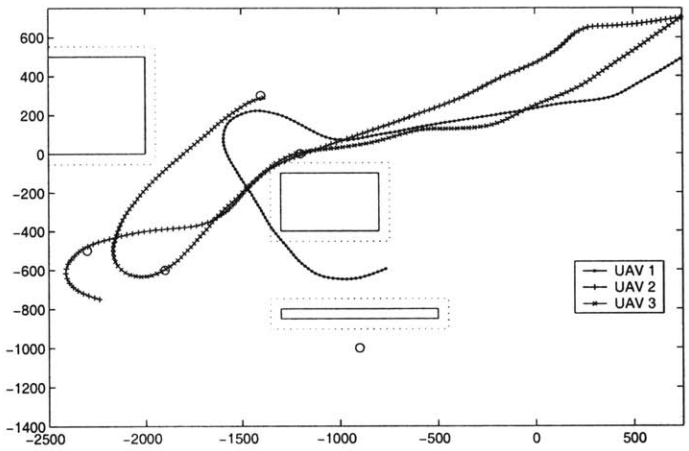

Figure 5-41: Scenario 2: Vehicle 3 discovers that strike on HVT A is unsuccessful

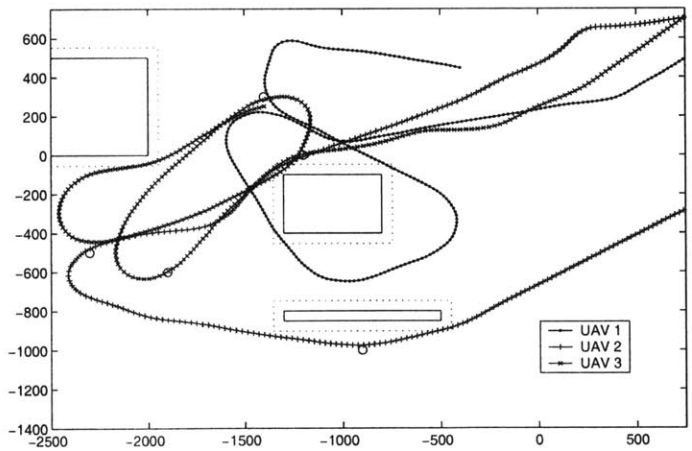

Figure 5-42: Scenario 2: Vehicle 3 assesses HVT A again

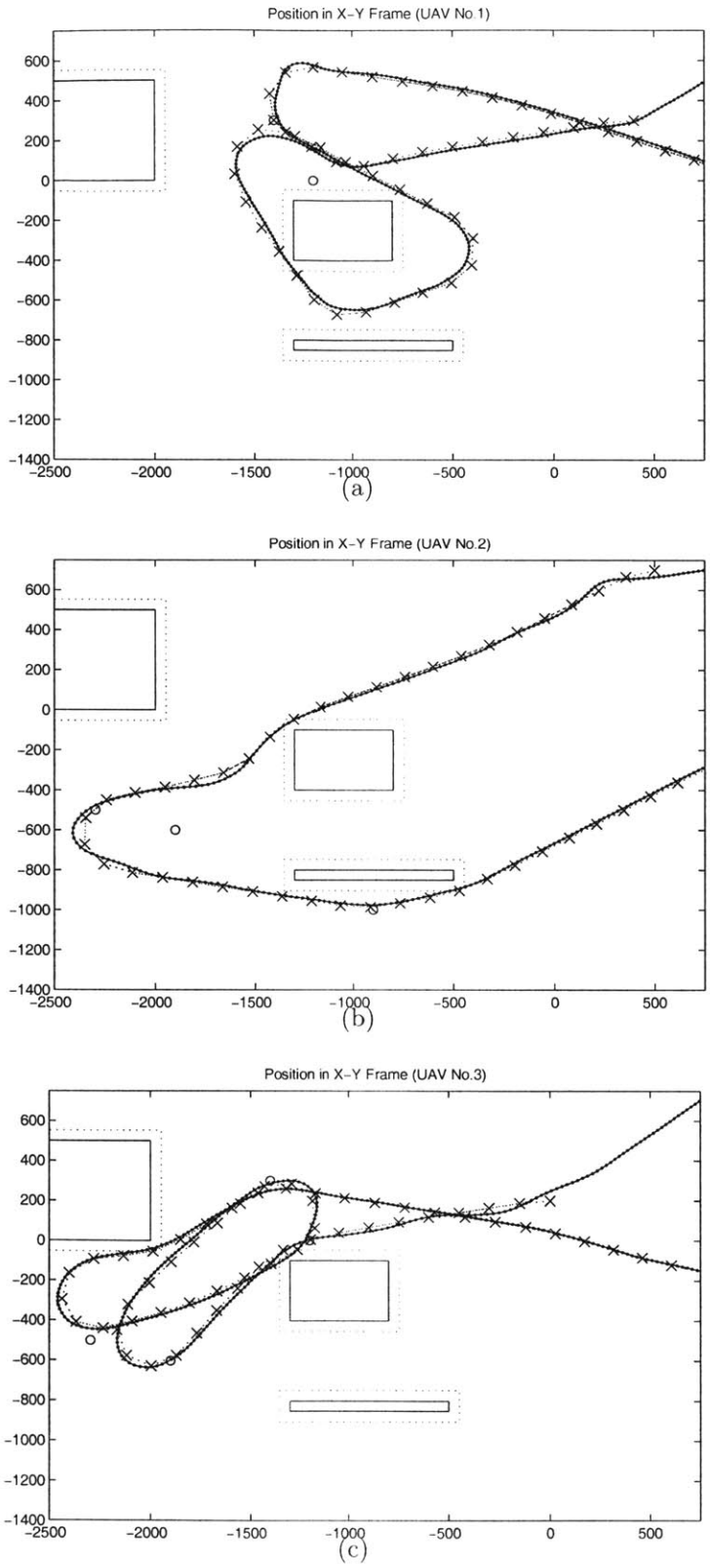

Figure 5-43: Planned waypoints and actual UAV trajectories for Scenario 2

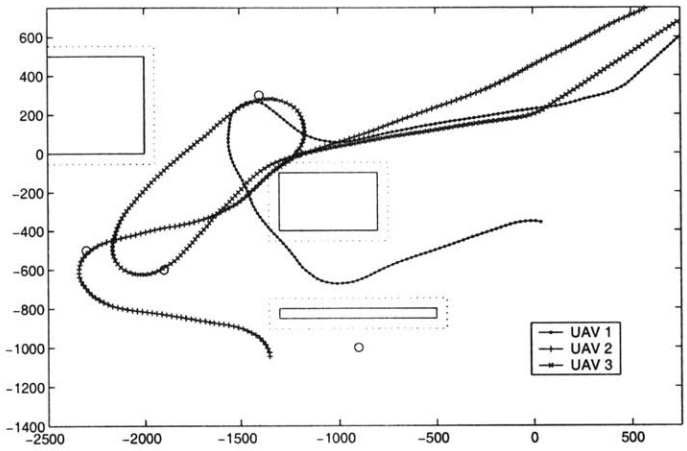

Figure 5-44: Scenario 3: Sudden loss of vehicle 2

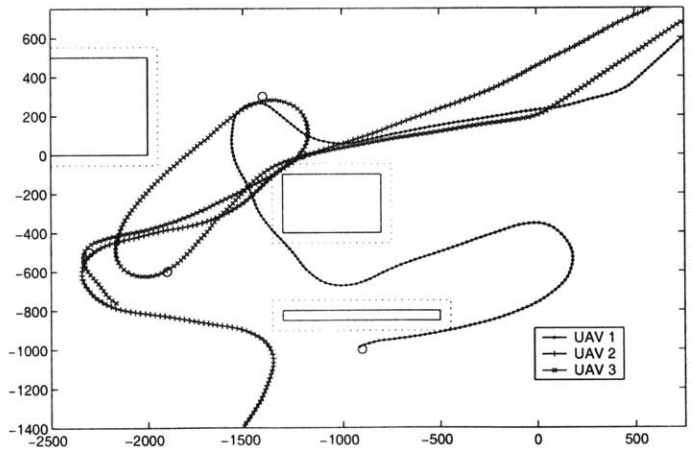

Figure 5-45: Scenario 3: Vehicle 1 comes all the way back

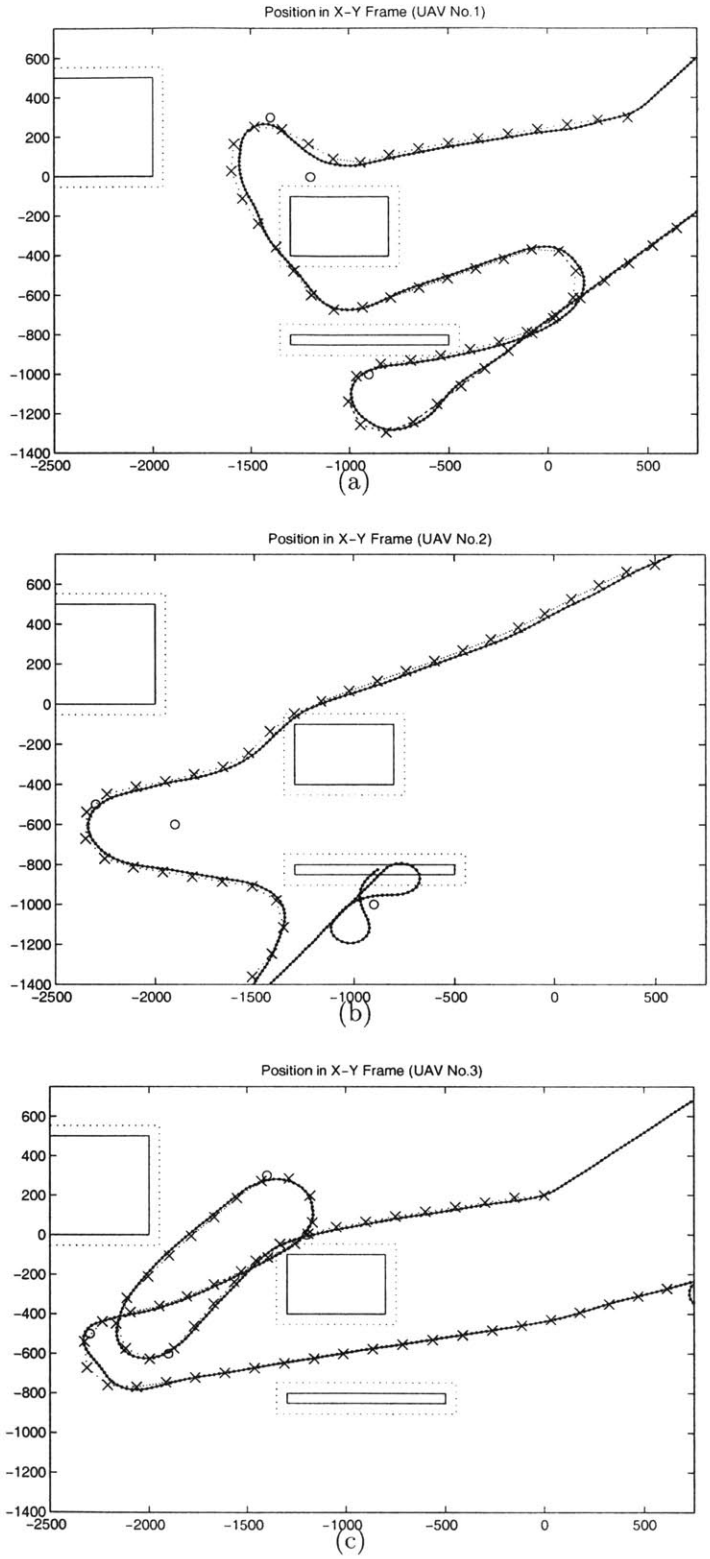

Figure 5-46: Planned waypoints and actual UAV trajectories for Scenario 3. The vehicle 2 is lost at the bottom of the figure (b), and the rest of the maneuver does not have any meanings.

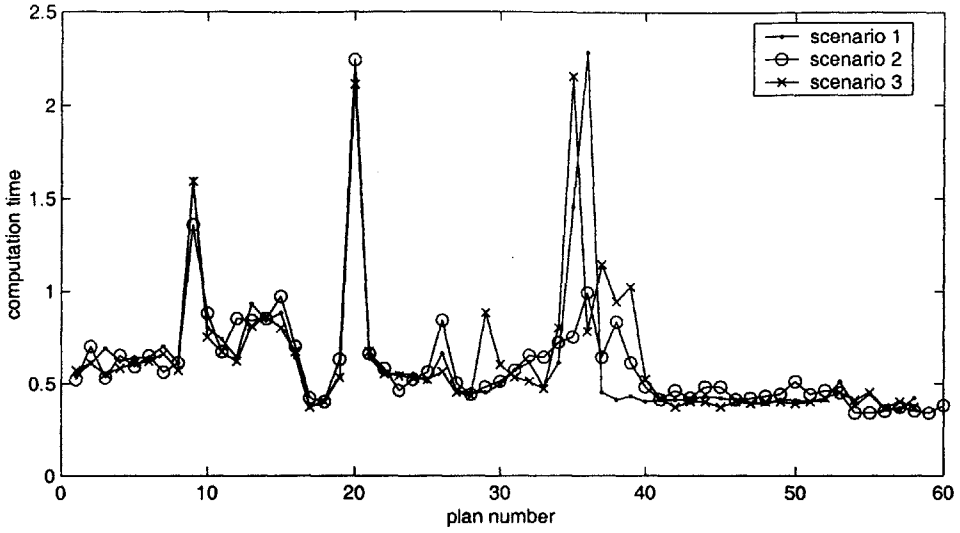

Figure 5-47: Computation time of each plan for the three scenarios

and 3 demonstrate how the tasks are properly reassigned among a fleet of vehicles after unexpected stochastic events.

The computation time for these three scenarios are shown in Figure 5-47. It is the time it took for the planner to generate detailed trajectories for all three vehicles after receiving a plan request. This includes: an update of the cost map if there is a change in the situational awareness; a task assignment if the reassignment is necessary; and generation of trajectories by the RHC. Peaks tend to appear when large changes in the environment require re-calculation of the overall process. For example, just before generating the ninth plan, the location of HVT A is updated, which results in a task reassignment and tight turn for vehicle 1. For plan number 20, the pop-up obstacle changes the entire cost map, which, again, results in a task reassignment and vehicle 1 is forced to make a sharp turn to avoid the obstacle. The peak represented by plan number 36 in scenario 1 is caused by hard turns made by vehicles 1 and 3. Vehicle 1 has to re-visit HVT A from the right, and then heads towards the base, which is also to the right of the figure. Vehicle 3, heading towards the lower left of the figure to visit HVT B for the BDA mission, needs to change its heading by 180 degrees to re-visit HVT A to accomplish the second BDA mission. The peak represented by plan number 35 in scenario 3 is caused by vehicle loss. Note that all of

the computation times are well below the discrete time step of $n_e \Delta t = 7.5$ [sec], and that the real-time trajectory generation for a fleet of vehicles in these three different scenarios is successful.

5.6 Conclusions

Several experiments have have been presented to demonstrate the use of MILP for on-line replanning to control vehicles in the presence of dynamic uncertainties. Four different levels of control loops have been implemented on a ground vehicle testbed and a UAV hardware-in-the-loop simulator testbed to demonstrate technologies developed for future UAV control. The first example validated the on-line trajectory generation using the RHC. This architecture uses MILP for high-level path-planning, while a low-level feedback loop onboard the vehicle tracks the desired waypoints and rejects disturbances. In one example, a receding horizon formulation successfully maneuvered a vehicle to its assigned goal with a restricted detection of obstacles, representing a limited-range radar. In the collision avoidance maneuver, the high-level RHC path planner can account for differences in the time-of-arrival between two vehicles. The approach uses a feedback correction in the RHC with a one time-step delay, and on-going research is investigating more reactive techniques. The last example showed the tight coordination of a fleet of three autonomous vehicles. It also demonstrated the task re-assignment due to the dynamic and/or stochastic events coupled with a re-design of trajectory. A faster task re-assignment algorithm will be required when more tasks are being assigned to larger fleets.

Chapter 6

Conclusions and Future Work

6.1 Contributions

This thesis presented a real-time trajectory generation method using a receding horizon control and demonstrated its hardware implementation on two different types of testbeds. In particular, the following list shows the primary contributions of this thesis:

- Rigorous formulation of the MILP receding horizon trajectory optimization problem that includes multiple vehicles and multiple goal scenarios.
- An improved formulation of the stable receding horizon controller that guarantees finite time completion of the mission in a constrained environment.
- Reduction of the computation time of the MILP RHC using a new pruning algorithm.
- Extension of the task allocation problem to scenarios with highly coupled tasks and relative timing constraints.
- Integration of the control algorithms acting on four different levels of the hierarchy in Figure 1-1.
- Demonstration of these planning algorithms in a real environment with disturbances, communication delays, and finite computational power.

Chapter 2 presented the complete receding horizon trajectory design problem in the MILP form. The binary variables in MILP express the logical constraints such as the goal selection,

the path selection, and the collision avoidance. This formulation allows for longer missions with several tasks because the trajectory is continually generated over a limited range into the future (*i.e.*, the planning horizon).

The discussion in Chapter 3 bridged the gap between the two models used in the RHC: the coarse model using the straight line approximation and the detailed model using the point mass vehicle dynamics. By considering the turning circles at the cost estimation phase, the path planned based on the straight lines guarantees the existence of a feasible solution during the MILP trajectory optimization phase. The node elimination and the modified Dijkstra's algorithm presented in this chapter allow "unstable" nodes to be pruned without losing the key candidate options for the optimal path. This pruning also significantly reduces the computation time.

Chapter 4 presented a task assignment algorithm that can be applied to complicated scenarios with various time dependencies. Adding the option of loitering as an extra degree of freedom enables the MILP to find an optimal solution to sophisticated missions, involving simultaneous arrivals or ordered tasks.

In Chapter 5, the planning algorithms have been demonstrated on two different types of testbeds. In the real world, disturbances act on the vehicle and its behavior can be different from what is planned. In an uncertain environment, a change in the situational awareness might make the existing plan obsolete, and the result of a stochastic event might require a change in the entire approach to the mission. Chapter 5 demonstrated that replanning at the various levels of the control hierarchy can be used to compensate for these different types of uncertainties. Several experiments were conducted to demonstrate the real-time control loop closures. These included the low-level feedback control, the graph-based path planning, the MILP based RHC trajectory generation, and the task reassignment among three heterogeneous vehicles. The experimental results showed that closing the various loops led to successful mission completion despite the action of disturbances. In addition, the experimental results indicate that the various assumptions made in the planning/simulations were valid.

6.2 Future Research Directions

While the scenarios examined in this thesis demonstrated the real-time trajectory generation for reasonably sized problems, a further increase in the size of the problem will lead to a computational issue for MILP or other non-convex optimization techniques. The computational issue mainly consists of the following three parts, and further future research will be required to develop algorithms to overcome them.

First, the problem size increases as the number of vehicles increases. The centralized planner presented in this thesis will eventually be unable to handle an overly large problem. However, the MILP trajectory design optimization can be conducted separately for each vehicle, as mentioned in Chapter 2, if the inter-vehicle collision is not an issue. This motivates implementing the trajectory design in a distributed architecture, and then using the pair-wise collision avoidance in Subsection 5.4.2 to avoid collisions.

Second, as the number of obstacles increases, the number of binary variables also increases, which leads to a rapid growth in the computation time. As discussed in Chapter 3, a pruning algorithm before the MILP optimization phase can significantly reduce the possible options while keeping the primary candidates for the best solution. Further improvement in the lower bound of the planning horizon might be possible, which reduces an area where detailed trajectory needs to be designed.

Third, on-line task reassignment has a large impact on the rate of the planning loop, as shown in Section 5.5. The computational demands of the task allocation are known to increase when additional or highly complicated tasks must be allocated. It is very difficult to solve large allocation problems using the exact or approximate decomposition methods using MILP. However, heuristic algorithms such as Tabu search [39] provide good solutions in a reasonable computation time for large problems. Using heuristics to predict the far future while solving the exact allocation problem in the near term using MILP should also enable task assignment in a receding horizon fashion.

Overall, the MILP RHC plays an important role in real-time trajectory generation and execution. In order to enhance the variety and flexibility of mission goals, however, tighter

integration with other algorithms such as temporal planning, low-observability technology, and stochastic programming needs to be explored.

Bibliography

[1] P. R. Chandler, M. Pachter, D. Swaroop, J. M. Fowler, J. K. Howlett, S. Rasmussen, C. Schumacher, and K. Nygard, "Complexity in UAV Cooperative Control," in *Proceedings of the American Control Conference*, (Anchorage AK), May 2002.

[2] C. Schumacher, P. R. Chandler, and S. Rasmussen, "Task Allocation for Wide Area Search Munitions via Network Flow Optimization," in *Proceedings of the American Control Conference*, (Anchorage AK), pp. 1917–1922, May 2002.

[3] J. Bellingham, M. Tillerson, A. Richards, and J. How, "Multi-Task Allocation and Path Planning for Cooperating UAVs," in *Second Annual Conference on Cooperative Control and Optimization*, Nov 2001.

[4] A. Richards, J. Bellingham, M. Tillerson, and J. How, "Coordination and Control of Multiple UAVs," in *Proceedings of the AIAA Guidance, Navigation and Control Conference*, (Monterey, CA), Aug 2002.

[5] J. C. Latombe, *Robot Motion Planning.* Kluwer Academic, 1991.

[6] P. R. Chandler and M. Pachter, "Research Issues in Autonomous Control of Tactical UAVs," in *Proceedings of the American Control Conference*, (Washington, DC), pp. 394–398, 1998.

[7] A. G. Richards, "Trajectory Optimization using Mixed-Integer Linear Programming," Master's thesis, Massachusetts Institute of Technology, June 2002.

[8] A. Richards, T. Schouwenaars, J. How, and E. Feron, "Spacecraft Trajectory Planning With Collision and Plume Avoidance Using Mixed-Integer Linear Programming," *Journal of Guidance, Control and Dynamics*, vol. 25, pp. 755–764, Aug 2002.

[9] A. Richards and J. P. How, "Aircraft Trajectory Planning With Collision Avoidance Using Mixed Integer Linear Programming," in *Proceedings of the American Control Conference*, (Anchorage, AK), May 2002.

[10] R. Fourer, D. Gay, and B. Kernighan, *AMPL: A Modelling Language for Mathematical Programming.* Danvers, MA: Boyd and Fraser Publishing Company, 1993.

[11] ILOG, *ILOG CPLEX User's guide*, 1999.

[12] A. Bemporad and M. Morari, "Control of systems integrating logic, dynamics, and constraints," *Automatica*, vol. 35, pp. 407–427, 1999.

[13] J. Bellingham, A. Richards, and J. How, "Receding Horizon Control of Autonomous Aerial Vehicles," in *Proceedings of the American Control Conference*, May 2002.

[14] J. S. Bellingham, "Coordination and Control of UAV Fleets using Mixed-Integer Linear Programming," Master's thesis, Massachusetts Institute of Technology, 2002.

[15] J. Bellingham, Y. Kuwata, and J. How, "Stable Receding Horizon Trajectory Control for Complex Environments." To appear at Proceedings of the American Control Conference, 2003.

[16] J. M. Maciejowski, *Predictive Control with Constraints.* Prentice Hall, 2002.

[17] M. B. Milam, K. Mushambi, and R. M. Murray, " New Computational Approach to Real-Time Trajectory Generation for Constrained Mechanical Systems," in *Proceedings of the IEEE Conference on Decision and Control*, (Washington DC), pp. 845–851, 2000.

[18] R. Franz, M. Milam, , and J. Hauser, "Applied Receding Horizon Control of the Caltech Ducted Fan," in *Proceedings of the American Control Conference*, 2002.

[19] C. Schumacher, P. R. Chandler, and S. Rasmussen, "Task Allocation for Wide Area Search Munitions via Network Flow Optimization," in *Proceedings of the AIAA Guidance, Navigation and Control Conference*, (Montreal, Canada), August 2001.

[20] M. Moser, D. Jokanovic, and N. Shiratori, "An algorithm for the multidimensional multiple-choice knapsack roblem," in *IEICE Trans. Fundamentals E80-A(3)*, p. 582 589, 1997.

[21] A. Jadbabaie, J. Primbs, and J. Hauser, "Unconstrained receding horizon control with no terminal cost," in *Proceedings of the American Control Conference*, (Arlington, VA), June 2001.

[22] A. B. Roger and C. R. McInnes, "Safety Constrained Free-Flyer Path Planning at the International Space Station," *Journal of Guidance, Control and Dynamics*, vol. 23, pp. 971–979, Dec 2000.

[23] J.-H. Chuang, "Potential-Based Modeling of Three-Dimensional Workspace for Obstacle Avoidance," in *IEEE Transactions on Robotics and Automation*, vol. 14, 1998.

[24] Z.-H. Mao and E. Feron, "Stability of Intersecting Aircraft Flows under Decentralized Conflict Avoidance Rules," in *AIAA Guidance, Navigation and Control Conference*, (Reston, VA), pp. 1042–1052, 2000.

[25] A. Bicchi and L. Pallottino, "On Optimal Cooperative Conflict Resolution for Air Traffic Management Systems," in *IEEE Trans. on Intelligent Transportation Systems*, vol. 1, pp. 221–231, 2000.

[26] R. Ghosh and C. Tomlin, "Maneuver Design for Multiple Aircraft Conflict Resolution," in *Proceedings of the American Control Conference*, (Chicago, IL), pp. 672–676, 2000.

[27] R. G. Cleggs, "Belmann-Ford and Dijkstra's Algorithm," tech. rep.

[28] P. Toth and D. V. (Editors), *The Vehicle Routing Problem Discrete Math.* the Society for Industrial & Applied Mathematics, Dec. 2001.

[29] K. P. O'Rourke, T. G. Bailey, R. Hill, and W. B. Carlton, "Dynamic Routing of Unmanned Aerial Vehicles Using Reactive Tabu Search," *Military Operations Research Journal*, vol. 6, 2000.

[30] M. Gendreau, A. Hertz, and G. Laporte, "A Tabu Search Heuristic for the Vehicle Routing Problem," *Management Science*, vol. 40, pp. 1276–1289, 1994.

[31] E. D. Taillard, P. Badeau, M. Gendreau, F. Guertin, and J. Y. Potvin, "A Tabu search heuristic for the vehicle routing problem with soft time windows," *Transportation science*, vol. 31, pp. 170–186, 1997.

[32] K. C. Tan, L. H. Lee, Q. L. Zhu, and K. Ou, "Heuristic methods for vehicle routing problem with time windows," *Artificial Intelligence in Engineering*, vol. 15, pp. 281–295, 2001.

[33] N. Pohlman, "Estimation and Control of a Multi-Vehicle Testbed Using GPS Doppler Sensing," Master's thesis, Massachusetts Institute of Technology, 2002.

[34] N. P. J. How and C. W. Park, "GPS Estimation Algorithms for Precise Velocity, Slip and Race-track Position Measurements," in *SAE Motorsports Engineering Conference & Exhibition*, 2002.

[35] J. R. Ellis, *Vehicle Handling Dynamics.* London: Mechanical Engineering Publications, 1994.

[36] C. Tin, "Feedback controller design of the truck testbed." MIT internal report, 2003.

[37] B. Vaglienti, *Lateral track control law for Piccolo.* Cloud Cap Technology, 2003.

[38] B. Williams, P. Kim, M. Hofbaur, J. How, J. Kennell, J. Loy, R. Ragno, J. Stedl, and A. Walcott, "Model-based Reactive Programming of Cooperative Vehicles for Mars Exploration," in *International Symposium on Artificial Intelligence and Robotics & Atomation in Space*, (St. Hubert, Canada), 2001.

[39] F. Glover and M. Laguna, *Tabu Search.* Kluwer Acad. Publ., 1997.